Beyond the trenches: a landscape-oriented chronostratigraphic approach to MIS 5 Middle Paleolithic open-air sites on the European Plain : case studies from Lichtenberg and Khotylevo I

Hein, M.

APPENDIX I: SUPPLEMENTARY INFORMATION FOR CHAPTER II

Luminescence chronology of the key-Middle Paleolithic site Khotylevo I (Western Russia) - Implications for the timing of occupation, site formation and landscape evolution

Supplementary Information

Tab. 1: Contributions of alpha, beta and gamma dose rates to the total dose rate of each sample. In-situ gamma spectrometry was used for samples L-EVA 1712, L-EVA 1714 and L-EVA 1716 (shown in bold).

Lab.-ID (L-EVA)	Alpha DR (mGy/a)	Beta DR (mGy/a)	Gamma DR (mGy/a)	Cosmic DR (mGy/a)	Total DR (mGy/a)
1702	0.86 ± 0.15	1.55 ± 0.13	0.88 ± 0.09	0.20 ± 0.02	3.49 ± 0.22
1703	0.10 ± 0.05	1.74 ± 0.18	0.79 ± 0.05	0.19 ± 0.02	2.81 ± 0.15
1704	0.10 ± 0.06	1.90 ± 0.20	0.84 ± 0.06	0.18 ± 0.02	3.02 ± 0.16
1705	0.09 ± 0.06	1.57 ± 0.17	0.71 ± 0.06	0.17 ± 0.02	2.54 ± 0.14
1706	0.07 ± 0.05	1.52 ± 0.16	0.60 ± 0.05	0.16 ± 0.02	2.35 ± 0.14
1707	0.09 ± 0.05	1.81 ± 0.19	0.78 ± 0.06	0.16 ± 0.02	2.84 ± 0.15
1708	0.11 ± 0.05	2.07 ± 0.20	0.94 ± 0.06	0.15 ± 0.01	3.27 ± 0.16
1709	0.10 ± 0.05	1.96 ± 0.18	0.86 ± 0.06	0.14 ± 0.01	3.06 ± 0.15
1710	0.08 ± 0.05	1.73 ± 0.19	0.72 ± 0.06	0.14 ± 0.01	2.67 ± 0.16
1711	0.08 ± 0.06	1.68 ± 0.19	0.67 ± 0.06	0.14 ± 0.01	2.56 ± 0.15
1712	0.05 ± 0.05	1.29 ± 0.16	**0.58 ± 0.06**	0.13 ± 0.01	2.05 ± 0.14
1713	0.06 ± 0.06	1.48 ± 0.17	0.52 ± 0.05	0.13 ± 0.01	2.18 ± 0.14
1714	0.06 ± 0.05	1.42 ± 0.17	**0.60 ± 0.06**	0.13 ± 0.01	2.20 ± 0.15
1715	0.06 ± 0.06	1.46 ± 0.18	0.51 ± 0.06	0.13 ± 0.01	2.15 ± 0.15
1716	0.07 ± 0.05	1.54 ± 0.17	**0.64 ± 0.06**	0.12 ± 0.01	2.37 ± 0.14
1717	0.04 ± 0.06	1.24 ± 0.18	0.39 ± 0.06	0.12 ± 0.01	1.80 ± 0.15
1718	0.06 ± 0.05	1.43 ± 0.17	0.52 ± 0.05	0.12 ± 0.01	2.13 ± 0.14
1719	0.06 ± 0.05	1.37 ± 0.17	0.52 ± 0.06	0.12 ± 0.01	2.08 ± 0.15

Tab. 2: Residual doses (RD) of the three different protocols measured after 3 hours of solar bleaching.

	***pIRIR$_{225}$* RD (Gy)**	***pIRIRI$_{290}$* RD (Gy)**	***pIRIR$_{290}$* (hb) RD (Gy)**	
Sample (L-EVA)	**1706**	**1706**	**1706**	**1715**
	8.20	26.65	21.75	21.61
	8.12	26.36	22.11	33.67
	9.77	30.40	27.20	30.42
				33.64
Sample (L-EVA)	**1707**	**1707**	**1707**	**1717**
	3.31	16.59	14.81	17.76
	3.02	17.70	29.83	21.58
	6.27		23.41	17.94
				19.58
Sample (L-EVA)	**1710**	**1710**	**1710**	**1718**
	2.11	1.81	14.00	19.33
	3.50	5.62	32.93	19.95
	10.32		34.61	21.76
				27.52

.

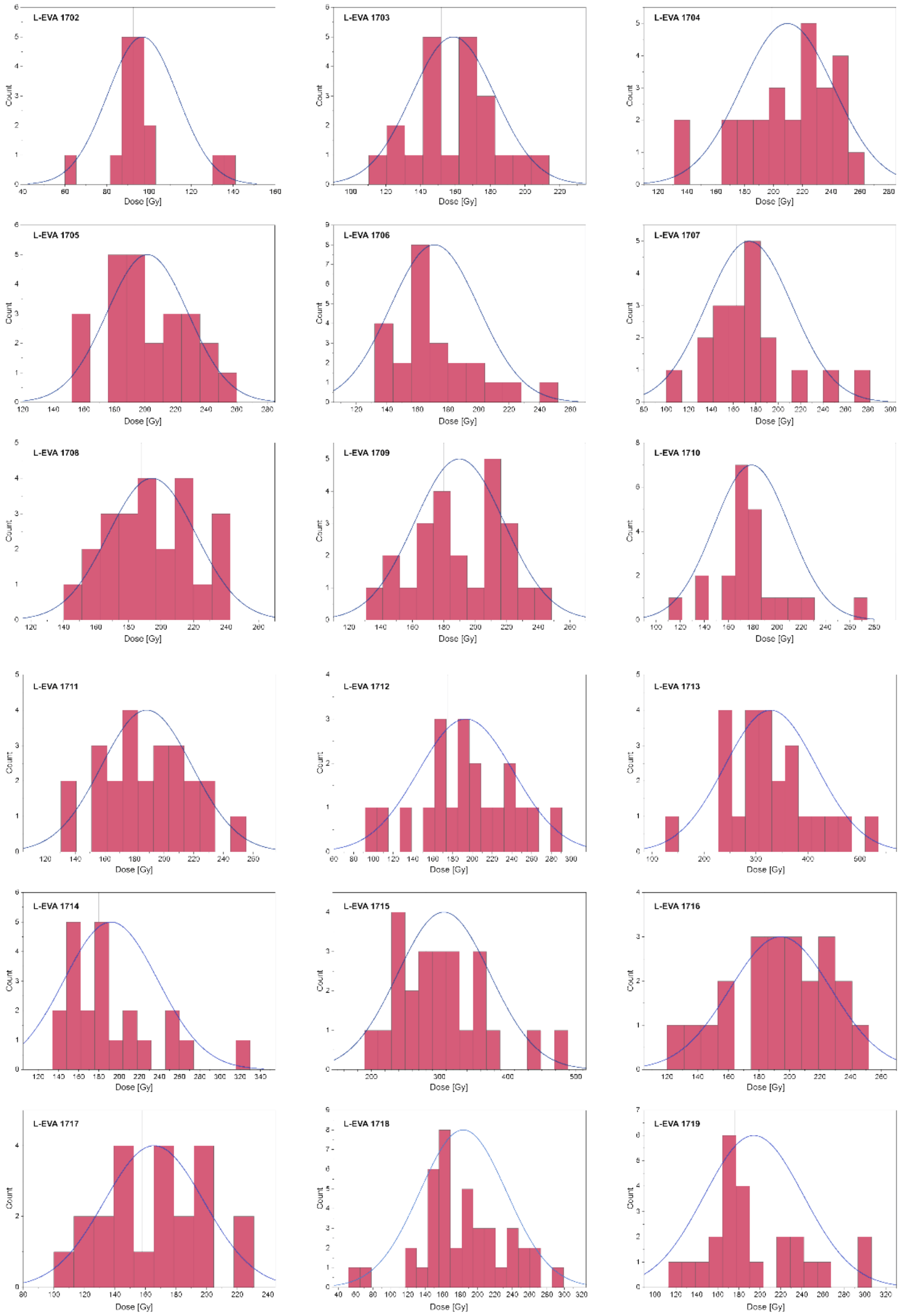

Fig. 1: De-distributions of all measured samples. The vertical reference line represents the weighted-mean estimate, and the blue curve displays an ideal normal distribution.

APPENDIX II: SUPPLEMENTARY INFORMATION FOR CHAPTER III

Eemian landscape response to climatic shifts and evidence for northerly Neanderthal occupation at a palaeolake margin in Northern Germany

Michael Hein, Brigitte Urban, David Colin Tanner, Anton Hermann Buness, Mario Tucci, Philipp Hoelzmann, Sabine Dietel, Marie Kaniecki, Jonathan Schultz, Thomas Kasper, Hans von Suchodoletz, Antje Schwalb, Marcel Weiss, Tobias Lauer

Published in ESPL (DOI: 10.1002/esp.5219)

Supplementary information

1. Geomorphological situation revealed by DEM analysis

Prior to fieldwork, we carried out a simple GIS-based exploration of the study area so that we could integrate stratigraphic findings into a landscape context and assess the validity of the investigated archive. We used QGIS (version 3.15) and digital elevation models (DEM) with 1 m spatial resolution (State Offices for Geoinformation and Land Survey in Lower Saxony and Saxony-Anhalt). Furthermore, digitized geological maps (1:25.000) were part of our GIS database (Merkt, 1975; Schwalb, 1987), acquired from the State Office for Mining, Energy and Geology, Lower Saxony and the State Office for Geology and Mining, Saxony-Anhalt. We used the data to identify landforms such as depressions, channels and periglacial features, and to distinguish those from the Saalian glacial landforms by means of stratigraphic relationship.The southern slope of the morainic remnant of the Öring is dissected by at least two larger valleys with lengths >2000 m, and corresponding alluvial fans formed at their mouths (referred to here as 1st order alluvial fans, Suppl. Fig. 3; Fig. 3B/C, main article). According to Fränzle (1988; cf. Garleff and Leontaris, 1971; Schokker et al., 2004), these erosional and depositional features developed during the late Saalian – early Eemian transition. Because the 1st order dry valleys dissect the Warthe glacial deposits from the latest Saalian, the Saalian-Eemian transition can safely be assumed for their formation, as well (Suppl. Fig. 1; Fig. 3B, main article). Our study site is located near the easternmost of these Öring alluvial fans, in proximity to a channel passage between Öring and Lemgow (Fig. 3, Suppl. Figs. 2 and 3). This channel passage is assumed to have its origins in a precursive Elsterian tunnel valley (Voss, 1981), and to have facilitated hydrological exchange ever since with the adjacent ice-marginal valley of the River Elbe. After the formation of the eastern fan, a subsequent incision created a roughly

W-E striking depression within this fan (Suppl. Fig. 3), which is physically linked with this channel passage between Öring and Lemgow. In Suppl. Fig. 2 we geometrically explore the whole palaeovalley system, including the 1st order dry valley in the SE Öring, the incised depression within the 1st order alluvial fan and the channel passage (between Öring and Lemgow) by means of longitudinal and cross sections. It shows the high likeliness of a discharge from the SE Öring on the shortest course towards the adjacent ice-marginal valley (cf. Suppl. Fig. 3). Later on, a smaller dry valley from the north aggraded a smaller fan within this preceding incised depression of the eastern 1st order alluvial fan (Suppl. Fig. 3), which had turned into a part of a fingerlake in the meantime. Stratigraphic superposition requires that these smaller features developed after the incision within the 1st order fan. Hence, we refer to the smaller landforms as 2nd order dry valley and alluvial fan. The location of our borehole transect and seismic profile was chosen to cut the 2nd order fan lengthwise and the incised depression within the 1st order fan crosswise (Fig. 3C). South of our study site a WNW – ESE striking and ca. 2 km long distinct ridge rises ~1.5 m above the surroundings, detaching our study site from the centre of the basin. This ridge has likely acted as a hydrographic divide in former times, as it does today (see Fig. 3B). Even well into the 20th century, the basin was periodically submerged with seepage waters during flooding of the Elbe valley, until the expansion of the drainage network in the 1960s artificially lowered the groundwater level (pers. comm. with residents). Thus, it is safe to assume that the basin repeatedly accommodated a water body whenever favourable hydrographic conditions existed. There is little other information about the formation of the basin itself that concerns the geological evolution, and the different stages and chronology of the lake development.

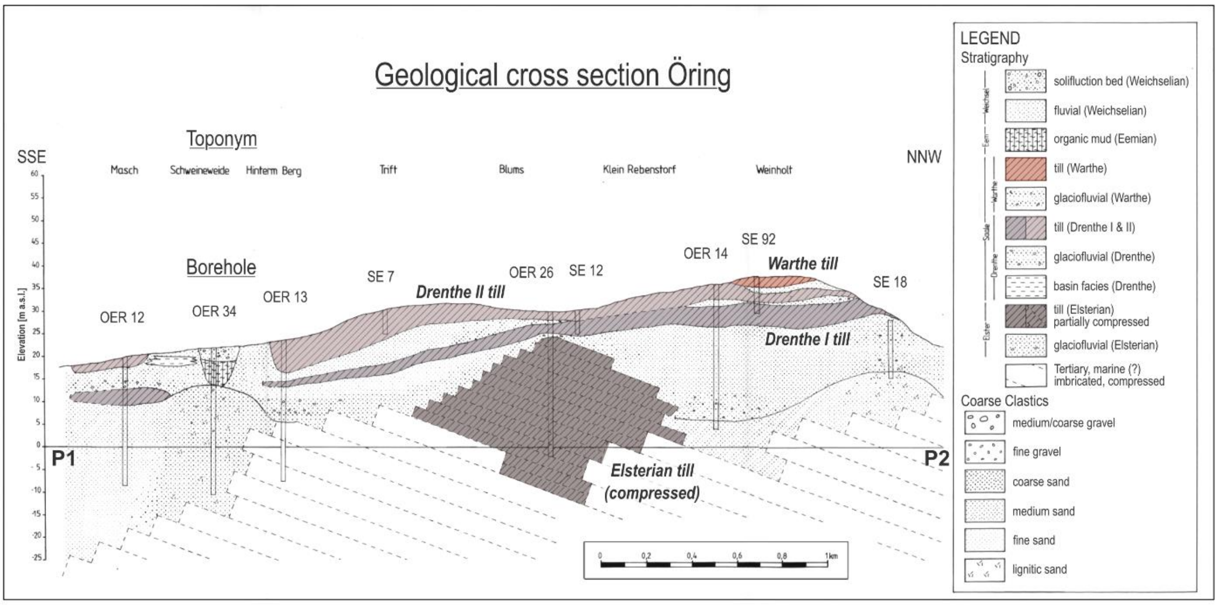

Suppl. Fig. 1: Geological cross-section of the Öring (modified after Schwalb, 1987) showing the stratigraphic relations of the occurring glacial tills. Note the deformed Elsterian till in core OER 26 (about 7 m depth), which we encountered in our core PD.020 as well. P1 and P2 refer to the position of the cross-section that is indicated in main Fig. 3A.

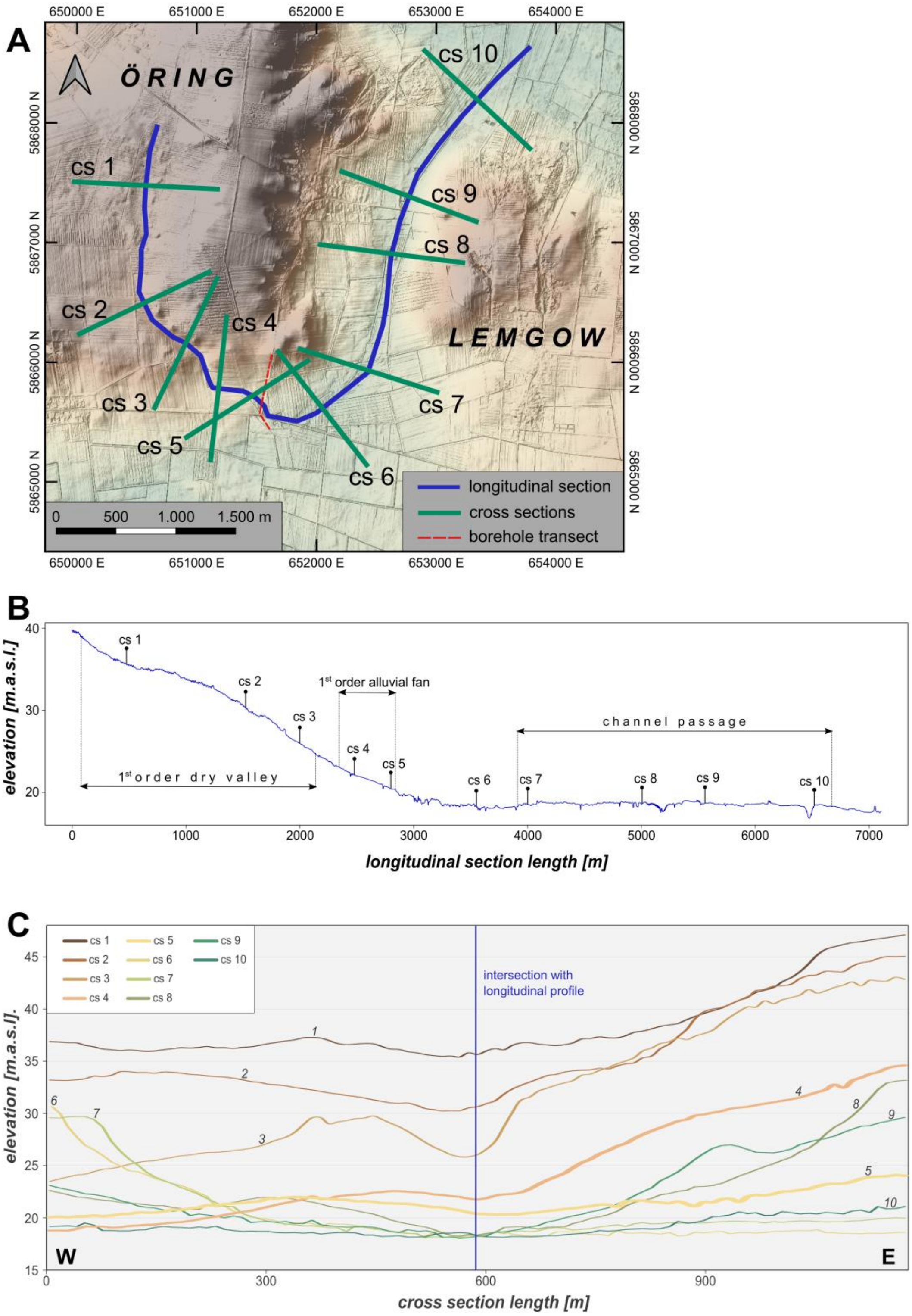

Suppl. Fig. 2: Positions of the longitudinal and cross-sections for morphometrical assessment of the presumed palaeovalley system at the Saalian-Eemian transition (for spatial context see Fig. 3, main article). B Exaggerated slope of the palaeovalley system along thelongitudinal section. Intersection with the cross-sections and the main geomorphological units are indicated. C Morphometry and elevation of the cross-sections.

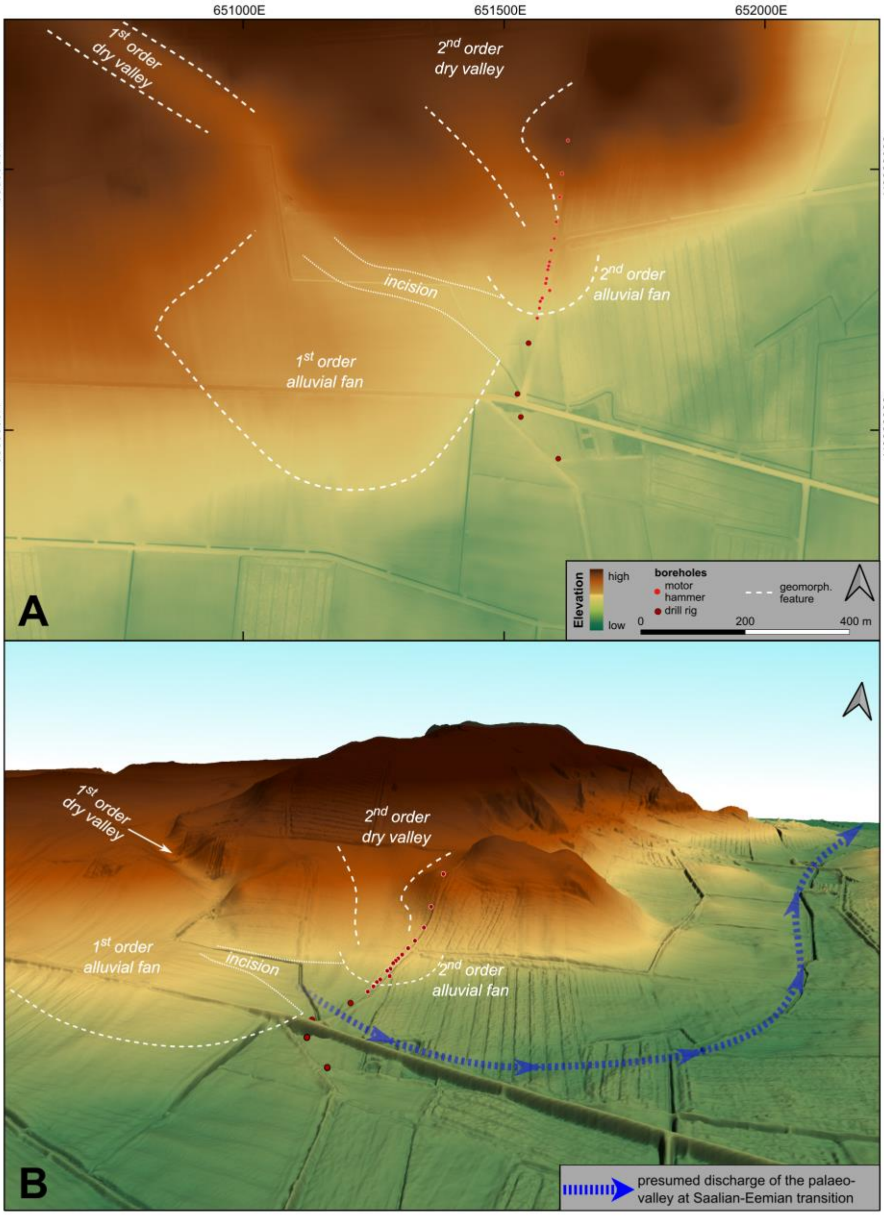

Suppl. Fig. 3: Main geomorphological features around the presented borehole transect in a 2d (A) and 3d-view with a 20x exaggeration (B). For spatial context see Fig. 3, main article. Presumed discharge direction of the palaeovalley at the Saalian-Eemian transition is derived from Suppl. Fig. 2.

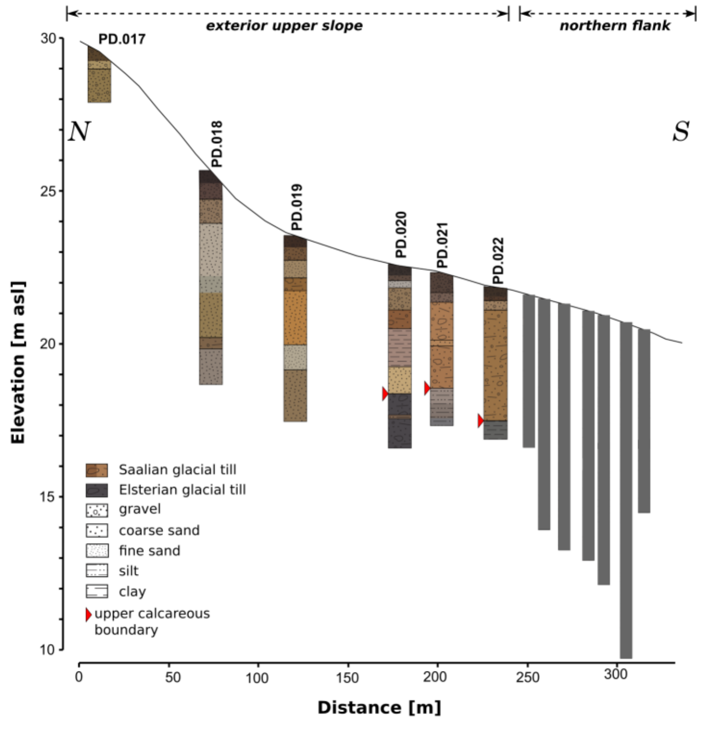

Suppl. Fig. 4: Sedimentary log of the exterior part of the borehole transect. For position, see Figs. 3 and 4 of the main article. Descriptions in section 4.1, main article.

2. Criteria for the assignment of distinct pollen zones

When working on single bulk samples, assemblages characteristic of certain pollen zones (e.g. E II, E VII, WF II) are at times hardly distinguishable from one another. In these cases we took stratigraphic considerations into account and tentatively assigned the (two) most likely pollen zones. Examples are samples 1, 2, 3, 7 and 20. Especially in the early and late Eemian periods, the amount of reworked pollen is partially quite high, obscuring the in-situ proportion and making attribution to a pollen zone difficult (samples 5, 7, 11, 12, 15, 21). When parts of an undisturbed underlying assemblage are found in the redepositional zone, they indicate the maximum stratigraphic age. In the same manner, the overlying in-situ assemblages constrain the minimum stratigraphic age. If no postdating sample was available, we could only narrow down deposition to a transitional period (samples 7, 12). Only in one case, we refrained from assigning a pollen zone, because redeposition could have occurred between PZ E V/VI and WF I (sample 5).Due to a gradually-sinking water table, the pollen-bearing organogenic deposits on the slopes fell dry at some point and formed the surface for an uncertain time. In this way, the dominating part of the pollen spectrum would be from the time of sediment formation, with a later overprint of continuing pollen deposition. As this is not easily detected in bulk samples, we sometimes assigned two equitable, neighboring pollen zones (samples 24 and 25).

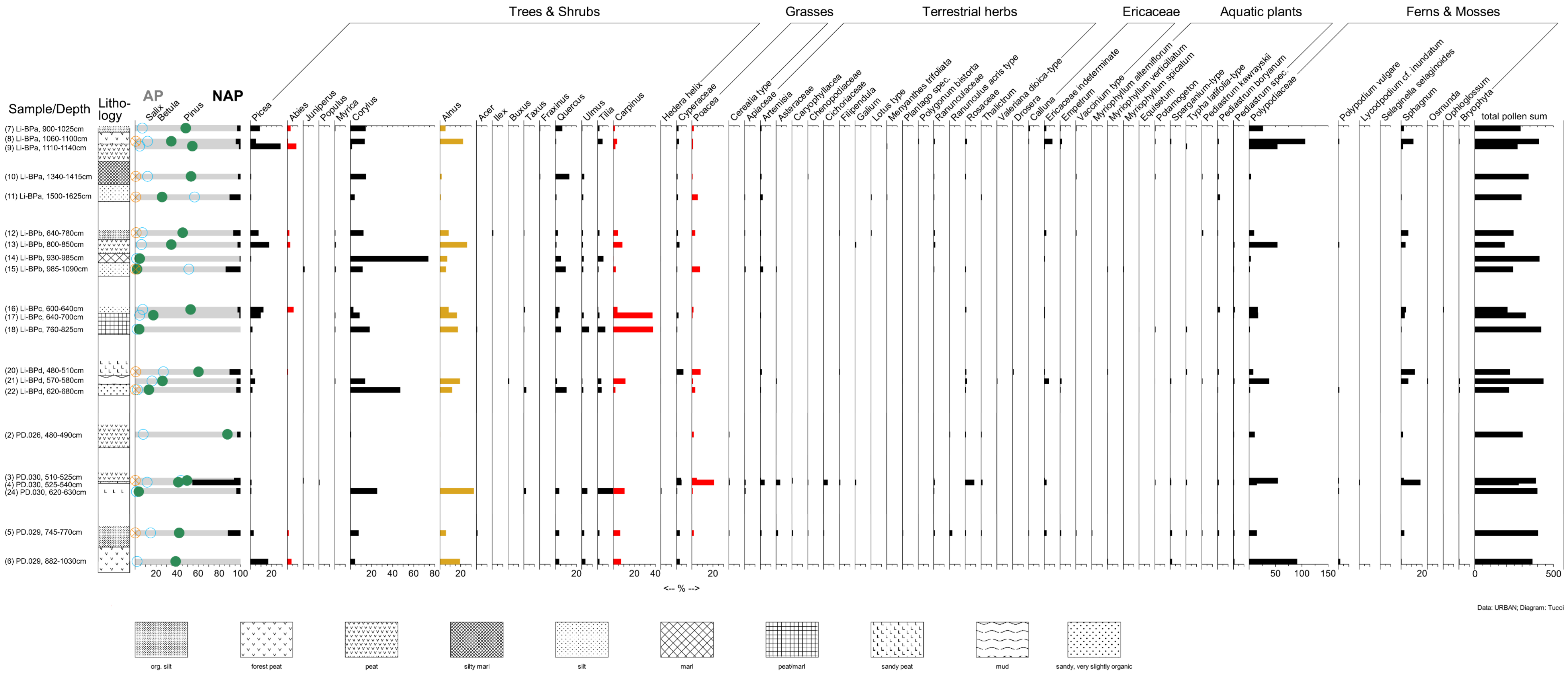

Suppl. Fig. 5: Palynological results plotted either as single sample or as a short pollen diagram.

3. Additional seismic information

A special difficulty of the S-wave seismic measurements is the velocity distribution in the very shallow region. The profile was measured on concrete slabs, and the high velocity of concrete and the compacted material below influenced the stacking velocities. The raw records show strong signals with velocities of ~4000 m s-1 that correspond to P-waves, and ~1000 m s-1 that most probably correspond to flexural waves in the slabs. This energy was attenuated first by amplitude scaling with t^2 up to 150 ms and second by a tight mute after normal move-out (Suppl. Tab. 1). Nevertheless, the high velocities of the consolidated material influence the stacking velocities that decrease strongly in the upper tens of milliseconds. This becomes particularly more obvious in the southern part of the profile, where peat layers also reduce the seismic velocities.To check to velocities derived by seismic processing (and therefore the processing itself), we conducted a S-wave VSP (vertical seismic profile) in the 22 m-deep Li-BPa borehole, as well as a gamma ray borehole survey (for position see Figs. 3and 4, main article; Suppl. Fig 6). The distance to the seismic line is 13 m. We used the same source as used for the survey and a three-component borehole geophone that was lowered successively by 1 m to record two shots of opposite polarity. The results (Suppl. Fig. 6) show S-wave velocities between very low values of 70 m s-1 up to 330 m s-1, where an upper zone of low velocities reaches down to 7 m and another one exists between 10 and 16 m. They positively correlate well with the gamma-ray log; i.e. low velocity values correspond to low gamma-ray values (Suppl. Fig 6). These values represent peat and fines (Fig. 5B, main article). The velocities in the VSP survey reaches lower values than those derived from stacking velocities; this can be attributed to the much lower resolution of the stacking velocities.Seismic S-wave velocity shows lateral variations (compare Fig. 5B, main article and Suppl. Fig. 7) from higher values in the Saalian and Tertiary sediments with over 300 m s-1 TWT to very low values (170-230 m s-1 TWT) in the youngest sediments, especially the peat layers. These extremely low velocities testify to the unconsolidated nature of these sediments and support our stratigraphic interpretations.

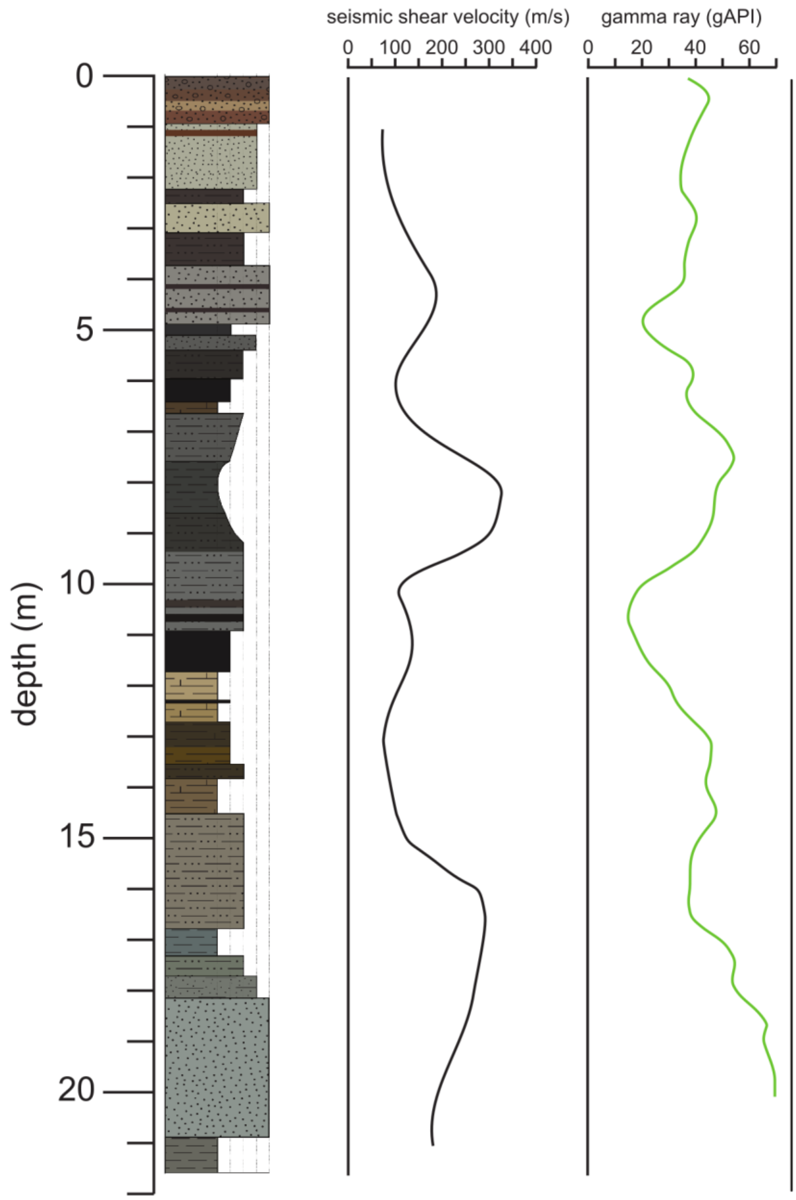

Suppl. Fig. 6: Borehole geophysics from borehole Li-BPa. First column, borehole with lithological column. Colours see Figure 4, main article. Second column, S-wave velocity derived from a Vertical Seismic Profiling (VSP). Third column, gamma ray log.

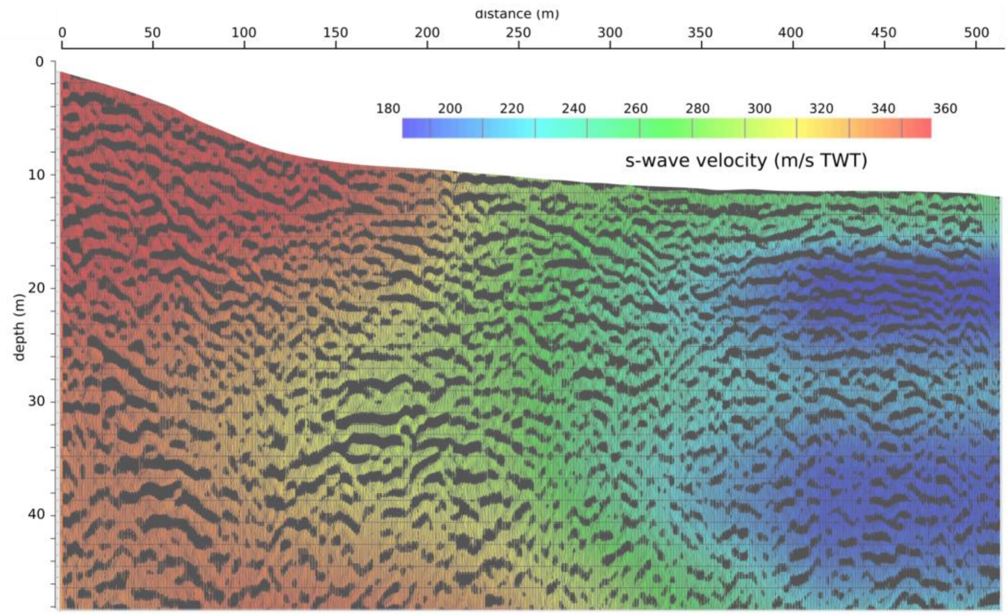

Suppl. Fig. 7: S-wave velocity of the seismic profile.

1	Correlation using recorded sweep
2	Vertical stack
3	Elevation static
4	Bad trace editing
5	True amplitude recovery (T**2)
6	AGC (150 ms)
7	Spectral whitening (20-160 Hz)
8	Time variant bandpass filter (60-160 Hz, 40-160 Hz)
9	Interactive velocity analysis
10	Normal moveout correction (100 % stretch mute)
11	Top mute of refracted and oscillating events
12	CDP stack (α trimmed mean, 20% excluded)
13	Tau-P filter (+- 0.5 ms/trace)
14	Time-depth conversion (smoothed velocities)
15	Correction to final datum

Suppl. Tab. 1: Seismic processing stages.

4. Luminescence data evaluation

We utilized coarse-grained (125-180 µm) potassium-feldspar on account of its higher saturation values compared with quartz (Lauer et al., 2017) and the pIRIR290 protocol (Suppl. Tab. 2) (Thiel et al., 2011), as it is characterized by only negligible anomalous fading (Buylaert et al., 2012). First performance tests included dose recovery (residual-subtracted measured/given dose of 0.95) and anomalous fading (two samples below 1.6%/decade) on the samples L-EVA 1859 and 1862. These were taken from a neighbouring core with a very comparable sedimentology and expected time horizon. The ages of L-EVA 1859 and 1862 will be reported in a follow-up publication. For De-measurements, we mounted twenty-four small-sized aliquots (0.5 mm) per sample onto stainless steel discs, using with silicone spray. We measured on a Risø TL-DA-20 reader with an internal calibrated 90Sr/90Y beta source (~0.22 Gy s-1) and IR light-emitting diodes (870 nm). The applied pIRIR290 protocol is summarized in Suppl. Tab. 2. Aliquots with a recycling ratio >10 % and a recuperation >5 % were excluded from further calculations. The equivalent doses for age calculations were established using kernel density estimates (KDE) by choosing the age model closest to the most meaningful KDE peak in terms of sedimentology and stratigraphy (Suppl. Fig. 7) (Galbraith and Roberts, 2012). Dose rates were determined with high-resolution germanium gamma spectrometry at the VTKA laboratory Dresden (Suppl. Tab. 3). Contributions of cosmic radiation and internal beta dose-rate were accounted for by following Prescott and Hutton (1994) and Huntley and Baril (1997), whereas alpha particle efficiency was approximated with an a-value of 0.11 (Kreutzer et al., 2014).In spite of comparable bandwidths selected for both luminescence samples in the KDE plots (31.67 for L-EVA 2026 and 39.71 for L-EVA 2027), their distributions differ substantially. L-EVA 2026 features multiple De-populations, presumable due to short-distance reworking of Saalian glaciofluvial sands with only partial bleaching during the process. Since the overlying stratum in core PD.030 is an undisturbed peat, we do not expect post-depositional mixing by cryo- or bioturbation. We consequently opted for the minimum age model after Galbraith et al. (1999), using the r.luminescence package (Burow, 2020), with the default settings and a σb–value of 0.1, which assumes 10% hypothetical overdispersion in an ideally bleached sample (Galbraith and Roberts, 2012). This model and the obtained De-value (264.4 Gy) best reflect the youngest population within our De-spectrum (Tab. 2, Suppl. Fig. 8). Sample L-EVA 2027 shows a more coherent and single-mode De-distribution, although a small shoulder in the KDE curve around 470 Gy indicates a distinct older population. For age calculations, we chose the weighted mean (De-value of 295.2 Gy), which is nearly coincident with the main mode of the distribution.The ages (108.4 ± 17.0 ka for L-EVA 2026 and 104.6 ± 10.5 ka for L-EVA 2027) imply early Weichselian deposition and are therefore in compliance with the stratigraphy of the samples above the mid-Eemian stratum (cf. section 4.1, main article). They are also in excellent agreement with the end of the Eemian interglacial, as dated by Lüthgens et al. (2011) to 108.9 ± 7.8 ka in NE Germany. As we do not know how much time passed at our site before clastic sedimentation commenced after the Eemian, our ages primarily help constrain the chronology of the peat deposit between the sampling positions of L-Eva 2026 and L-EVA 2027, determined to be of Herning Stadial age (Tab. 1, sample 4, main article) (Menke and Tynni, 1984). The high OD-values (33.3 ± 1.4% for L-EVA 2026 and 26.6 ± 0.8% for L-EVA 2027) could result from post-depositional mixing, incomplete bleaching and small-scale dose-rate differences (Jacobs and Roberts, 2007). We exclude post-depositional mixing because of seemingly intact overlying organogenic sediments in both cases. Incomplete bleaching could be an issue because of short transport distances of the grains on the slope. Dose rate variations are just as likely, keeping in mind that we took the samples from relatively broad (15 cm) segments of the cores.

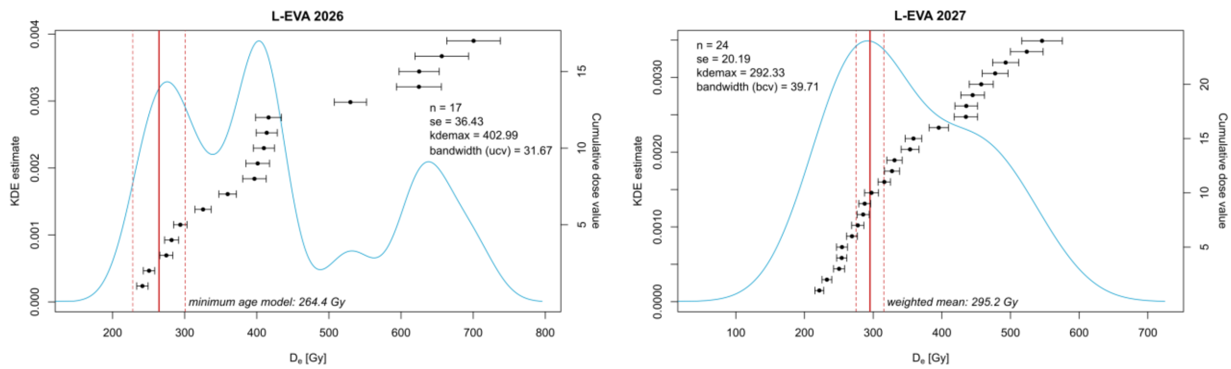

Suppl. Fig. 8:D_e-distribution of the measured luminescence samples, plotted as Kernel Density Estimates (KDE). The KDE modes helped to choose the appropriate age models.

Step	Treatment
1	Dose
2	Preheat (320°C for 60s)
3	IRSL, 100s at 50°C
4	IRSL, 200s at 290°C → L_x
5	Test dose
6	Preheat (320°C for 60s)
7	IRSL, 100s at 50°C
8	IRSL, 200s at 290°C → T_x
9	IRSL, 100s at 325°C → hot bleach
10	Return to step 1

Suppl. Tab. 2: Measurement steps of the pIRIR$_{290}$ protocol.

Lab.-ID L-EVA	Area (Core)	U (ppm)	Th (ppm)	K (%)	Cosmic Dose (Gy/ka)	DR_{total} (Gy/ka)	H_2O (%)
2026	1 (PD.030)	1.6 ± 0.2	4.2 ± 0.3	1.4 ± 0.1	0.12 ± 0.01	2.44 ± 0.20	14.2 ± 10
2027	1 (PD.030)	4.7 ± 0.5	4.1 ± 0.3	1.1 ± 0.1	0.11 ± 0.01	2.82 ± 0.21	14.8 ± 10

Suppl. Tab. 3: Results of high-resolution gamma spectrometry and utilized water contents for luminescence measurements.

5. Interpretation of the geochemical values

Sample number 23 was taken from a terrestrial, non-hydromorphic soil. It shows low Corg contents (0.62%) and a very narrow C/N ratio of 8.0, in the typical range for present Central European forest soils with mull humus (Ad-hoc-Arbeitsgruppe Boden, 2005). These values suggest good soil aeration that promotes decomposition of organic material and lowering of the C/N ratio. This also explains the poor pollen preservation in this soil, rendering the pollen sample indeterminable (Tab. 1, main article). Samples 2, 24 and 25, which stem from semi-terrestrial half-bogs on the south-facing slope of the channel, feature medium Corg values (4.9 to 15.6%) and wider C/N ratios (16.1 to 25.6), indicating that decomposition of organic material was impaired and its accumulation was favoured by moistening. Again, these values are characteristic for half-bogs (‘Anmoor’ in German), according to AG Boden (2005). Finally, the samples from the forest peat at the bottom part of the channel reveal equally wide C/N ratios (21.7 and 24.6), but even higher Corg contents of 19.5 and 29.5%, pointing to a mesotrophic peat accumulation (Meier-Uhlherr et al., 2015). The Corg and C/N values successfully distinguish the humus-enriched layers and horizons along the Eemian zone of the transect and further justify its meaningful subdivision into a northern flank and a bottom part.

6. Eemian soil formation on Saalian glacial substrates

Generally, Eemian soils on Saalian glacial materials are known to form thick, orange-brown Bt-horizons with illuviated sesquioxides and clay, and their decalcification/weathering zone can exceed 4 m thickness in northern Germany Thus, soil formation is assumed to have been more intense than in comparable Holocene soils on Weichselian tills. Additionally, the distinctive red colouring and less hydromorphic features in the soils suggest warmer and drier climate throughout their formation, as compared to the present interglacial (Roeschmann et al., 1982; Stephan, 2014; Stremme et al., 1982).At the position of core PD.021 we dug a prospection pit, exposing a pebbly and partly brunified Weichselian cover sand (Geschiebedecksand [GDS] in German) and the Eemian soil formed in a Saalian till (Suppl. Fig. 9). The upper part of the till has albic properties, being depleted in iron oxides and clay minerals (WRB, 2015). Along cracks and tongues, this albic fossil E horizon has started to consume the Btg horizon below. The Btg horizon is rich in clay and shows incipient stagnic properties. Overall, the decalcification depth of the Saalian till amounts to about 4 m (cf. cores PD.022 to 025; Suppl. Fig. 9; Fig. 4 in the main article). In terms of weathering intensity and depth, the findings confirm the statements on soil formation and stable surfaces in section 5.1 (main article). They also match the general properties known for such soils (see above). However, a possible weak Holocene continuation of pedogenesis cannot be reliably distinguished from that of the Eemian in this test pit (cf. Roeschmann et al., 1982).

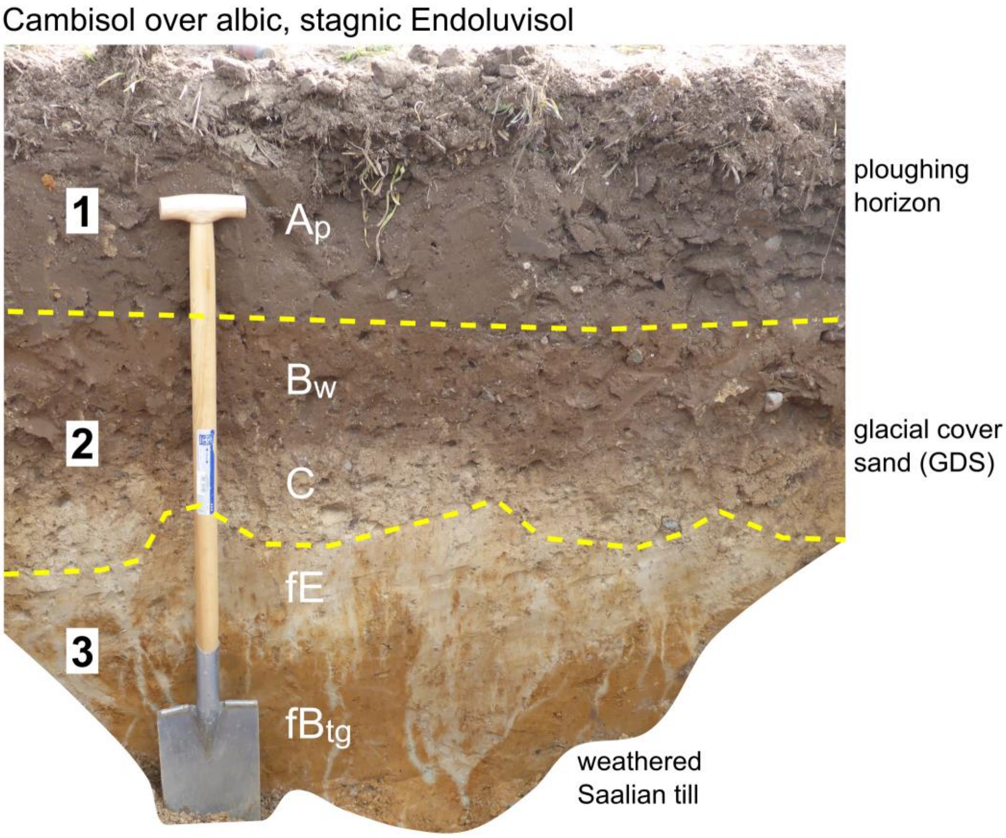

Suppl. Fig. 9: Soil exposure at the position of PD.022 (see Fig. 4, main article), showing weathered Saalian till caused mainly by Eemian pedogenesis. The length of the spade is about 110 cm.

APPENDIX III: SUPPLEMENTARY INFORMATION FOR CHAPTER IV

Supplementary Information S1 – Sections 1 to 4
Archaeology and Artefact Analyses

Neanderthals in changing environments from MIS 5 to early MIS 4 in northern Central Europe – Integrating archaeological, (chrono)stratigraphic and paleoenvironmental evidence at the site of Lichtenberg

Marcel Weiss*[1,2], Michael Hein*[1], Brigitte Urban[3], Mareike C. Stahlschmidt[1], Susann Heinrich[1], Yamandu H. Hilbert[2], Robert C. Power[4,1], Hans v. Suchodoletz[5], Thomas Terberger[6], Utz Böhner[6], Florian Klimscha[7], Stephan Veil[7], Klaus Breest[8], Johannes Schmidt[5], Debra Colarossi[9,1], Mario Tucci[3], Manfred Frechen[10], David Colin Tanner[10] & Tobias Lauer[1]

[1]Max Planck Institute for Evolutionary Anthropology, Leipzig, Germany

[2]Institut für Ur- und Frühgeschichte, Friedrich-Alexander-Universität Erlangen-Nürnberg, Erlangen, Germany

[3]Leuphana University Lüneburg, Institute of Ecology, Lüneburg, Germany

[4]Institute for Pre- and Protohistoric Archaeology and Archaeology of the Roman Provinces, Ludwig Maximilian University Munich, Germany

[5]Institute of Geography, Leipzig University, Leipzig, Germany

[6]State Service for Cultural Heritage Lower Saxony, Hannover, Germany

[7]Lower Saxony State Museum, Department for Research and Collections, Archaeology Division, Hannover, Germany

[8]Volunteer archaeologist, Berlin, Germany

[9]Department of Geography and Earth Sciences, Aberystwyth University, Aberystwyth, Wales, UK

[10]Leibniz Institute for Applied Geophysics, Stilleweg 2, Hannover, Germany

Section 1: Excavation Lichtenberg I and II

Lichtenberg I: 2017

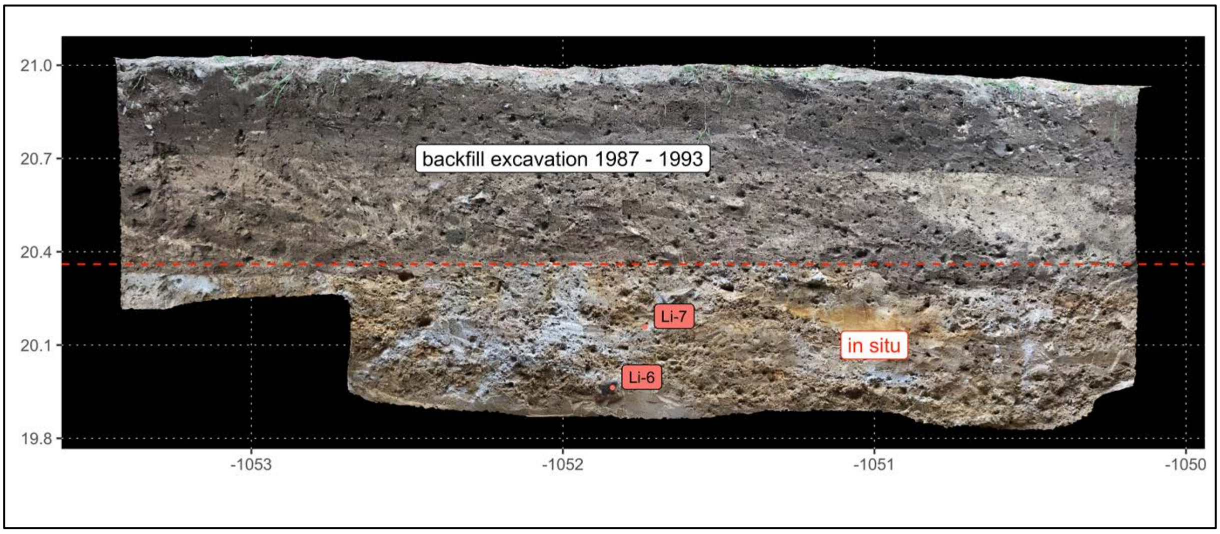

Supplementary Figure S1. Test trench 2017, East profile. Li-7: Keilmesser from Layer 7', Li-6: fragment of a bifacial tool from Layer 7'. Orthophoto created with Agisoft Metashape.

Lichtenberg I: 2019

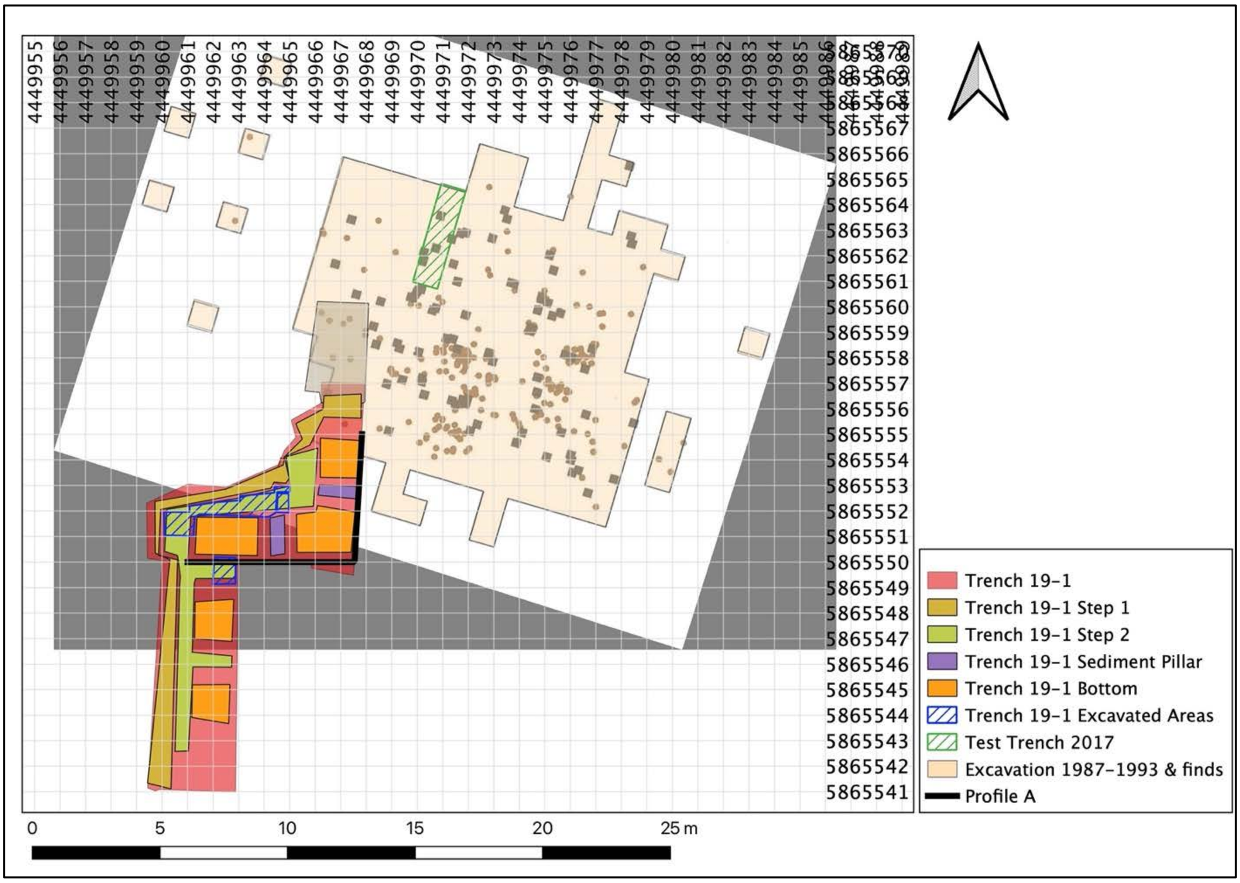

Supplementary Figure S2. Excavation plan Lichtenberg I. Plan created with QGIS 3.12.3.

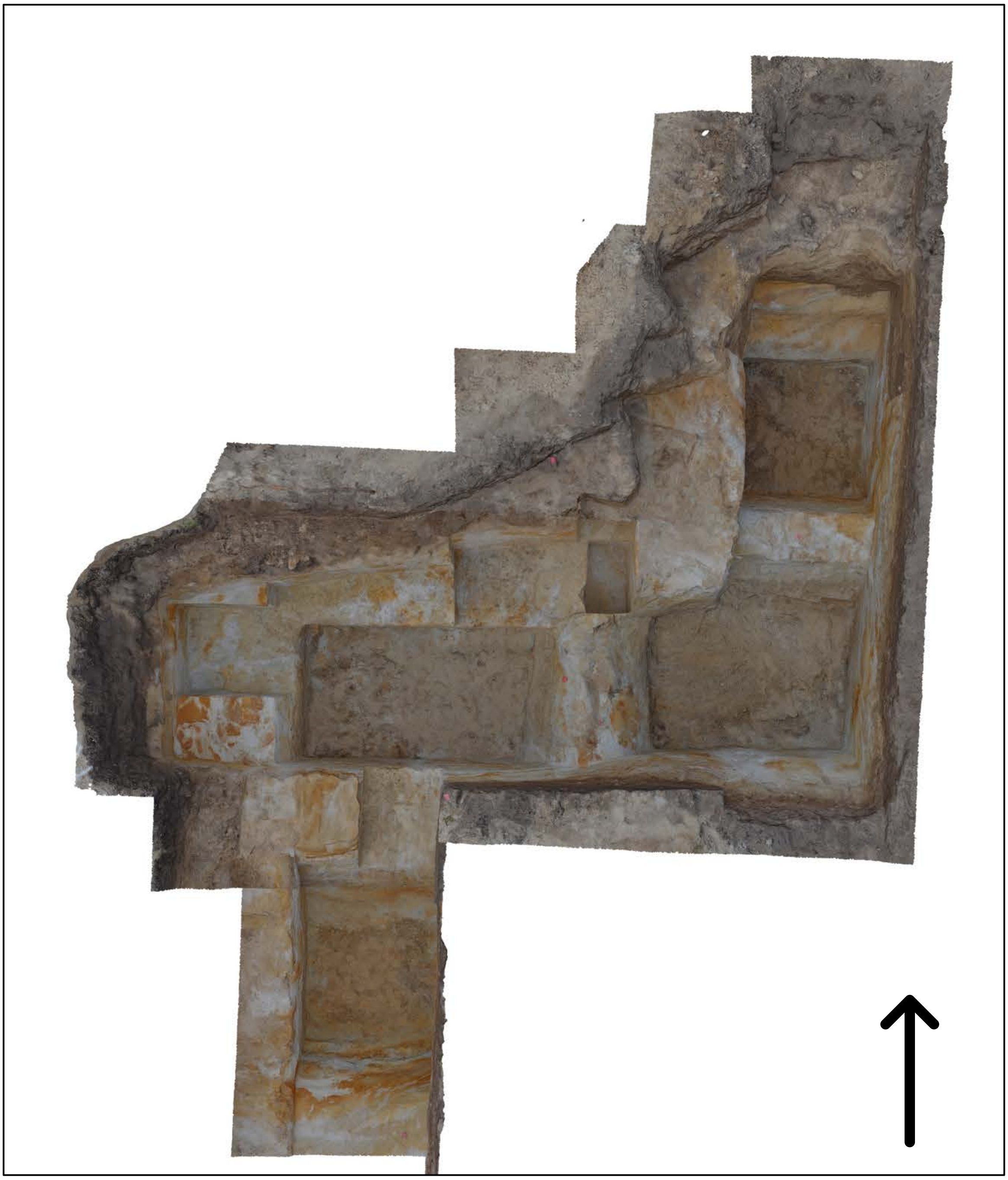

Supplementary Figure S3. Ortho view Trench I. 3D model created with Agisoft Metashape.

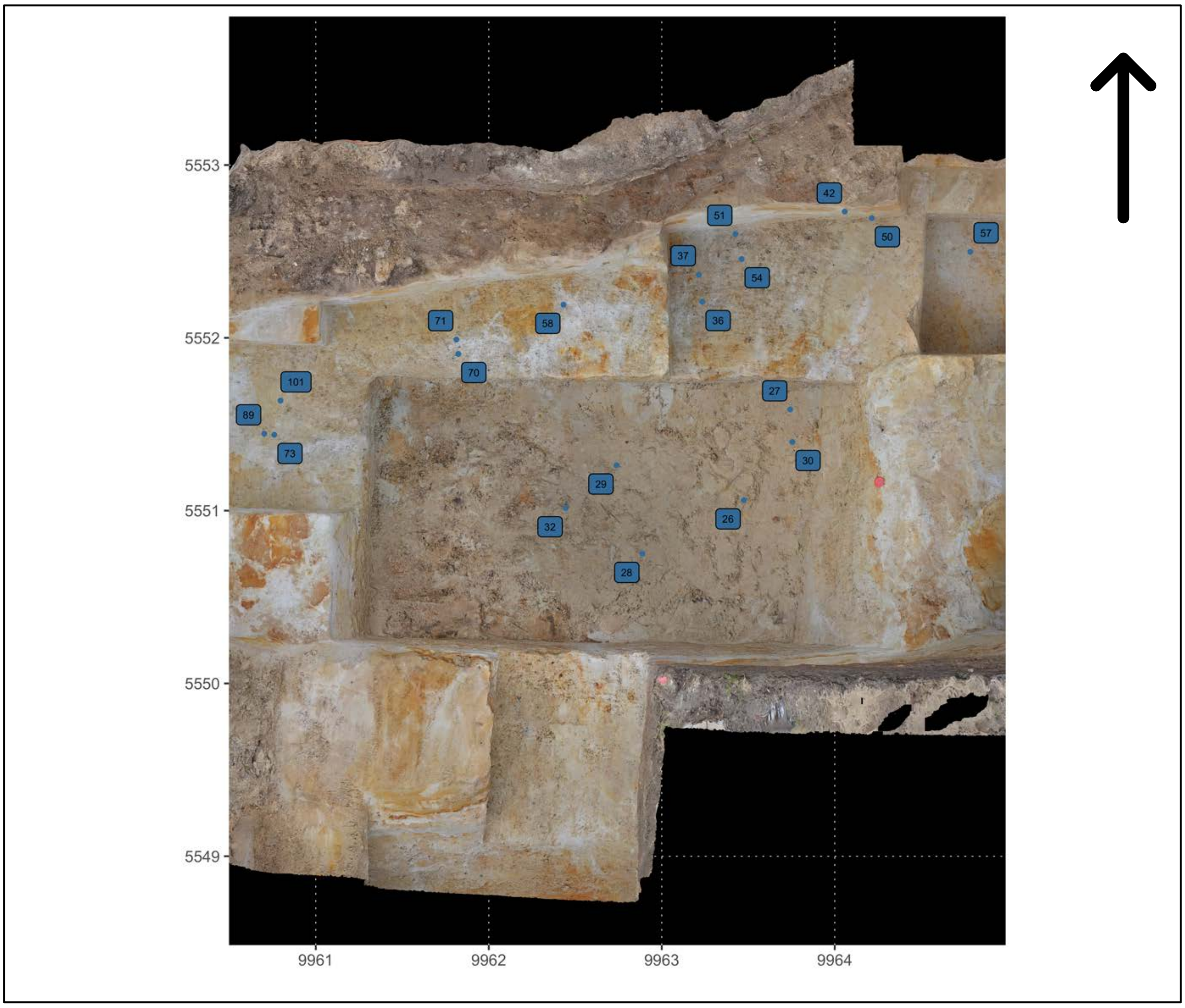

Supplementary Figure S4. Orthographic view of the excavated area and find numbers of artefacts ≥15mm. Orthophoto created with Agisoft Metashape.

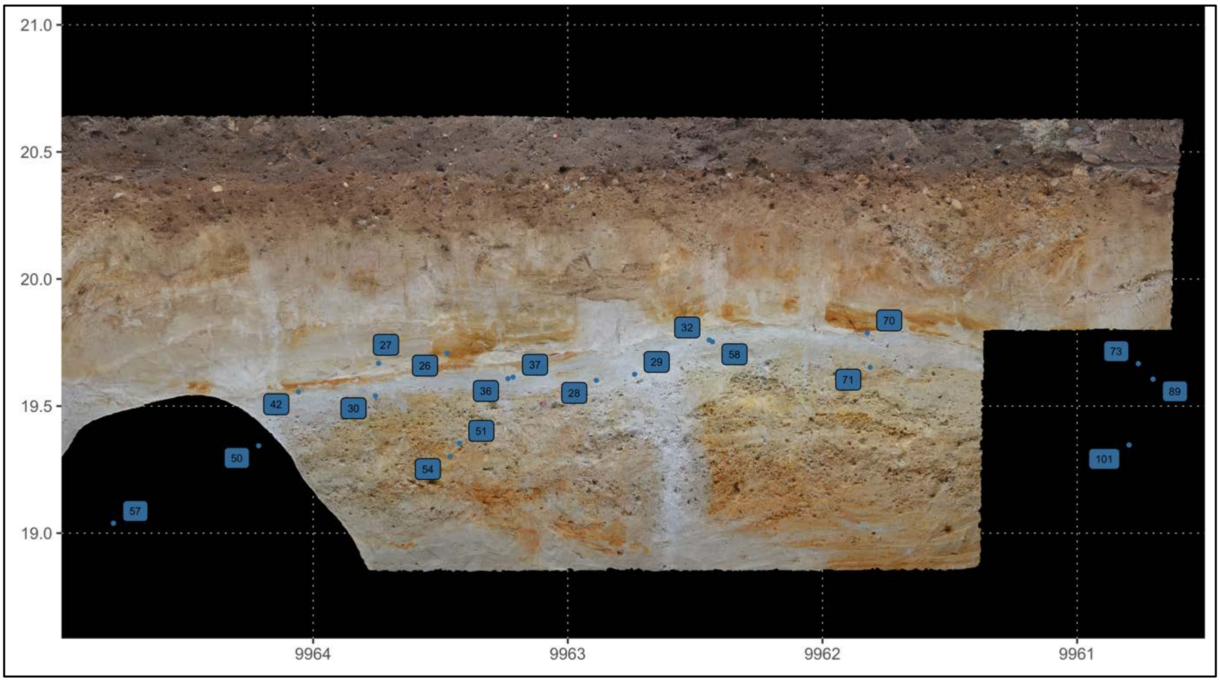

Supplementary Figure S5. Trench 1, South profile with plotted artefacts ≥15mm, Layer 7 and Layer 8. Orthophoto created with Agisoft Metashape.

Supplementary Figure S6. Flake LIA-36 in situ in Layer 7 (formerly: Layer package 2). Photo: M. Weiss.

Supplementary Figure S7. Flake LIA-50 (N) and undiagnostic flint fragment (E) in situ in Layer 8 (formerly: Layer package 2). Photo: M. Weiss.

Lichtenberg II

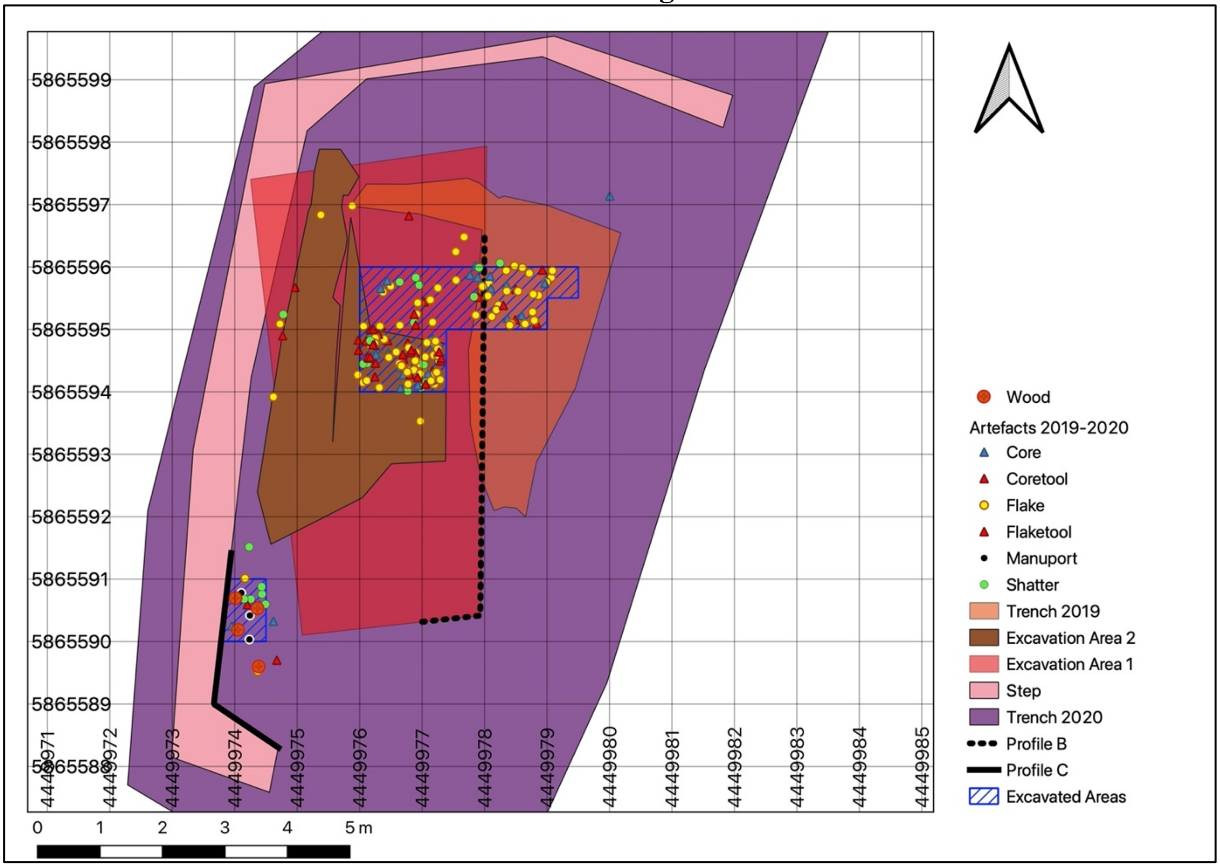

Supplementary Figure S8. Plan of Trench 2 with the excavated squares and find categories. Finds outside the excavated squares were made during the preparation of the excavation and the West-profile. Plotted are alle artefacts ≥15mm. Plan created with QGIS 3.12.3.

Supplementary Figure S9. Trench 2 at the start of the fieldwork in March 2020 with ground water protection. Photo: M. Weiss.


Supplementary Figure S10. Endscraper LIA-285 in situ in Layer 11a. Photo: M. Weiss.

Supplementary Figure S11. Core LIA-335 in situ in Layer 11a. Photo: M. Weiss.

Supplementary Figure S12. Tool LIA-478 in situ in Layer 11a, with a charcoal concentration in the East. Photo: M. Weiss.

Lichtenberg III

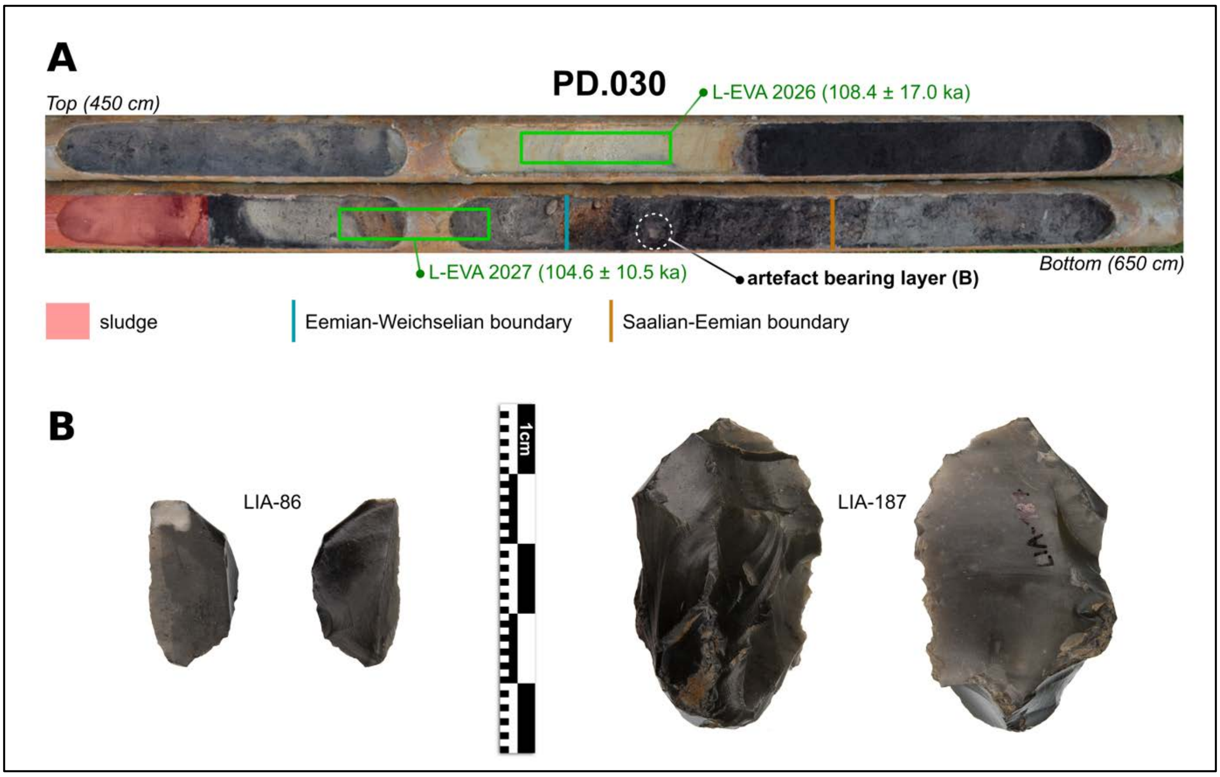

Supplementary Figure S13. A: Core PD.030 with the position of the Eemian artefacts. B: Flakes LIA-86 and LIA-187 from the Eemian Layer. Photos: M. Weiss.

Section 2: Analysis of the find horizon Lichtenberg II

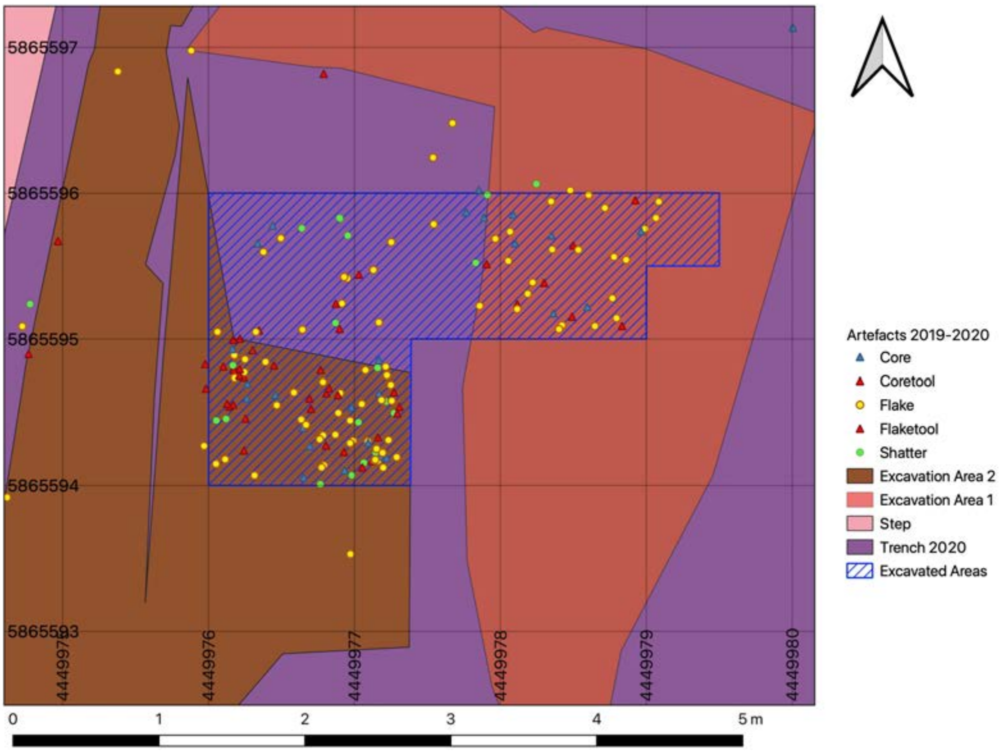

Supplementary Figure S14. Plan of the excavation and position of the excavated squares. Finds outside the excavated squares were made during the preparation of the excavation and the West-profile. Plotted are alle artefacts ≥15mm. In the following analysis, squares are named based on the last 4 digits of the coordinates. Plan created with QGIS 3.12.3

Preface

In the following, we present our analysis of the find horizon (humic sand) from the squares excavated in 2020. The squares are named based on the last 4 digits of the coordinates. The goal of the analysis is to evaluate whether there exists a single, or more than one find horizon within the humic sand. Small lithics <1.5 cm are prone to dislocation by post depositional processes (annimal trampling, cryoturbation, sediment movements). Therefore, the small lithics between 4 mm and 1.49 cm from the screen where counted from each excavated bucket from each quarter square. This resulted in several plots presented in the first section.

Additionally, the position of the lithics >1.49 cm was added to the indivdual plots. This is to see if accumulations of small and large finds are distriubted similarily. A further analysis of the depths follows in Section 2.2.

Further, the thickness of the datapoints in the diagrams displays the gravel content of each bucket. In Section 2.3, we analyze the relationship between small lithics and gravel content further. This is to evaluate whether gravels and small lithics are affected equally by post desposizional processes. In the reverse that means, if the depths of the small lithic counts show no clear find horizon but they correlate with gravel content, post depositional disturbances of the find horizon are probable.

An interesting feature of the Li-II assemblage is that lithics are relatively small (see further Supplementary Section 3.4). Cores from small nodules already hint that this may be due to small raw material available at the site. Therefore, we checked raw material size sampled from the excavation area in relation to artefact size in Section 2.4.

This section was written in RMarkdown.

2.1. The lithics <1.5 cm of the individual quarter squares

2.1.1 square 9978/5595

2.1.1.1 9978/5595 Southwest-Quarter Square

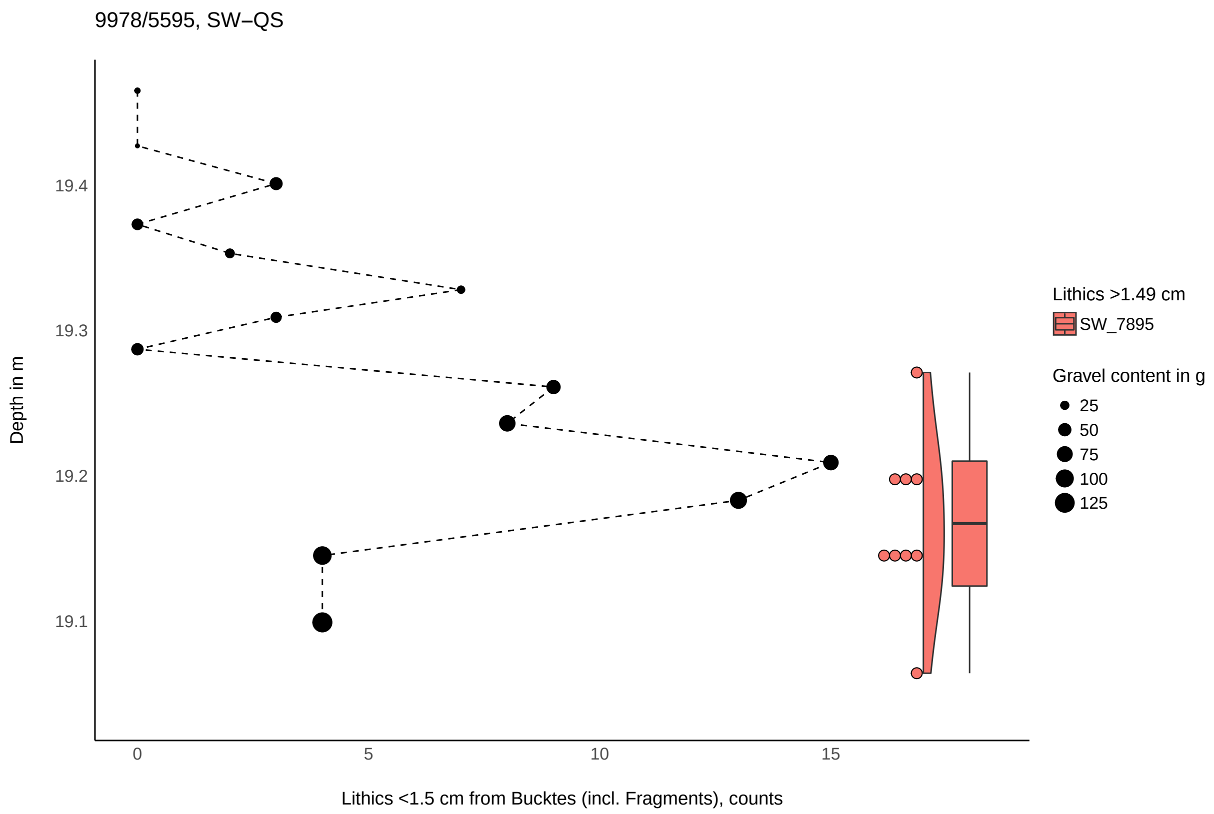

Supplementary Figure S15.

2.1.1.2 9978/5595 North-West Quarter Square

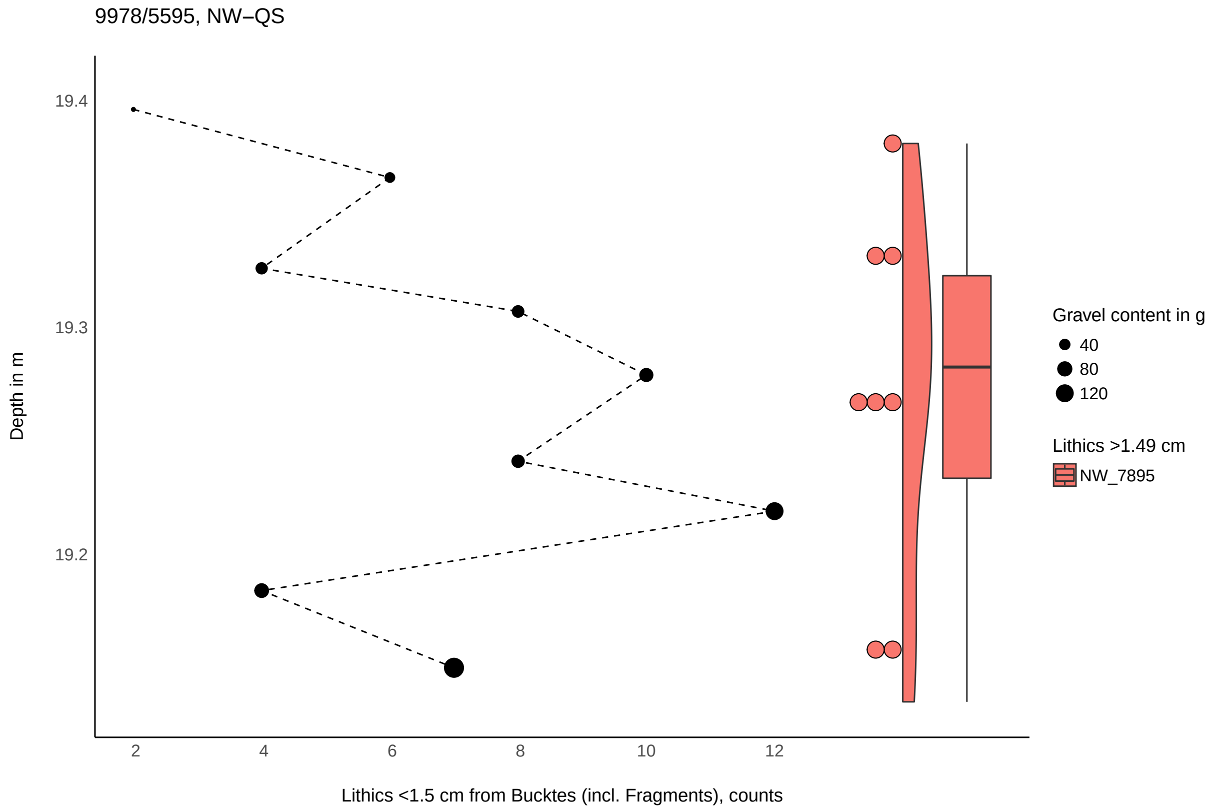

Supplementary Figure S16.

2.1.1.3 9978/5595 Southeast-Quarter Square

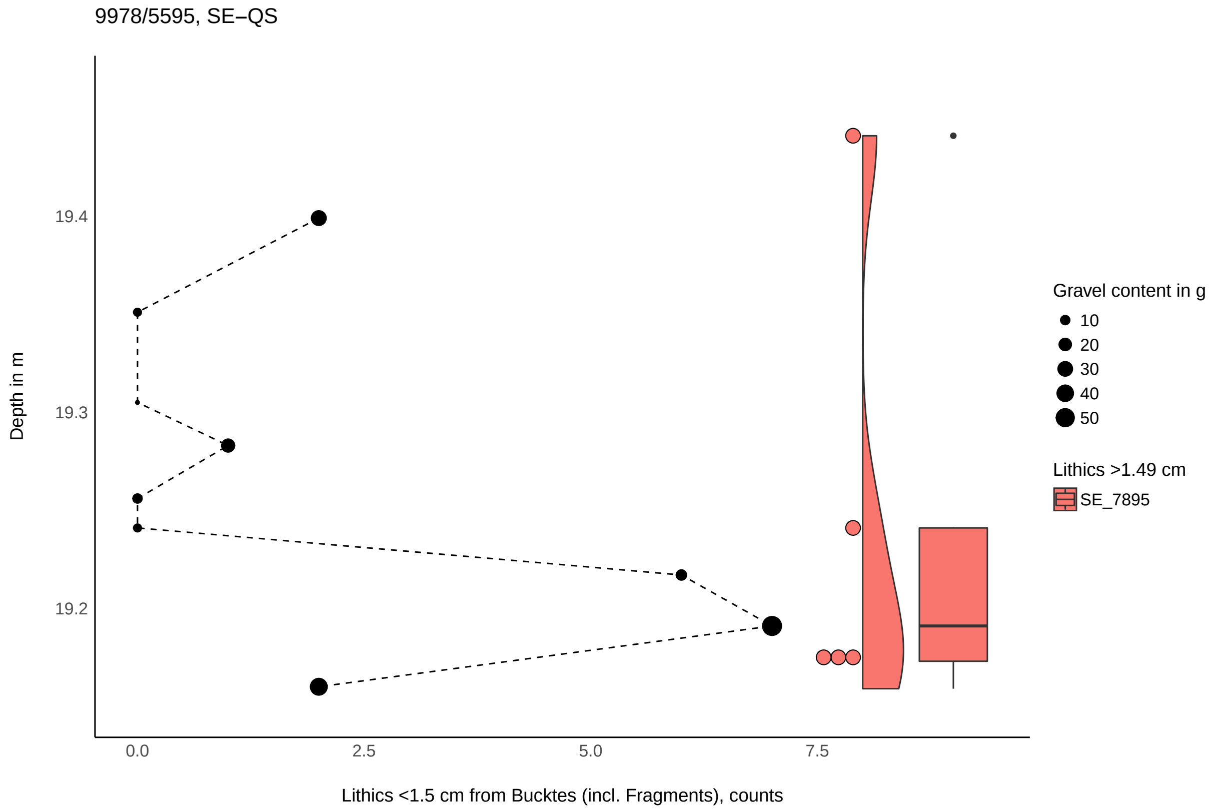

Supplementary Figure S17.

2.1.1.4 9978/5595 North-East Quarter Square

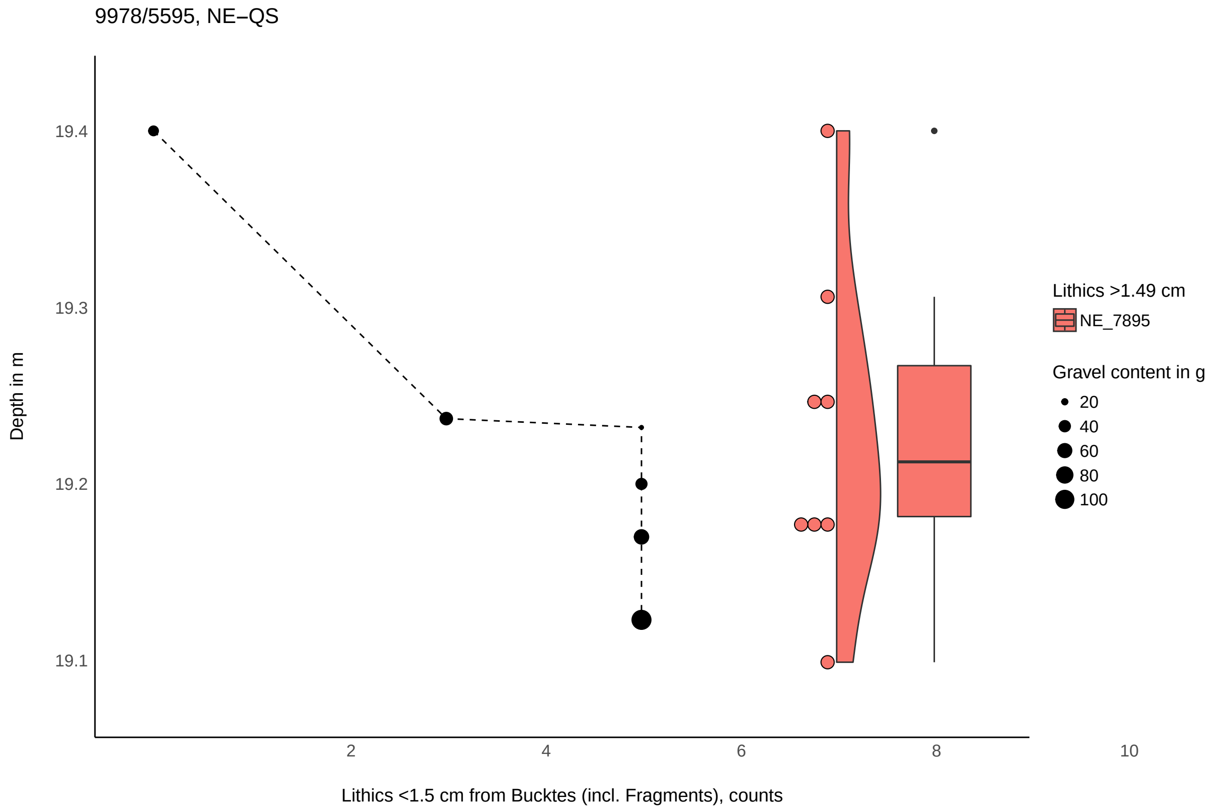

Supplementary Figure S18.

2.1.2 Square 9976/5594

2.1.2.1 9976/5594 North-East-Quarter Square - Top removed by excavator

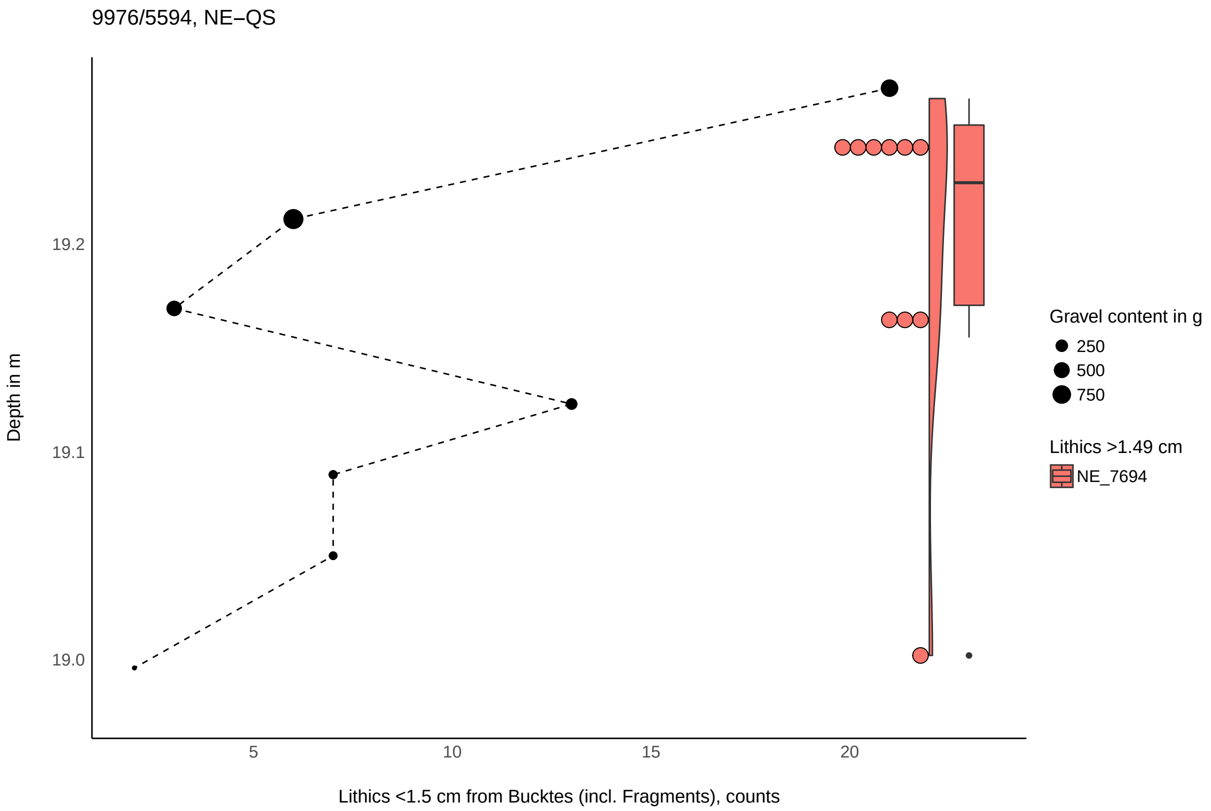

Supplementary Figure S19.

2.1.2.2 9976/5594 North-West-Quarter Square - Top removed by excavator

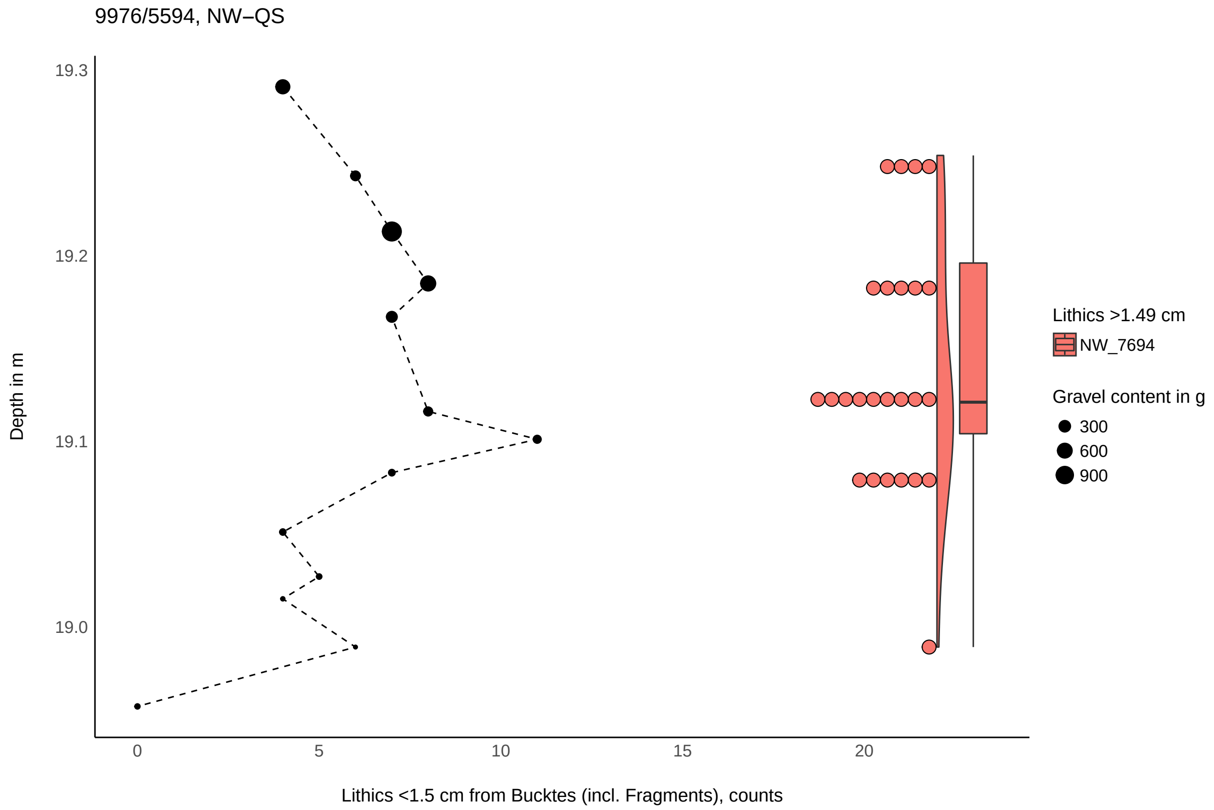

Supplementary Figure S20.

2.1.2.3 9976/5594 South-East-Quarter Square - Top removed by excavator

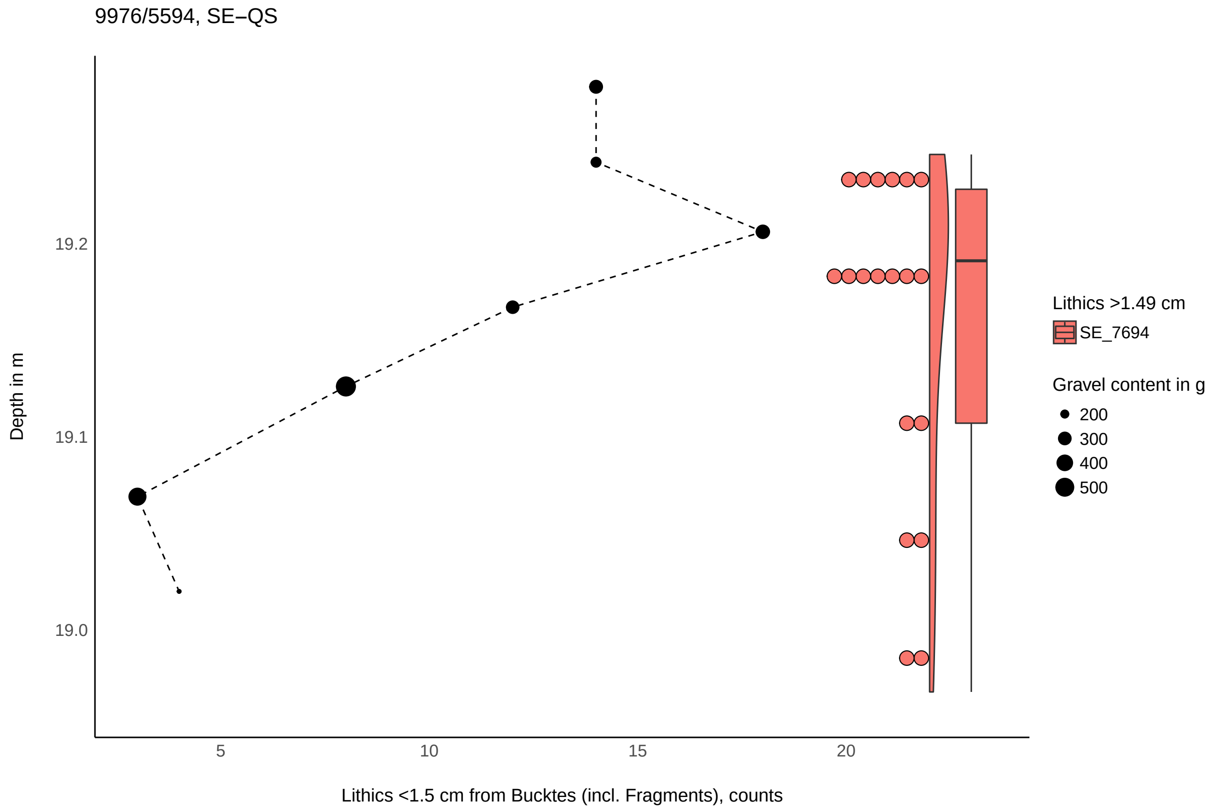

Supplementary Figure S21.

2.1.2.4 9976/5594 South-West-Quarter Square - Top removed by excavator

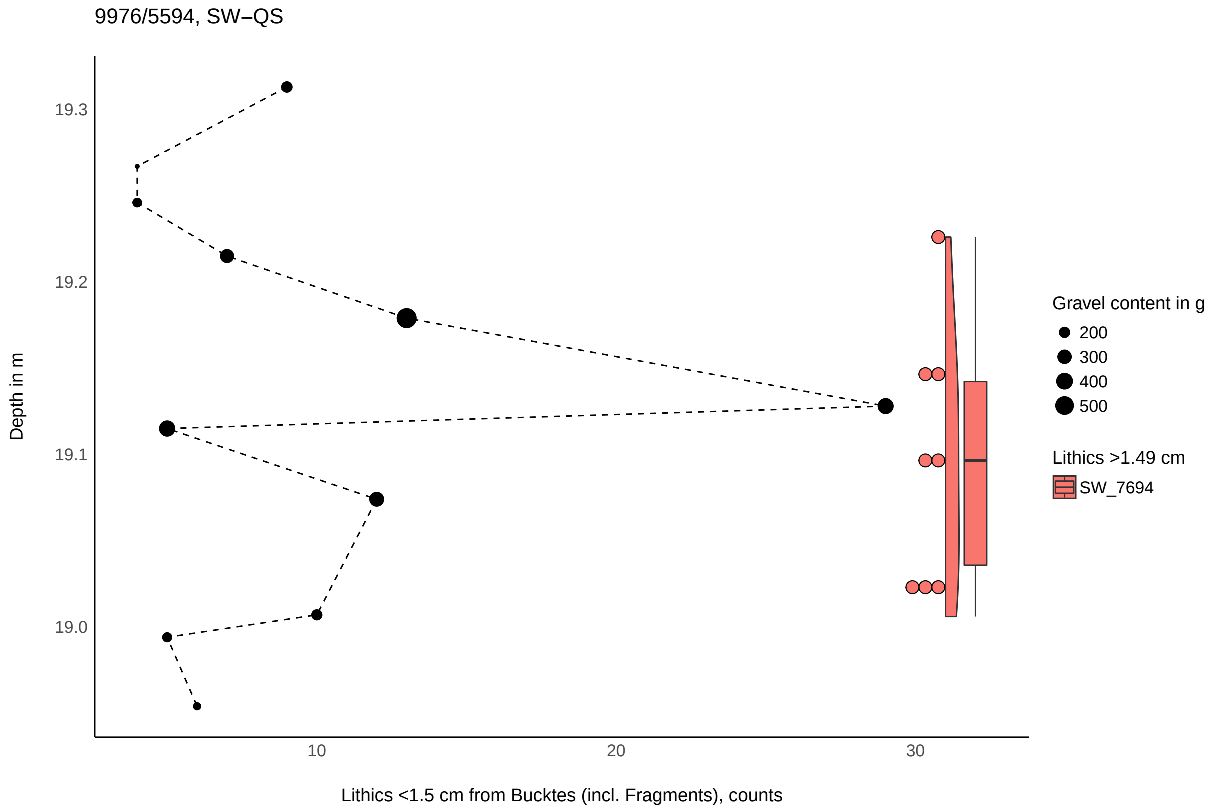

Supplementary Figure S22.

2.1.3 Square 9977/5594

2.1.3.1 9977/5594 North-West-Quarter Square - Top removed by excavator

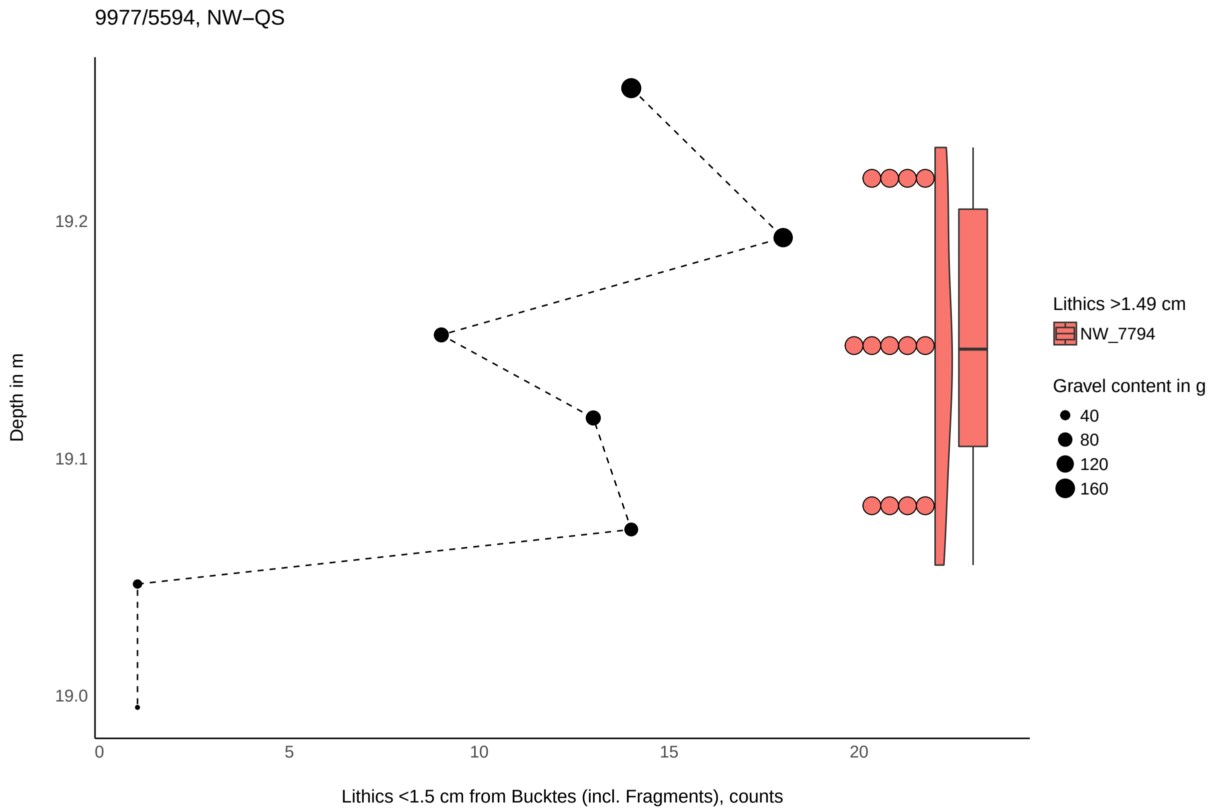

Supplementary Figure S23.

2.1.3.2 9977/5594 South-West-Quarter Square - Top removed by excavator

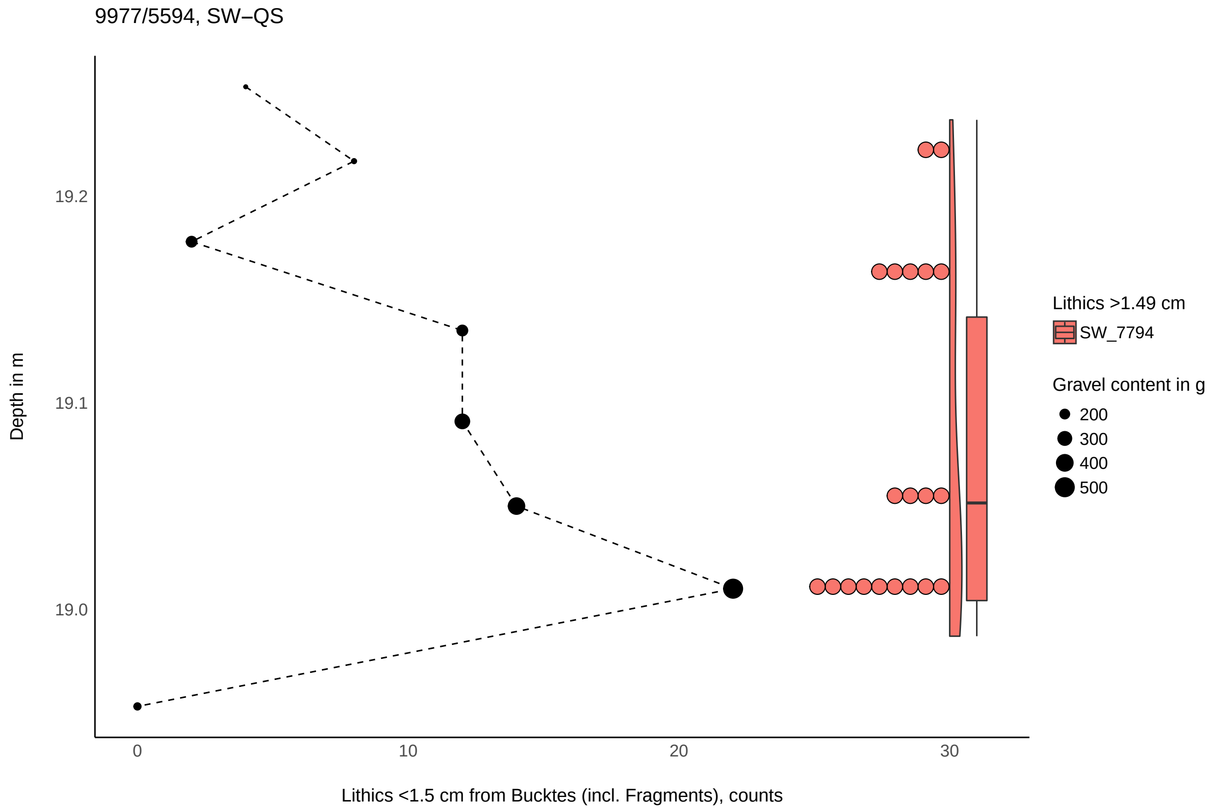

Supplementary Figure S24.

2.1.4 Square 9979/5595

2.1.4.1 9979/5595 North-West Quarter Square

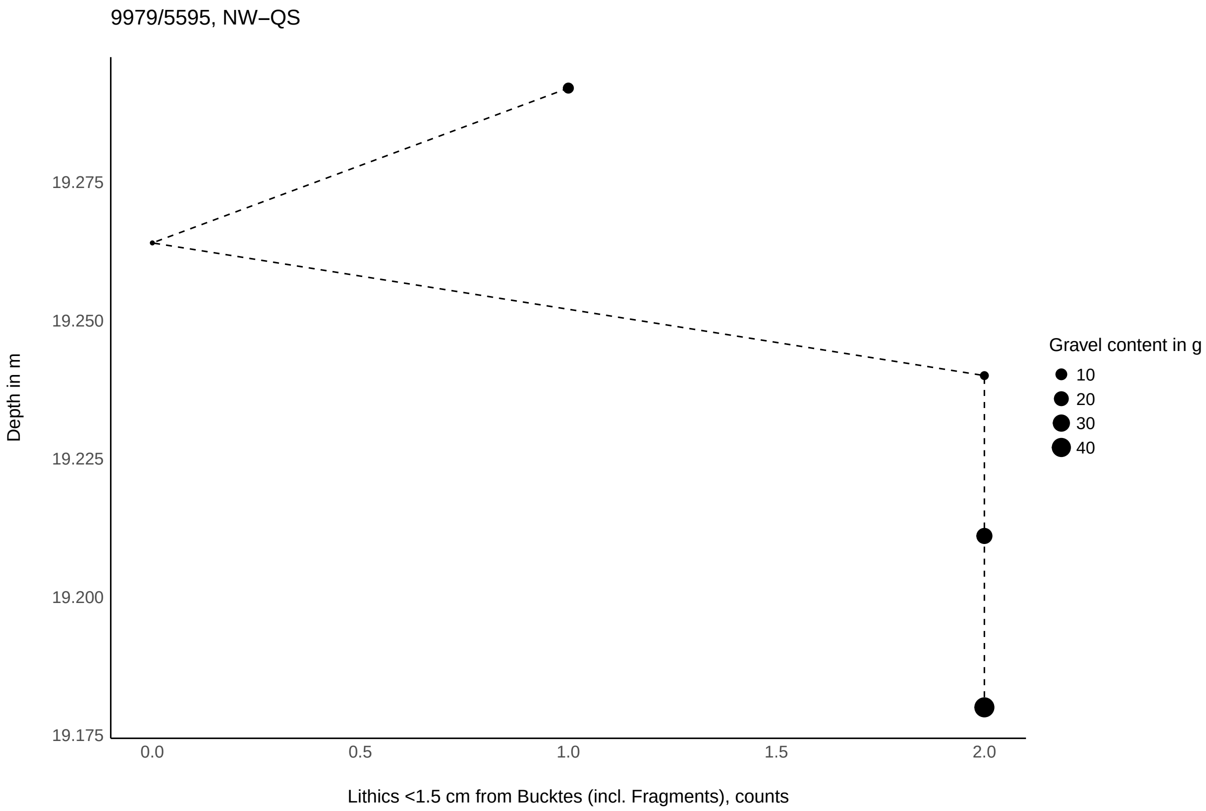

Supplementary Figure S25.

2.1.5 Lithic counts <1.5 cm from all squares

To summarize, the small lithics from all squares are plotted below (Figure S26). The diagramm indicates that the lithic counts decrease towards the suspected paleoshore in the East. This may be due to human behavior and the spatial distribution of the artefacts at the site. On the other hand, this could be an artefact of the excavation circumstances, as we had to stop at a specific depth due to the ground water table. It may be that the artefact concetrations of the find horizon dipped down towards the paleoshore, but we could not reach them. We will check this in a future campaign when the ground water table is lower.

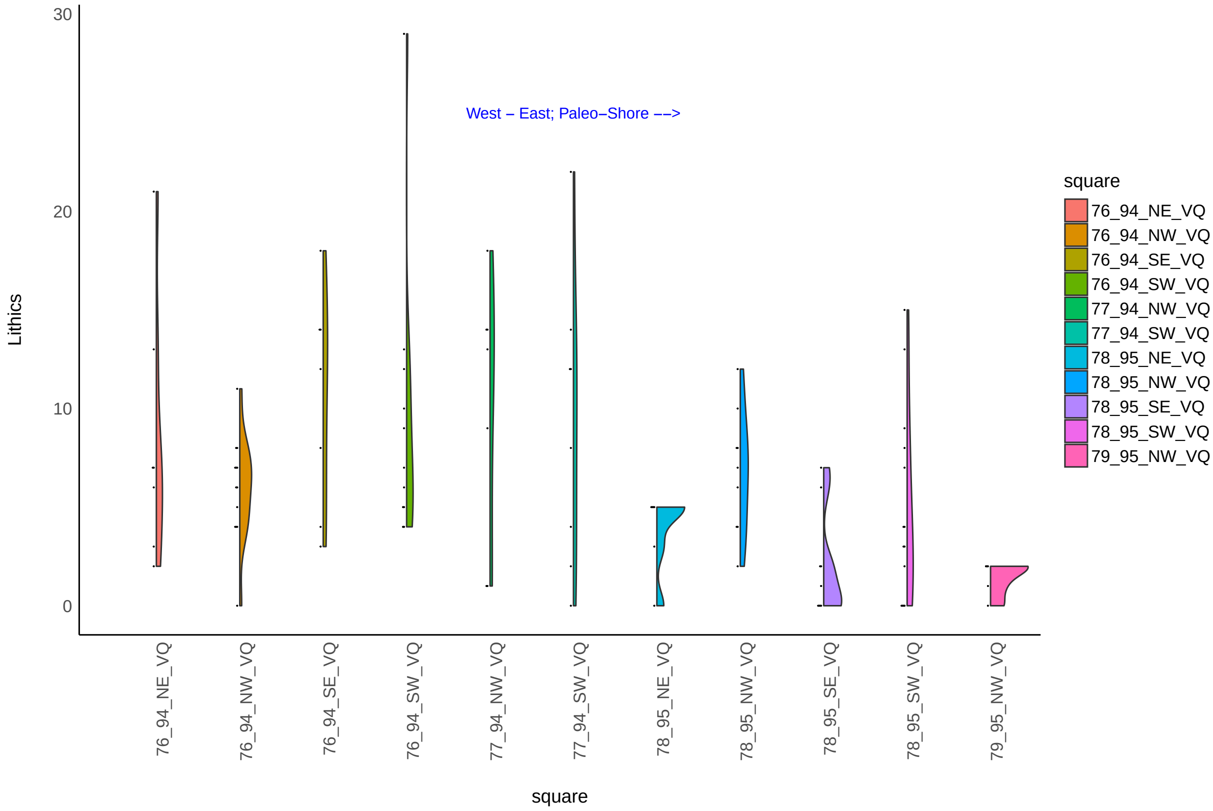

Supplementary Figure S26.

2.2 Further inspection of lithics and depth

2.2.1 The relationship between artefact <1.5 cm counts and Z

The results of a linear model reveal a relationship between small lithic counts and depth:

```
##
## Call:
## lm(formula = All_Buckets$Lithics ~ All_Buckets$Z)
##
## Residuals:
##     Min      1Q  Median      3Q     Max
## -8.893 -3.986 -1.390  2.675 21.803
##
## Coefficients:
```

```
##              Estimate Std. Error t value Pr(>|t|)
## (Intercept)    192.469     91.220   2.110   0.0375 *
## All_Buckets$Z   -9.686      4.754  -2.038   0.0444 *
## ---
## Signif. codes:  0 '***' 0.001 '**' 0.01 '*' 0.05 '.' 0.1 ' ' 1
##
## Residual standard error: 5.466 on 94 degrees of freedom
## Multiple R-squared:  0.0423, Adjusted R-squared:  0.03211
## F-statistic: 4.152 on 1 and 94 DF,  p-value: 0.0444
```

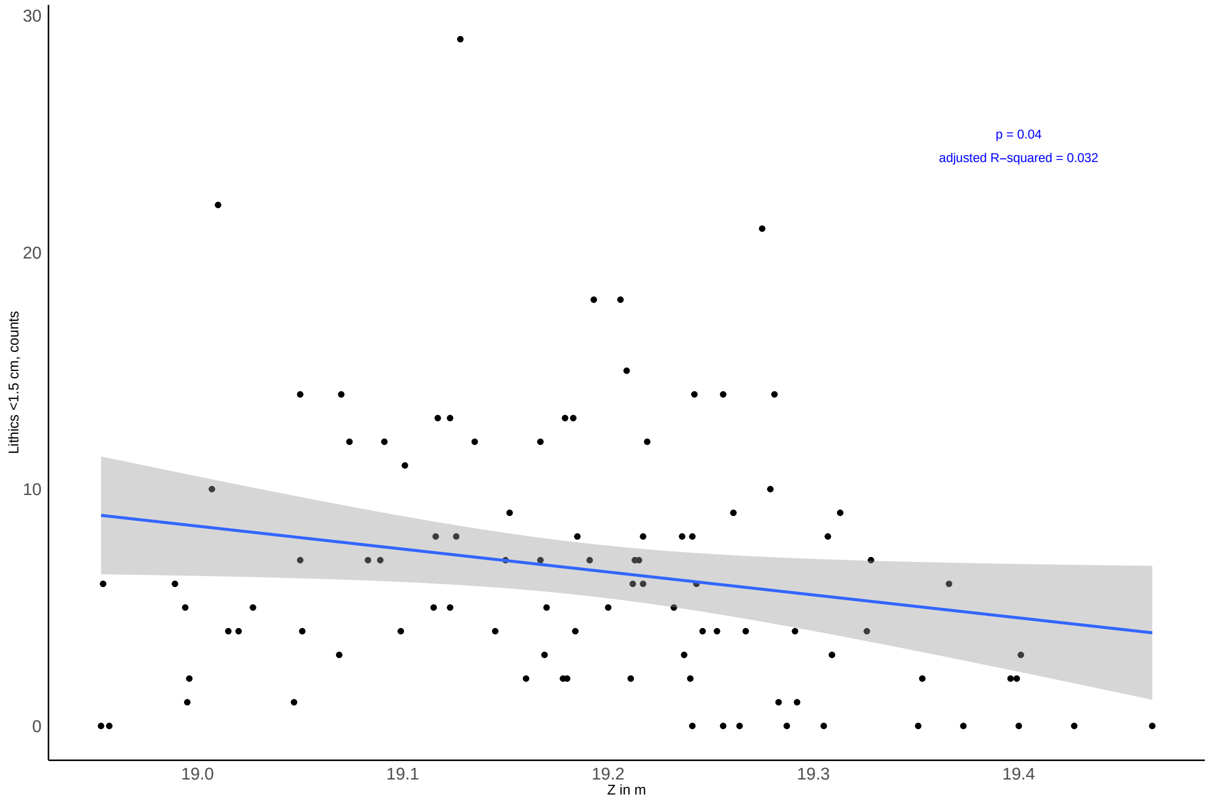

Supplementary Figure S27. The relationship between small artefact <1.5 cm counts and depth.

The plot of the linear model in Figure S27 shows that there is a significant relationship (at a p-value of 0.05) between the small find counts and depth.

This result is further reinforced by the following plot (Figure S28) of the small lithic counts from all quarter squares and depth. Here, a convex hull illustrates the distribution range.

The results indicate that there is a find horizon within the humic sand around a depth of Z = 19.2 m. However, the small artefacts scatter within the entire range. This may be due to small lithics beeing more prone to disclocation within the sediment than the larger artefacts. Therefore, we need to look again at the distribution of artefacts >1.49 cm within the humic sand:

2.2.2 Artefacts >1.49 cm and depth

From the plots above (Figures S15-S25) we gain the impression that the large finds are also distributed somewhat randomly within the humic sand. Therfore, let's plot all the large finds

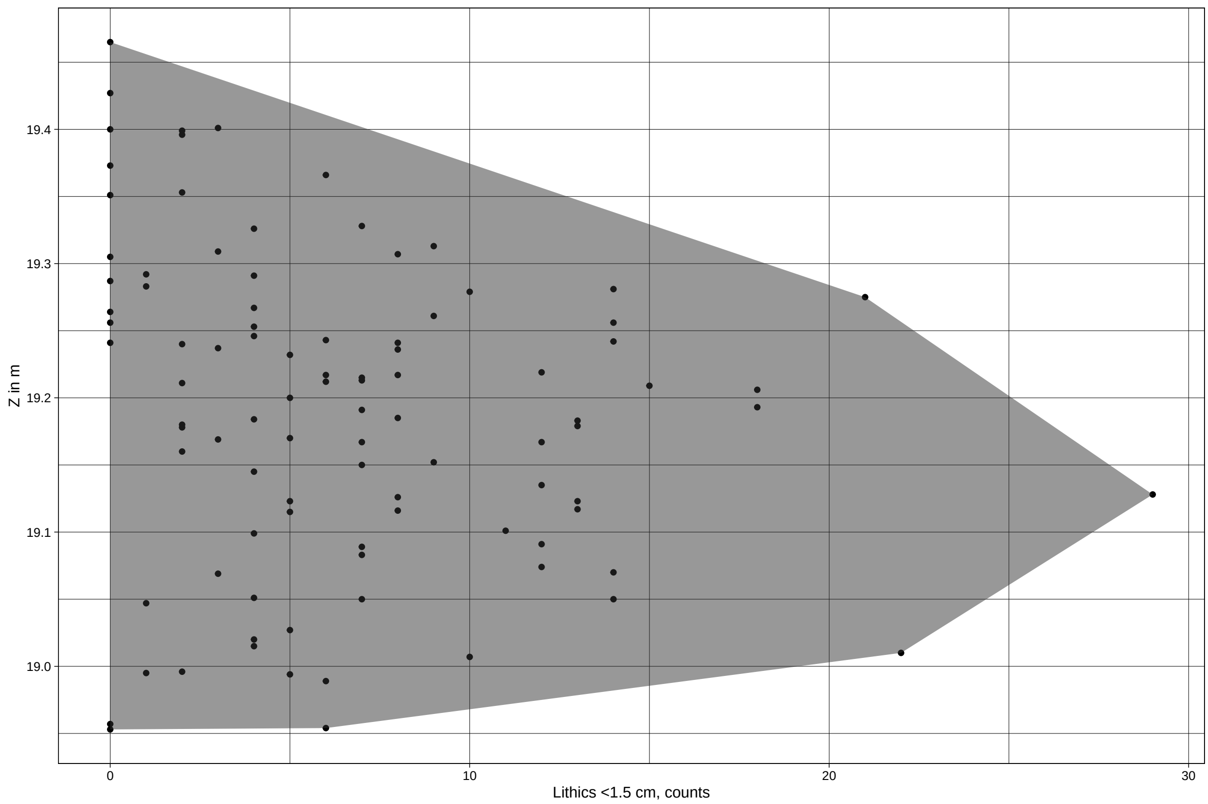

Supplementary Figure S28. Small artefact <1.5 cm counts and depth.

together (We included the artefacts found in the test excavation 2019 and the lithics from the 2020 campaign.), illustrated in Figure S29.

Comparable to the results for the small lithics, the plot in Figure S29 shows that most artefacts >1.49 cm are concentrated between Z = 19.09 m and Z = 19.24 m. Let's take a closer look at the distribution:

```
##    Min. 1st Qu.  Median    Mean 3rd Qu.    Max.
##   18.84   19.09   19.17   19.17   19.24   19.55
```

With this result, we can infer the existence of a concentrated find horizon that ranges within 15 cm.

2.2.3 The the depth distribution of artefacts >1.49 cm weight

With the assumption that lighter artefacts are more prone to dislocation within the sandy sediment, the distribution of the heavier pieces could help to narrow down the range of the main find horizon. Therefore, we analyze in the following the depth distribution of artefacts regarding their weight. Therefore, we divided the artefacts in heavy lihics (>9.9 g) and light lithics (>10 g). We included the artefacts found in the test excavation 2019 and the lithics from the 2020 campaign.

As illsutrated by the plot (Figure S30), the light artefacts are distributed as follows:

```
##    Min. 1st Qu.  Median    Mean 3rd Qu.    Max.
##   18.91   19.09   19.17   19.17   19.24   19.55
```

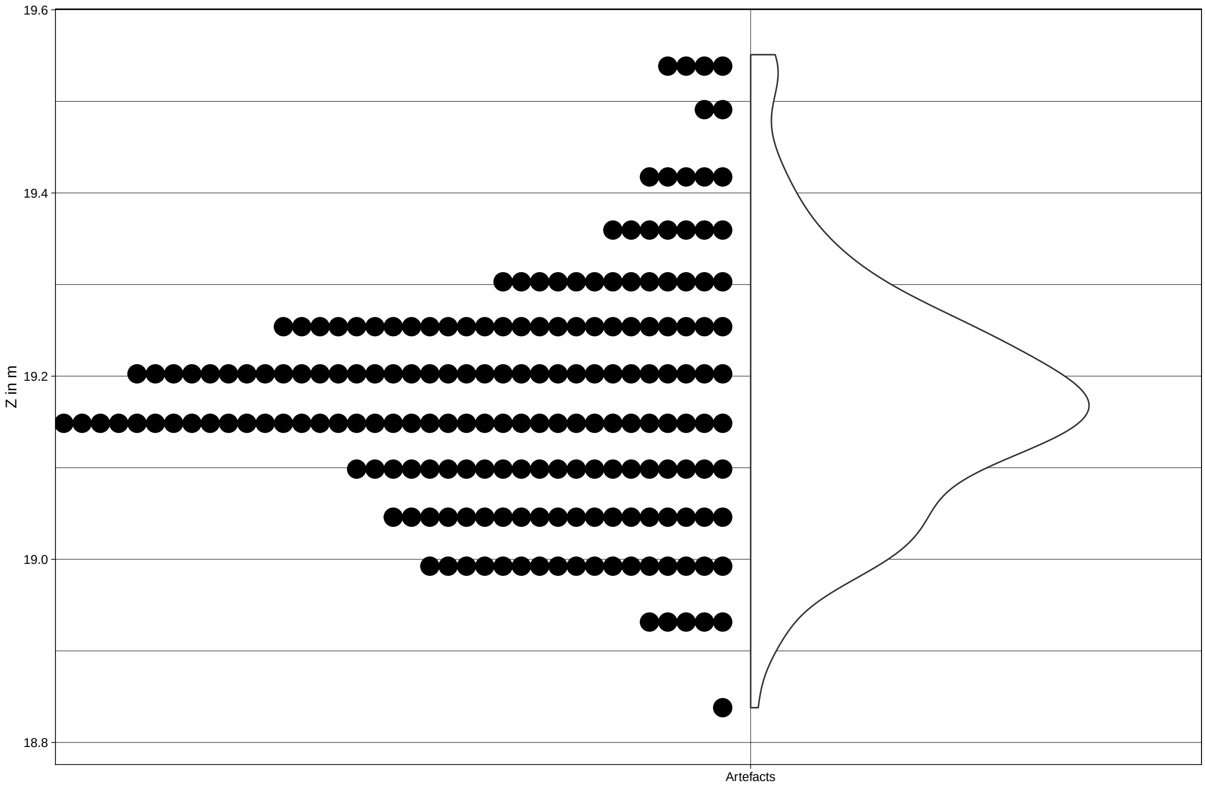

Supplementary Figure S29. Large artefacts >1.49 cm and depth

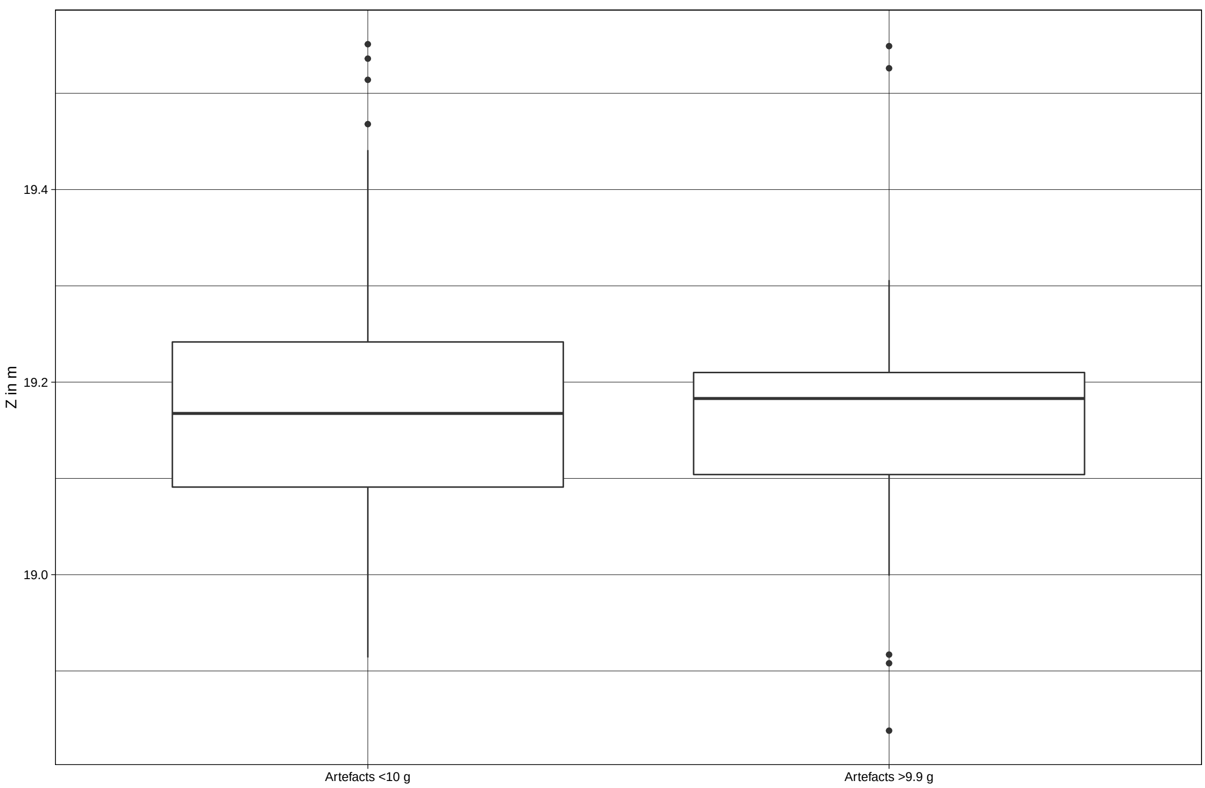

Supplementary Figure S30. Large Artefacs divided into light artefcats <10 g and heavier artefacts >9.9 g, and depth.

The heavier artefacts show a more narrow distribution between the 1st and the 3rd quartile:

```
##    Min. 1st Qu.  Median    Mean 3rd Qu.    Max.
##   18.84   19.10   19.18   19.16   19.21   19.55
```

These results let us slightly narrow down the main find horizon based on the heavier artefacts between Z = 19.10 m and Z = 19.21 m, indicating a thickness of 11 cm.

2.3 The relationship between gravel and lithic <1.5 cm counts

To analyze whether small lithics and the gravel content within the humic sand my be affected by similar post-depositional processes, we take a look at the linear relationship of gravel content in g of each bucket and the resspective small lithic counts.

The linear model of the relationship between small lithic counts and gravel content reveals a significant result:

```
##
## Call:
## lm(formula = All_Buckets$Lithics ~ All_Buckets$Gravel)
##
## Residuals:
##      Min       1Q   Median       3Q      Max
## -10.6045  -3.4153  -0.9523   2.7464  20.0691
##
## Coefficients:
##                    Estimate Std. Error t value Pr(>|t|)
## (Intercept)        4.758911   0.669042   7.113 2.21e-10 ***
## All_Buckets$Gravel 0.011368   0.002597   4.378 3.10e-05 ***
## ---
## Signif. codes:  0 '***' 0.001 '**' 0.01 '*' 0.05 '.' 0.1 ' ' 1
##
## Residual standard error: 5.091 on 94 degrees of freedom
## Multiple R-squared:  0.1694, Adjusted R-squared:  0.1605
## F-statistic: 19.17 on 1 and 94 DF,  p-value: 3.105e-05
```

The plot in Figure S31 illustrates further that at a p-value of 0.05, there exists a linear relationship between the gravel content of the find horizon and the small finds. This indicates that small gravels and artefacts may have been affected by the same post-depositional processes.

But how is the data actually distributed? Let’s take a lok at another diagramm (Figure S32).

The graphs in Figure S32 show the distribution of the gravel content and the lithic counts in relation to depth. The polygons highlight the maximum values. The plot shows that the maximum lithic values in realtion to depth do not necessarily correlate 1:1 with the maximum gravel values. This indicates also a certain initial independence (before potential disturbances) of lithic accumulation by humans and natural gravel content. The three maximum values for small lithic counts match the 1st to 3rd quartiles (Z = 19.1 m to Z = 19.21 m, see above) for the Z values of the large finds. This lets us infer the orginal find horizon within this depth range.

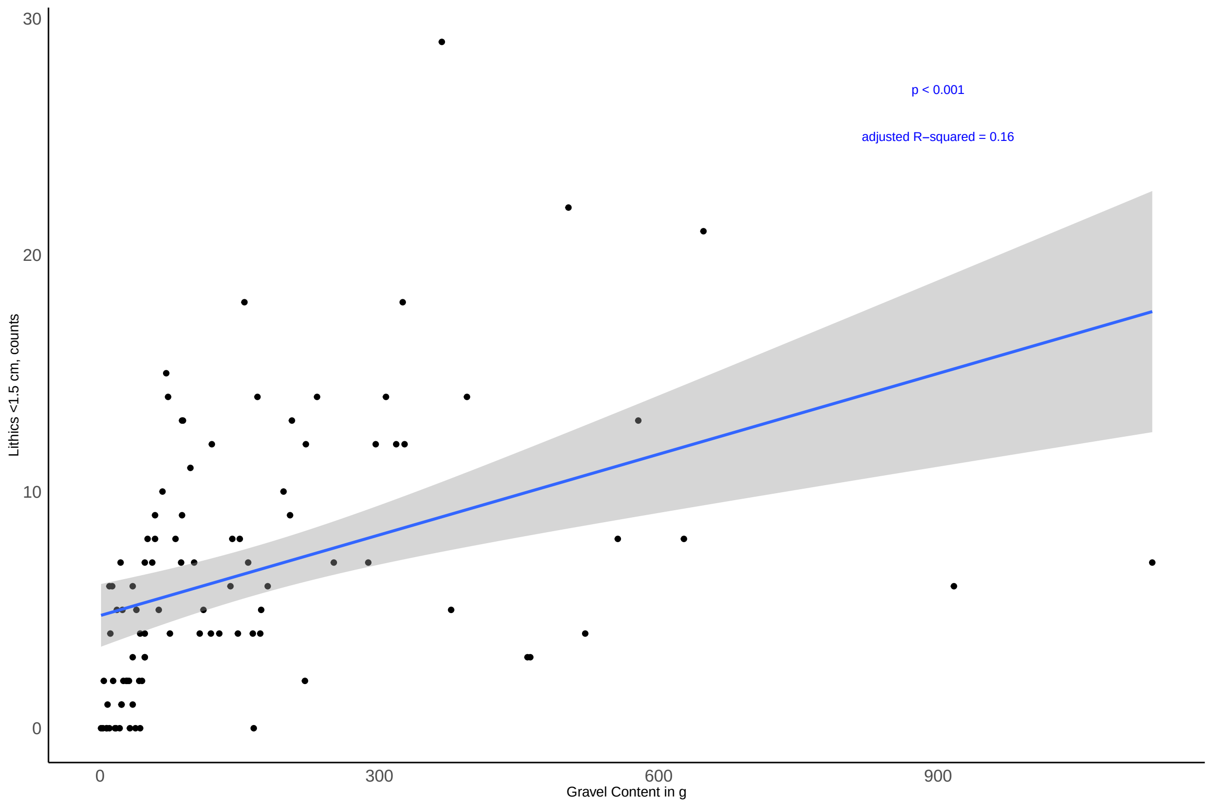

Supplementary Figure S31. The relationship between small lithic <1.5 cm counts and gravel content.

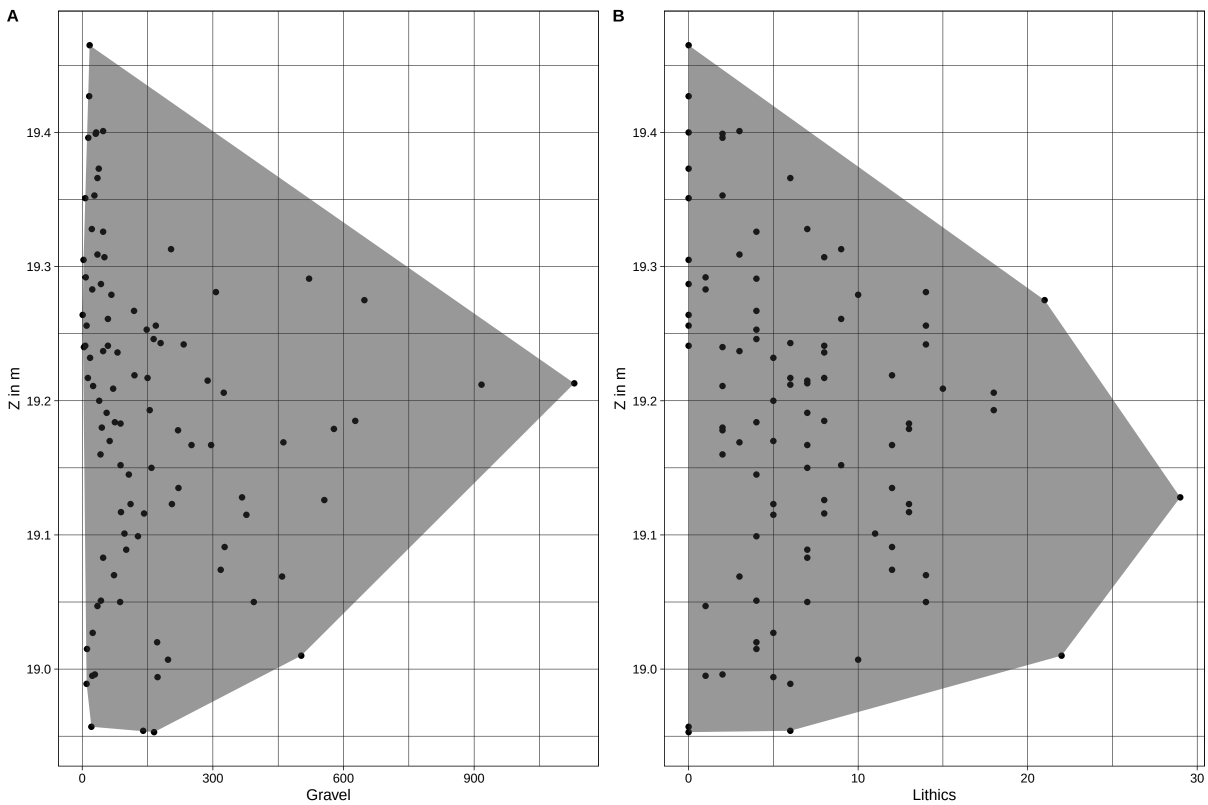

Supplementary Figure S32. The distribution of the gravel content and the lithic counts <1.5 cm in relation to depth.

Conclusion of Section 2.2 and Section 2.3

We can conclude that there exists a denser concetration of small and large artefacts between a depth of 19.10 m and Z = 19.21 m. However, the finds also scatter within the entire excavated depth and some post depositional dislocation needs to be taken into account. Further evidence for these processes comes from the gravel content of the sediment. A correalation of small finds and gravel content in relation to depth indicates that the objects where affected by similar post deposoitional processes within the humic sand. Nevertheless, the highest gravel contents and lithic counts do not correlate 1:1 with each other, indicating the remnants of original find distributions within the sediment.

2.4 Raw material size and Artefact size

An interesting feature of the Lichtenberg II assemblage is the small artefact size. To see if this corresponds to the local raw material, we did the following: We sampled quarter squares with high gravel content, the North-West quarter square 9976/5594, as well as the North-West quarter square 9977/5594 for baltic flint gravels and recorded the specimens. The aim was to evaluate raw material size of Baltic Flint that naturally occures within the find horizon. We included the flint artefacts found in the test excavation 2019 and the lithics (flint) from the 2020 campaign.

Comparison of weight

Weight is used here es an estimation of artefact and raw material size.

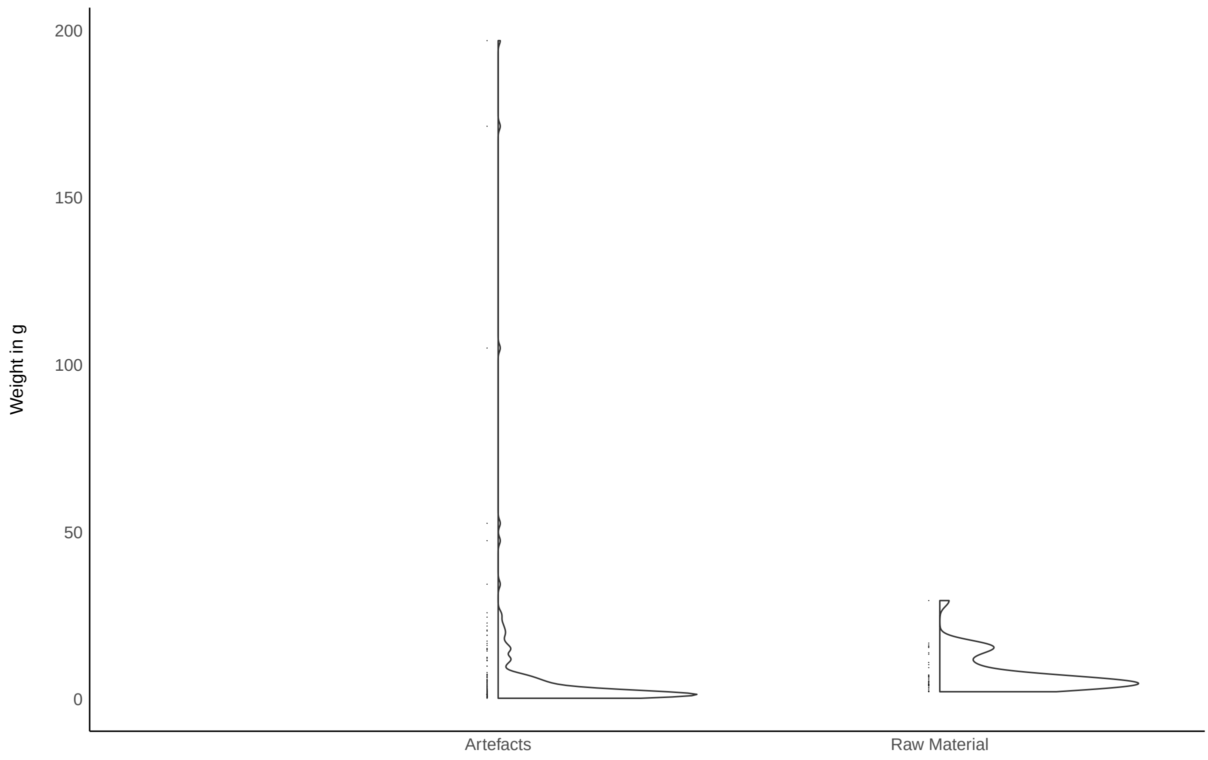

Supplementary Figure S33. The comparison of artefact and raw material weight.

The plot in Figure S33 illustrates that the ranges of raw material and artefact weight (i.e. size) largely overlap. We can infer that part of the archaeological assemblage was manufactured on the small raw material found at the site. Thereby, the artefacts reveal a smaller median weight value:

```
## [1] 2.2
```

than the raw material:

```
## [1] 5.3
```

This is logical, as the assemblage consists of knapped cores (reduced nodules) and light flakes and tools.

But the assemblage includes also some larger artefacts, e.g., a large quartzite flake (not included in the plot) or a flint core. This indicates that humans where able to access and collect larger raw material from the surrounding landscape which they transported to the site.

Section 3: Artefacts Lichtenberg I and Lichtenberg II

In the following analysis we focus mainly on the artifacts from Lichtenberg II, as the material from Lichtenberg I was already published elsewhere (Veil et al., 1994; Weiss, 2020).

This section was written in Rmarkdown.

3.1 Rawmaterial Lichtenberg II

Table S1 shows that we have a raw material diversity in Lichtenberg II, relative to Lichtenberg I where all artifacts where made of Baltic Flint (Veil et al., 1994).

Although beeing small, the quality of the raw material was good, as most artifacts show no special raw material features (Table S2).

3.2 Classification Lichtenberg II

Table S3 shows the classification of the n=192 Lichtenberg II artefacts. The assemblage is dominated by flakes, followed by cores and flake tools. The latter two have the same numbers. The assemblage consists further of shattered pieces and coretools. We also found 3 manuports and one piece typed as 'other' which are most likely raw material imports and/or hammerstones. If we exclude manuports, other and shatter, the assemblage of 163 artefacts consist of 51.5% flakes, 30.1% tools and 18.4% cores. This is a relatively high share of tools compared to Lichtenberg I (18.8% (Veil et al., 1994)).

3.3 Classification Lichtenberg I

During our fieldwork in 2019, we recovered the small number of 20 artefacts from the find horizon of Lichtenberg I, summarized in Table S4. The assemblage consists mainly of flakes, one of which is potentially the product of bifacial production (see main text). The low number of artitfacts is explained by the fact that the main find concentration has already been excavated

Supplementary Table S1. Rawmaterial Lichtenberg II. Included are also manuports and a potential hammer stone (category: 'other')

Raw Material	n
FLINT	184
IronConc	1
Porphyry	1
Quartzite	5
Quartzite(?)	1

Supplementary Table S2. Rawmaterial characteristics Lichtenberg II

Raw Material Characteristics	n
BRYOZOANS	9
EXTENSIVE FROSTCRACK	1
FOSSIL	1
GRANULAR	14
INTRUSIONS_FLAWS	23
NONE	130
THERMAL_FRACTURES	14

Supplementary Table S3. Classification Lichtenberg II

Classification	n
CORE	30
CORETOOL	18
FLAKE	84
FLAKETOOL	31
MANUPORT	3
OTHER	1
SHATTER	25

before (Veil et al., 1994). Additionally, we recovered one Keilmesser and one tool fragment in the find horizon below the 1987-1993 excavation during our initial sondage in 2017 (Table S4).

3.4 Size

During our excavation of Lichtenberg II, we already recognized the small size of the artefacts. Therefore, we set the usual 2 cm size cut-off for single recorded artefacts to 1.5 cm. In the following, we first present the size of artefacts from Lichtenberg II and I (2019) and compare Lichtenbverg II in the next steps to a sample from Lichtenberg I (1987-1993), as well as diachronically to other Central European assemblages.

3.4.1 Lichtenberg II

Cores and coretools show a similar range of size, potentially directly dependent of the small sized raw material (see SI 3 - Analysis of the find horizon Lichtenberg II). Secondary and subsequent products within the operational chain, i.e. flakes, flaketools and shattered pieces are smaller than the latter two. The median dimensions are all below 3 cm, as presented in Table S5.

Supplementary Table S4. Classification Lichtenberg I

Classification	n
CORE	3
FLAKE	17
TOOL	2

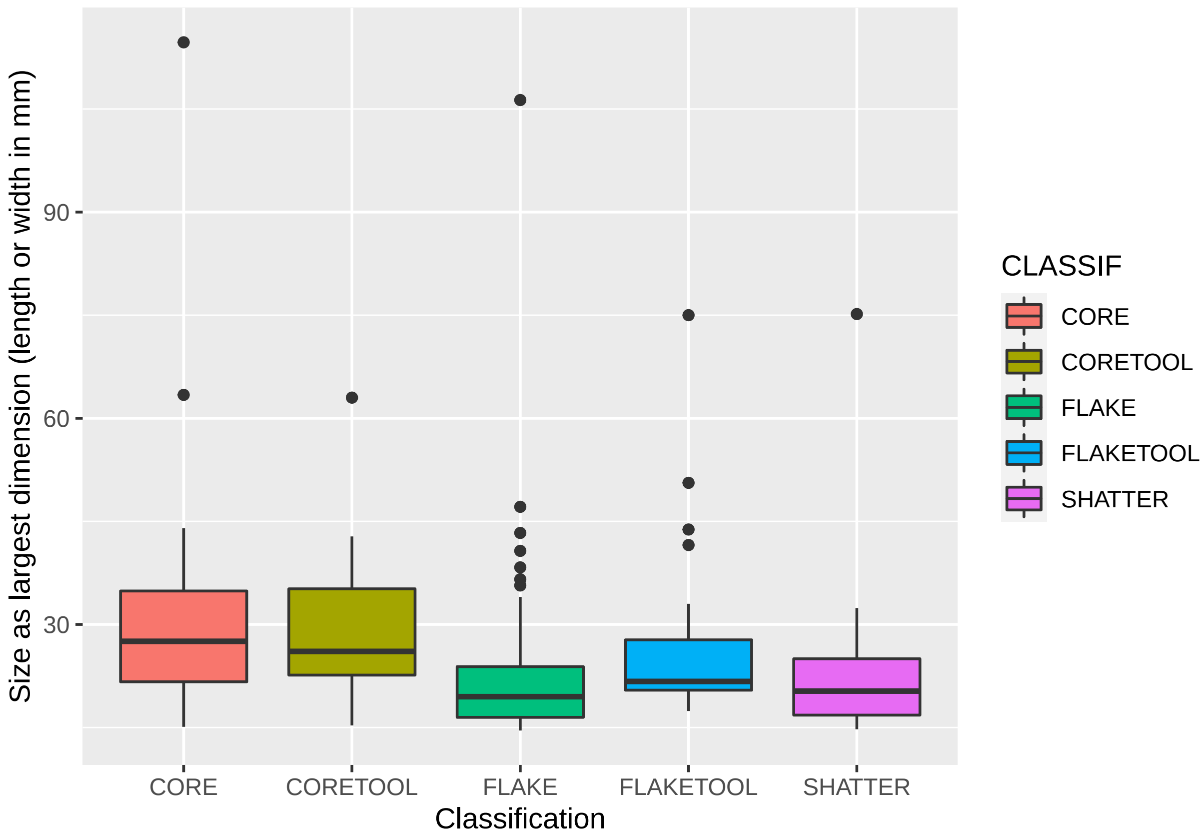

Supplementary Figure S34. Artefact size Lichtenberg II.

Supplementary Table S5. Artefact Size Lichtenberg II

CLASSIF	n	Median_Dimension
CORE	30	27.54
CORETOOL	18	26.07
FLAKE	84	19.48
FLAKETOOL	31	21.70
SHATTER	25	20.30

Supplementary Table S6. Artefact Size Lichtenberg I - new excavation

CLASSIFICATION	n	Median_Dimension
CORE	3	33.2
FLAKE	17	19.8

3.4.2 Lichtenberg I

During our fieldwork in 2019, we disovered 20 cores and flakes (Table S4). This is a too small number for a reliable estimation of artefact size. The median size data is presented in Table S6, but will not be used for further comparison (see below).

3.4.3 Size comparison of Lichtenberg I and II

As stated above, we cannot use the Lichtenberg I (2019) artefacts for a reliable comparison of size. To illustrate the size differences between Lichtenberg I and II, we use a dataset of recently published Lichtenberg I Keilmesser (and one handaxe (Weiss, 2020)) instead. Additionally, we use the data of 88 large flakes from the 1987-1993 excavation to demonstrate the maximum possible size difference for the flakes and in consequence for the raw material.

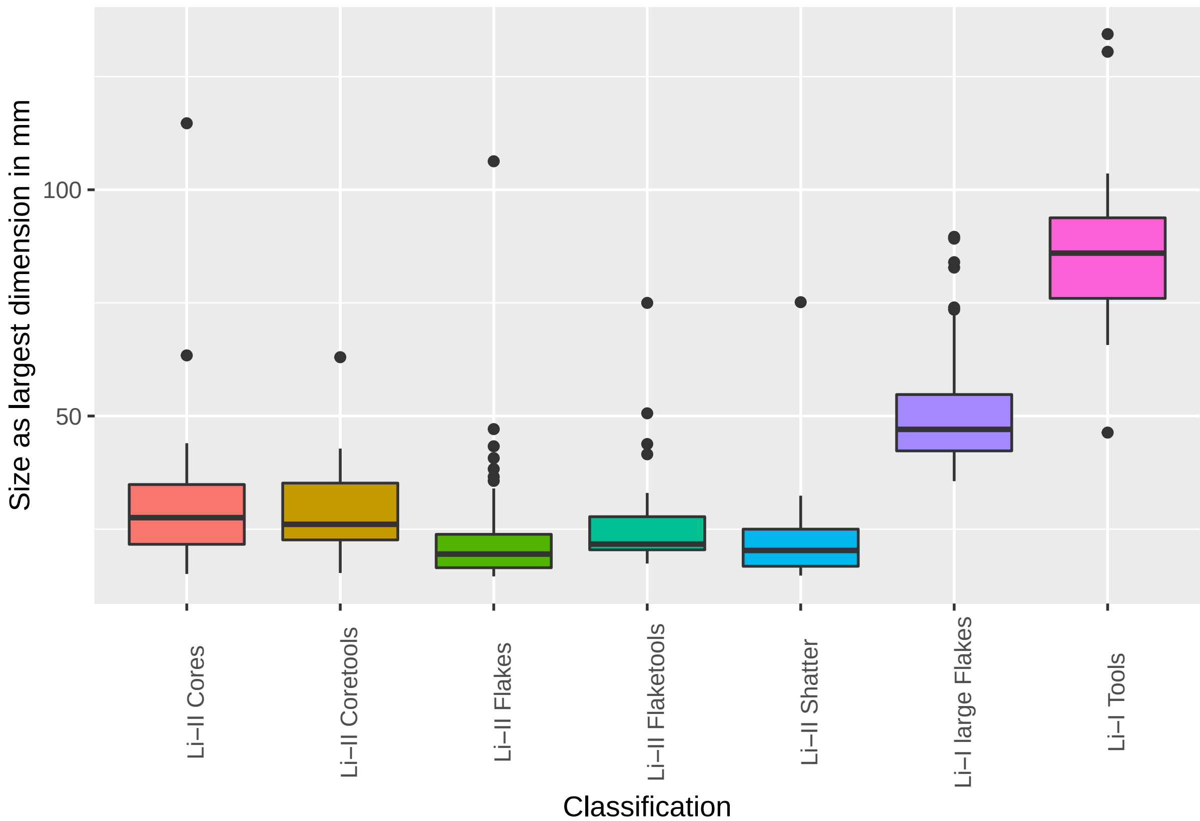

Supplementary Figure S35. Artifact size Lichtenberg I and I.

The plot in Fig. S35 demonstrates the artefact size difference of the Lichtenberg I and II assemblages. The mean values for the median size values of the Lichtenberg I flakes and tools are displayed in Table S7. Although we did not include the data for small flakes (between 1.5 cm and 3 cm) from Lichtenberg I, the large flakes exceed by far the main flake size distribution of Lichtenberg II. The large tools from Lichtenberg II demonstrate even more drastic the

Supplementary Table S7. Artefact size Lichtenberg I (large flakes only), 1983-1993 excavation

Classification	n	Median_Dimension
FLAKE	88	47.05
Tool_Li_I	23	86.00

differences in artefact (and -in the end- raw material) size between Lichtenberg I and II.

3.4.4 Diachronic size comparison of Lichtenberg II and other Central European assemblages between MIS 5e and MIS 3

To analyze if Lichtenberg II can in fact be characterized as a small artefact assemblage, we compared the size of flakes to other Central to Eastern Central European sites. The data was mainly collected by one of us (MW) and was previously published in Weiss et al. 2017 (Weiss et al., 2017) and in Weiss & Weber 2019 (Weiss and Weber, 2019). As for the other assemblages only complete artefacts >1.99 cm where measured, we adjusted the flake data from Lichtenberg accordingly. We incorporated the following assemblages from the Eemian: Taubach, Thuringia/Germany (Bratlund, 1999), Neumark-Nord, Saxony-Anhalt/Germany (Gaudzinski-Windheuser and Roebroeks, 2014) and Rabutz, Saxony/Germany (Toepfer, 1958). From MIS 5a, we included: Königsaue, Saxony-Anhalt/Germany (Mania and Toepfer, 1973), Khotylevo I, Russian Federation (Hein et al., 2020), and Wroław-Hallera-Avenue Lower Find layer, Poland (Wiśniewski et al., 2013). Salzgitter-Lebenstedt, Lower-Saxony /Germany (Pastoors, 2001; Tode, 1982) dates either to the MIS 5a/ MIS 4 transition or to early MIS 3. From the latter time period, we included: Pouch, Saxony-Anhalt/Germany (Weiss, 2015), and the Upper Find layer of Wroław-Hallera-Avenue, Poland (Wiśniewski et al., 2013).

The plot in Figure S36 shows that Lichtenberg II has the smallest flakes of all assemblages, followed by the Eemian sites. There is a general trend that flakes get larger during MIS 5a and early MIS 3. That smaller artefact assemblages in the latter two time periods are raw material related, was recently shown in a study by Weiss et al. (Weiss et al., 2017): in Königsaue, it seems that nodules where pre-shaped at the raw material outcrop and the then smaller initial cores where transported to the lake site. Second, in Wrocław-Hallera-Avenue, only small sized nodules occur naturally (Weiss et al., 2017; Wiśniewski et al., 2013). Generally, we can tentatively infer that during periods with high plantcover (Eemian, Brörup) raw material was rather small sized, and good quality raw material may have been harder to access than in time periods with less plant cover (MIS 3, MIS 5a/ MIS 4 transition). During the latter, large sized raw material was accessible in erosional channels or braided river valleys, like, e.g., in Pouch (Weiss, 2015).

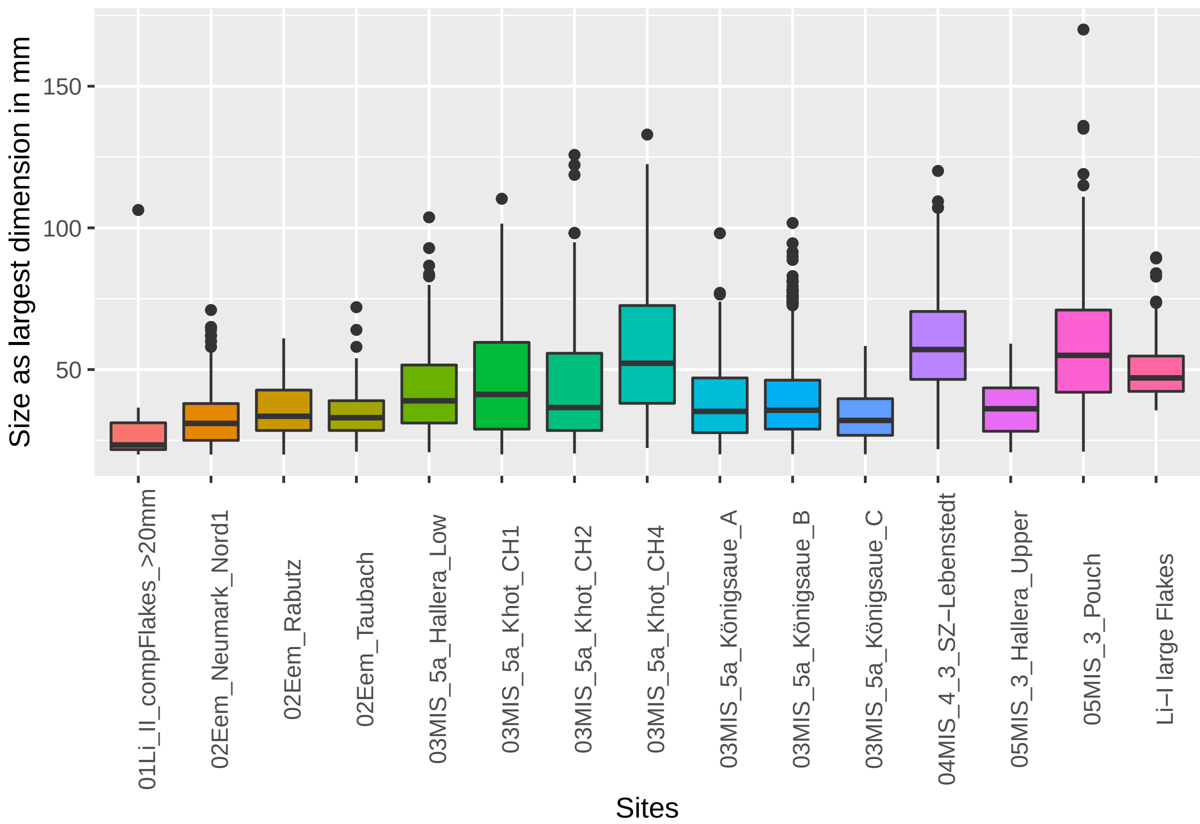

Supplementary Figure S36. Flake size comparison between Lichtenberg II and other cnetral European assemblages, dating between MIS 5e and MIS 3.

3.5 Lichtenberg II: Cores

The main attributes of the cores are listed in the following. Inclcuded are also cores that were transformed into tools in a subsequent step. “NA” values are excluded.

- Amount of secondary (worked) surface on the cores:
  - “10-30%”: n=14, 35%
  - “40-60%”: n=15, 37.5%
  - “70-90%”: n=9, 22.5%
  - “100%”: n=2, 5%

- Number of flaking surfaces:
  - “0”: n=1, 2.5%
  - “1”: n=19, 47.5%
  - “2”: n=13, 32.5%
  - “3”: n=6, 15%
  - “4”: n=1, 2.5%

- Number of flake scars:
  - “1”: n=14, 35%
  - “2”: n=3, 7.5%
  - “3”: n=6, 15%
  - “4”: n=8, 20%
  - “5”: n=7, 17.5%
  - “6”: n=1, 2.5%
  - “7”: n=1, 2.5%

- Flaking directions (all flaking surfaces):
  - “Unidirectional”: n=54, 80.6%
  - “Unidirectional and Lateral”: n=4, 6%
  - “Bidriectional”: n=7, 10.4%
  - “Concentric”: n=2, 3%

- State of the striking platform:
  - “Primary (i.e. natural) Surface”: n=20, 51.3%
  - “Plain”: n=17, 43.6%
  - “Coarse prepared (~2 large scars)”: n=2, 5.1%

- Exploitation:
  - “Tested Nodule”: n=20, 50%
  - “Flaking Core”: n=9, 22.5%
  - “Exhausted Core”: n=11, 27.5%

Summarizing the data provided above, we can say that most cores:

1. are knapped on half of their entire surface
2. have one or two flaking surfaces
3. have mainly only a single flake scar, but 3 to 5 flake scars are also common
4. are knapped unidriectionally
5. have ntaural or plain striking surfaces (no facetting!)
6. are either flaked a single time or exhausted

This leads to the conclusion that simple flaking methods dominate the blank production in Lichtenberg II. Core preparation is not common, if not entirely missing. The simple and sometimes just once knapped cores may also be due to the small raw material size, as some nodules make only one-time flaking possible. This is confirmed by the model illustrated below, showing that core length and the number of flake scars are significantly related (at a significance level of 0.05).

```
##
## Call:
## lm(formula = Core$LENGTH ~ Core$FLAKE_SCARS)
```

```
##
## Residuals:
##     Min      1Q  Median      3Q     Max
## -19.966  -7.111  -2.541   4.979  26.734
##
## Coefficients:
##                  Estimate Std. Error t value Pr(>|t|)
## (Intercept)       19.4647     3.1466   6.186 3.16e-07 ***
## Core$FLAKE_SCARS   2.1203     0.9199   2.305   0.0267 *
## ---
## Signif. codes:  0 '***' 0.001 '**' 0.01 '*' 0.05 '.' 0.1 ' ' 1
##
## Residual standard error: 10.07 on 38 degrees of freedom
##   (2 observations deleted due to missingness)
## Multiple R-squared:  0.1227, Adjusted R-squared:  0.09956
## F-statistic: 5.312 on 1 and 38 DF,  p-value: 0.02673
```

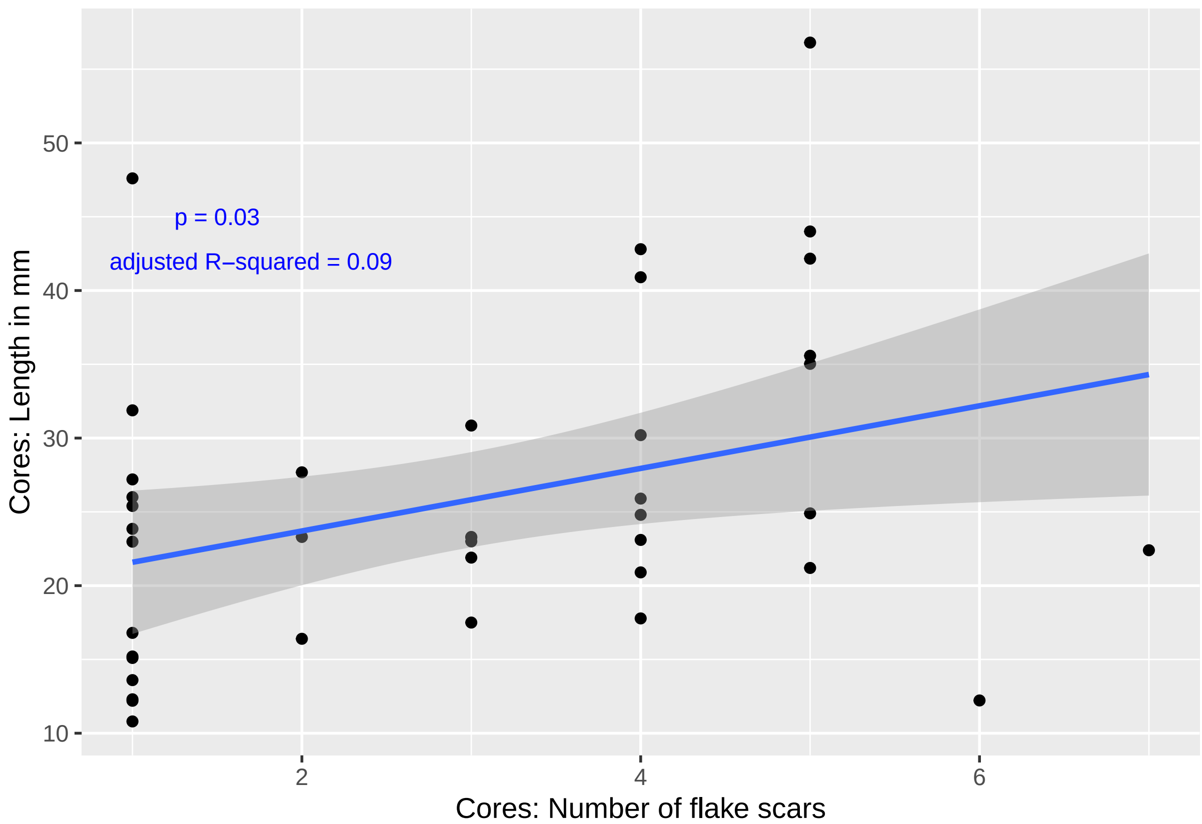

Supplementary Figure S37. The relationship between core length and flake scars.

3.6 Lichtenberg II: Flakes

The main attributes of the flakes are listed in the following. Included are n=55 complete flakes. "NA" values are excluded.

- State of the platform:
  - "Crushed": n=13, 23.6%
  - "Primary Surface": n=12, 21.8%
  - "Plain-NA" (natural or worked surface): n=10, 18.2%
  - "Plain-100%": n=18, 32.7%
  - "Scars-100%": n=1, 1.8%
  - "Removed": n=1, 1.8%

"Plain-100%" refers to platforms with one or two large negatives. "Scars-100%" refers to platforms that were prepared with 3 or more flake scars.

- Share of secondary (worked or artificial) surface on the dorsal face:
  - "0%" (natural surface): n=8, 15.1%
  - "10-30%": n=9, 17%
  - "40-60%": n=5, 9.4%
  - "70-90%": n=11, 20.7%
  - "100%": n=20, 37.7%

- Directions of the dorsal scars:
  - "Aligned" (i.e. same direction as ventral): n=23, 51.1%
  - "Lateral": n=9, 20%
  - "Opposed" (i.e., opposed to ventral): n=3, 6.7%
  - "Aligned and Lateral": n=5, 11.1%
  - "Bidirectional": n=3, 6.7%
  - "Bilateral": n=2, 4.4%
  - "Concentric": n=0, 0%

The platform attributes reinforce the observation made on the cores that striking platform preparation (i.e. Levallois sensu largo) was not common. Most of the flakes stem from an advanced state of core reduction, the share of fully cortical flakes is lower. This might be a reasonable distribution, as cores naturally produce a lower share of fully cortical flakes compared flakes with no or only remnants of natural surfaces. However, if we sum up all the flakes with remnants of natural surface on their dorsal face, we end up with 62.2% (compared to ~37.7% of non-cortical flakes). This is more than half of the flake population and may have its reason in the small size of the raw material. The observed dorsal scar directions on the flakes show the same trend as the flaking directions on the cores: the blank production in Lichtenberg II is dominated by unidirectional flaking.

3.7 Lichtenbergg II: Tools

The tools can be subdivided into 30 flaketools and 18 coretools.

- The tools where manufactured on diverse blank types:

Supplementary Table S8. Tool type size Lichtenberg II

TOOL_TYPE	n	Median_Length	Median_Width	Median_Thickness
BACKED_KNIFE	1	41.55	34.59	12.96
DENTICULATE	3	25.46	16.55	5.50
EDGE_RETOUCH	8	15.30	20.16	6.45
ENDSCRAPER	8	22.96	23.28	11.45
ENDSCRAPER_HAMMER	1	23.30	18.70	13.40
ENDSCRAPER_SCRAPER	1	14.30	27.90	16.40
HAMMERSTONE	3	40.90	26.80	19.20
NATBACK	1	21.90	14.80	13.00
NOTCH	11	24.80	19.50	11.60
POSS_USE	9	20.90	19.90	8.80
SCRAPER	2	24.85	23.65	7.50
NA	1	21.14	12.65	2.91

  - “Natural Piece”: n=2, 4.2%
  - “Flake”: n=30, 62.5%
  - “Core”: n=12, 25%
  - “Shatter”: n=4, 8.3%

- The typological classifications are presented in the following in alphabetical order:
  - “Backed Knife”: n=1, 2%
  - “Denticulate”: n=3, 6.3%
  - “Edge Retouch” (limited retouch, not scraper-like): n=8, 16.7%
  - “Endscraper”: n=8; 16.7%
  - “Endscraper, reused as hammerstone”: n=1, 2%
  - “Endscraper-Scraper”: n=1, 2%
  - “Hammerstone”: n=3, 6.3%
  - “Naturally Backed Knife”: n=1, 2%
  - “Notch”: n=11, 22.9%
  - “Scraper”: n=2, 4.2%
  - “Use-wear”: n=9, 18.8%

The tools from Lichtenberg II are dominated by flakes with use-wear, simple edge retouch and endscrapers. They were manufacture on a diversity of blanks, dominated by flakes. Endscrapers and endscraper combination tools were manufactured on thick blanks (Supplementary Table S8), indicating special functional requirements. Also, the rather steep endscraper edge can only be produced on a relatively thick blank. The high share of cores and shattered pieces that also served as blanks for tools indicate that recycling played an important role in the Lichtenberg II assemblage. For example, the artefact LIA-379 was initially a core and then reused as hammerstone (Supplementary Figure S38).

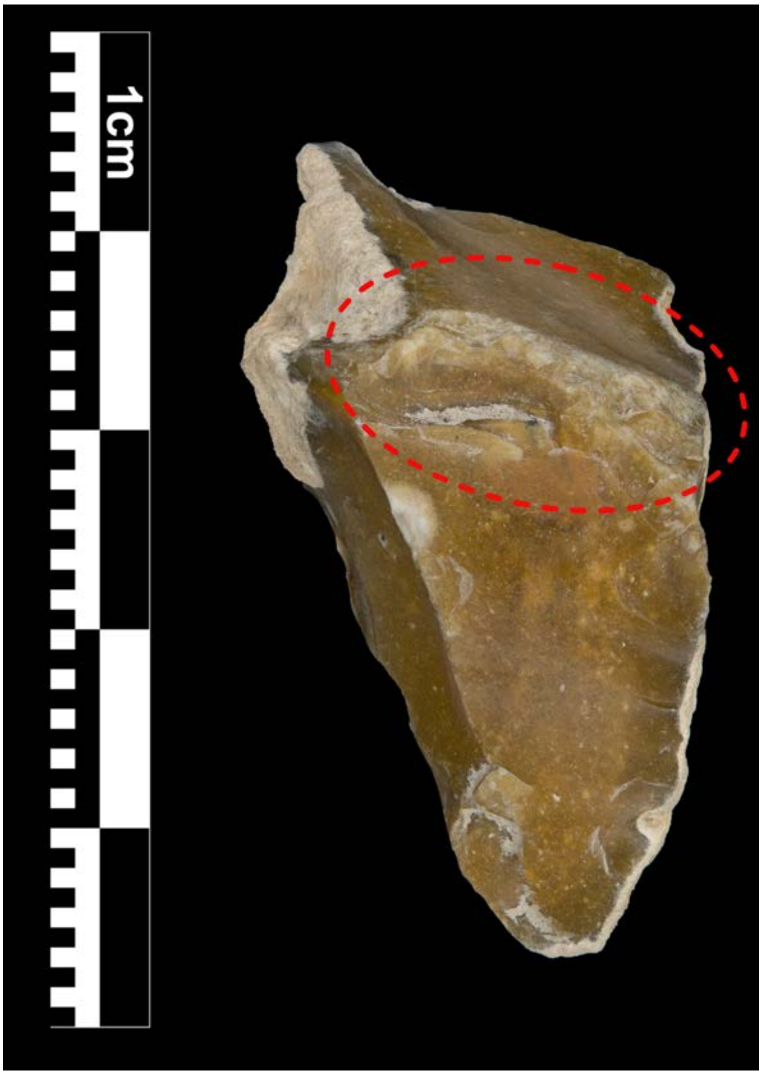

Supplementary Figure S38. Artefact LIA-379. Initially, it was a core. The battering marks (red circle) show that the core was recycled as hammerstone.

Supplementary Figure S39. Flake with edge retouch LIA-536 and edge retouched former core LIA-416.

Supplementary Figure S40. Naturally backed knife LIA-538. The blank was either a core or a natural piece that was shaped with a view strikes (blue arrows).

Supplementary Figure S41. Large quartzite flake LIA-513.

Supplementary Table S9. Selected attributes for Lichtenberg II

INVENTARNUMMER	RAWMAT	PRESERVATION	BLANK	CLASSIF	LENGTH	WIDTH	THICK	WEIGHT	PLATFORM	DORSALSCARS	DORSALDIRECT	TOOL_TYPE	AMOUNT_RETCORE	FLAKE_SUR	FLAKE_SCARS	CONDITION_STRIKE	FLAKING_DIR_A_B_C_D
LIA-097	FLINT	COMPLETE	FLAKE	FLAKE	16.56	28.62	4.71	2.15	CRUSHED	100%	BIDIRECTIONAL	NA	NA	NA	NA	NA	NA-NA-NA-NA
LIA-098	FLINT	COMPLETE	FLAKE	FLAKE	22.48	12.82	6.13	1.40	CRUSHED	100%	BIDIRECTIONAL	NA	NA	NA	NA	NA	NA-NA-NA-NA
LIA-099	FLINT	MEDIAL	FLAKE	FLAKE	24.79	13.29	3.95	1.40	NA	100%	ALIGNED_LATERAL	NA	NA	NA	NA	NA	NA-NA-NA-NA
LIA-103	FLINT	COMPLETE	CORE	CORETOOL	22.82	26.14	7.55	5.70	NA	NA	NA	ENDSCRAPER	NA	NA	NA	NA	NA-NA-NA-NA
LIA-105	FLINT	DISTAL	FLAKE	FLAKE	13.77	21.16	5.27	1.60	NA	NA	NA	NA	NA	NA	NA	NA	NA-NA-NA-NA
LIA-120	FLINT	COMPLETE	FLAKE	FLAKE	32.91	12.94	4.10	2.35	PRIMARY_SURFACE-0%	70-90%	ALIGNED	NA	NA	NA	NA	NA	NA-NA-NA-NA
LIA-121	FLINT	COMPLETE	FLAKE	FLAKETOOL	37.10	43.81	9.90	14.90	REMOVED	70-90%	ALIGNED	POSS_USE	NA	NA	NA	NA	NA-NA-NA-NA
LIA-127	FLINT	PROXIMAL	FLAKE	FLAKE	16.34	15.86	3.42	0.75	CRUSHED	NA	NA	NA	NA	NA	NA	NA	NA-NA-NA-NA
LIA-128	FLINT	COMPLETE	FLAKE	FLAKE	17.88	23.23	7.79	4.40	PLAIN-100%	100%	ALIGNED	NA	NA	NA	NA	NA	NA-NA-NA-NA
LIA-129	FLINT	DISTAL	FLAKE	FLAKE	12.25	15.88	4.10	0.75	NA	NA	NA	NA	NA	NA	NA	NA	NA-NA-NA-NA
LIA-132	FLINT	COMPLETE	FLAKE	FLAKE	15.63	24.79	6.03	1.80	PLAIN-NA	100%	LATERAL	NA	NA	NA	NA	NA	NA-NA-NA-NA
LIA-133	FLINT	COMPLETE	NATURAL_PIECE	CORE	31.88	23.35	14.65	7.30	NA	NA	NA	NA	40-60%	1	1	PRIMARY_SURFACE	UNIDIRECTIONAL-NA-NA-NA
LIA-140	FLINT	COMPLETE	FLAKE	SHATTER	17.99	11.58	6.64	1.45	NA	NA	NA	NA	NA	NA	NA	NA	NA-NA-NA-NA
LIA-143	FLINT	COMPLETE	FLAKE	SHATTER	19.71	20.30	6.95	2.75	NA	NA	NA	NA	NA	NA	NA	NA	NA-NA-NA-NA
LIA-146	FLINT	COMPLETE	FLAKE	FLAKE	10.42	15.57	2.52	0.40	PLAIN-NA	100%	ALIGNED	NA	NA	NA	NA	NA	NA-NA-NA-NA
LIA-147	FLINT	SHATTERED	NA	FLAKETOOL	21.14	12.65	2.91	1.00	NA	NA	NA	NA	NA	NA	NA	NA	NA-NA-NA-NA
LIA-150	FLINT	COMPLETE	FLAKE	FLAKE	21.58	10.55	6.96	1.60	PRIMARY_SURFACE-0%	10-30%	ALIGNED	NA	NA	NA	NA	NA	NA-NA-NA-NA
LIA-152	FLINT	COMPLETE	FLAKE	SHATTER	53.79	75.16	12.95	47.40	NA	NA	NA	NA	NA	NA	NA	NA	NA-NA-NA-NA
LIA-154	FLINT	COMPLETE	CORE	CORETOOL	42.16	40.70	24.15	24.55	NA	NA	NA	NOTCH	70-90%	1	5	PLAIN	UNI_LAT-NA-NA-NA
LIA-156	FLINT	COMPLETE	CORE	CORETOOL	23.85	31.05	18.70	14.40	NA	NA	NA	ENDSCRAPER	70-90%	1	1	PLAIN	UNIDIRECTIONAL-NA-NA-NA
LIA-158	FLINT	COMPLETE	NATURAL_PIECE	CORE	22.98	38.87	11.87	1.60	NA	NA	NA	NA	40-60%	1	1	PLAIN	UNIDIRECTIONAL-NA-NA-NA
LIA-159	FLINT	COMPLETE	FLAKE	FLAKE	31.80	36.56	5.33	5.50	PLAIN-NA	0%	NA	NA	NA	NA	NA	NA	NA-NA-NA-NA
LIA-165	FLINT	COMPLETE	FLAKE	SHATTER	32.39	10.72	7.80	2.05	NA	NA	NA	NA	NA	NA	NA	NA	NA-NA-NA-NA
LIA-166	FLINT	COMPLETE	FLAKE	SHATTER	13.95	14.74	3.95	0.80	NA	NA	NA	NA	NA	NA	NA	NA	NA-NA-NA-NA
LIA-190	FLINT	COMPLETE	NATURAL_PIECE	CORE	35.03	27.49	32.14	25.85	NA	NA	NA	NA	70-90%	2	5	COARSE_PREPARED	UNIDIRECTIONAL-UNIDIRECTIONAL-NA-NA
LIA-191	FLINT	COMPLETE	NATURAL_PIECE	CORE	23.27	20.78	13.87	7.20	NA	NA	NA	NA	10-30%	0	3	PRIMARY_SURFACE	NA-NA-NA-NA
LIA-192	FLINT	LONGIT_BROKEN	FLAKE	FLAKE	17.54	13.51	3.60	0.85	NA	NA	NA	NA	NA	NA	NA	NA	NA-NA-NA-NA
LIA-199	FLINT	COMPLETE	FLAKE	FLAKE	8.01	17.97	2.73	0.55	CRUSHED	100%	ALIGNED	NA	NA	NA	NA	NA	NA-NA-NA-NA
LIA-216	FLINT	DISTAL	FLAKE	FLAKE	47.11	30.32	10.07	17.40	NA	NA	NA	NA	NA	NA	NA	NA	NA-NA-NA-NA
LIA-219	FLINT	COMPLETE	FLAKE	FLAKE	25.94	23.10	10.32	5.10	PRIMARY_SURFACE-0%	0%	NA	NA	NA	NA	NA	NA	NA-NA-NA-NA
LIA-220	FLINT	SHATTERED	FLAKE	FLAKE	12.79	14.56	2.99	0.60	NA	NA	NA	NA	NA	NA	NA	NA	NA-NA-NA-NA
LIA-223	FLINT	LONGIT_BROKEN	NATURAL_PIECE	CORE	32.63	13.31	6.72	2.95	NA	NA	NA	NA	NA	NA	NA	NA	NA-NA-NA-NA
LIA-240	FLINT	COMPLETE	FLAKE	FLAKE	35.67	17.76	12.03	7.25	PLAIN-100%	10-30%	LATERAL	NA	NA	NA	NA	NA	NA-NA-NA-NA
LIA-242	FLINT	COMPLETE	FLAKE	FLAKE	11.40	18.04	3.42	0.65	PLAIN-100%	10-30%	OPPOSED	NA	NA	NA	NA	NA	NA-NA-NA-NA
LIA-244	FLINT	COMPLETE	FLAKE	FLAKETOOL	25.46	16.55	4.92	2.45	REMOVED	100%	ALIGNED_LATERAL	DENTICULATE	NA	NA	NA	NA	NA-NA-NA-NA
LIA-248	Quartzite	COMPLETE	COBBLE	CORE	27.68	20.99	17.95	8.75	NA	NA	NA	NA	40-60%	1	2	PLAIN	UNI_LAT-NA-NA-NA
LIA-251	FLINT	COMPLETE	FLAKE	FLAKE	15.62	5.98	3.07	0.35	CRUSHED	10-30%	ALIGNED	NA	NA	NA	NA	NA	NA-NA-NA-NA
LIA-253	FLINT	COMPLETE	FLAKE	FLAKETOOL	23.85	8.71	6.20	1.45	REMOVED	0%	NA	POSS_USE	NA	NA	NA	NA	NA-NA-NA-NA
LIA-263	FLINT	COMPLETE	NATURAL_PIECE	CORE	17.78	11.28	18.36	3.00	NA	NA	NA	NA	40-60%	2	4	PRIMARY_SURFACE	UNIDIRECTIONAL-UNIDIRECTIONAL-NA-NA
LIA-265	FLINT	COMPLETE	FLAKE	FLAKE	19.47	17.66	6.10	2.30	PLAIN-NA	0%	NA	NA	NA	NA	NA	NA	NA-NA-NA-NA
LIA-271	FLINT	MEDIAL	FLAKE	FLAKE	27.70	29.06	8.00	6.75	NA	NA	NA	NA	NA	NA	NA	NA	NA-NA-NA-NA
LIA-279	FLINT	COMPLETE	FLAKE	FLAKE	15.40	12.49	3.69	0.75	PLAIN-NA	10-30%	ALIGNED	NA	NA	NA	NA	NA	NA-NA-NA-NA
LIA-285	FLINT	COMPLETE	FLAKE	FLAKETOOL	30.37	28.65	15.84	15.05	PRIMARY_SURFACE-0%	10-30%	BIDIRECTIONAL	ENDSCRAPER	NA	NA	NA	NA	NA-NA-NA-NA
LIA-286	FLINT	COMPLETE	FLAKE	FLAKE	19.80	16.96	7.44	2.15	PLAIN-100%	100%	BIDIRECTIONAL	NA	NA	NA	NA	NA	NA-NA-NA-NA
LIA-287	FLINT	COMPLETE	FLAKE	FLAKE	16.63	19.84	3.66	1.40	PRIMARY_SURFACE-0%	100%	LATERAL	NA	NA	NA	NA	NA	NA-NA-NA-NA
LIA-290	Quartzite	DISTAL	FLAKE	FLAKE	26.40	30.99	8.79	3.75	NA	NA	NA	NA	NA	NA	NA	NA	NA-NA-NA-NA
LIA-294	FLINT	COMPLETE	NATURAL_PIECE	CORE	12.22	16.40	13.75	2.10	NA	NA	NA	NA	70-90%	3	6	COARSE_PREPARED	UNIDIRECTIONAL-UNIDIRECTIONAL-UNIDIRECTIONAL-NA
LIA-299	FLINT	COMPLETE	NATURAL_PIECE	CORE	35.58	40.57	21.87	22.80	NA	NA	NA	NA	40-60%	2	5	PRIMARY_SURFACE	BIDIRECTIONAL-UNIDIRECTIONAL-NA-NA
LIA-301	FLINT	COMPLETE	FLAKE	FLAKE	18.60	17.99	5.00	1.40	PLAIN-100%	100%	BILATERAL	NA	NA	NA	NA	NA	NA-NA-NA-NA
LIA-303	FLINT	COMPLETE	FLAKE	FLAKETOOL	11.61	19.61	4.58	1.25	REMOVED	100%	BILATERAL	EDGE_RETOUCH	NA	NA	NA	NA	NA-NA-NA-NA
LIA-307	FLINT	COMPLETE	FLAKE	FLAKETOOL	27.60	23.06	16.96	11.70	REMOVED	40-60%	ALIGNED	ENDSCRAPER	NA	NA	NA	NA	NA-NA-NA-NA
LIA-308	FLINT	LONGIT_BROKEN	FLAKE	FLAKE	17.50	8.71	3.87	0.75	NA	NA	NA	NA	NA	NA	NA	NA	NA-NA-NA-NA
LIA-314	FLINT	SHATTERED	FLAKE	SHATTER	21.70	11.10	8.03	1.85	NA	NA	NA	NA	NA	NA	NA	NA	NA-NA-NA-NA
LIA-315	FLINT	COMPLETE	FLAKE	FLAKE	20.16	16.41	5.67	1.65	PLAIN-100%	100%	OPPOSED	NA	NA	NA	NA	NA	NA-NA-NA-NA
LIA-316	FLINT	SHATTERED	CORE	SHATTER	21.36	16.48	10.17	3.75	NA	NA	NA	NA	NA	NA	NA	NA	NA-NA-NA-NA
LIA-317	FLINT	COMPLETE	FLAKE	FLAKE	31.27	19.28	9.13	4.95	PLAIN-100%	100%	ALIGNED	NA	NA	NA	NA	NA	NA-NA-NA-NA
LIA-318	FLINT	COMPLETE	FLAKE	FLAKETOOL	21.55	13.01	7.17	2.20	REMOVED	NA	NA	EDGE_RETOUCH	NA	NA	NA	NA	NA-NA-NA-NA
LIA-321	FLINT	COMPLETE	FLAKE	FLAKE	16.43	23.54	8.48	3.30	SCARS-100%	10-30%	ALIGNED	NA	NA	NA	NA	NA	NA-NA-NA-NA
LIA-322	FLINT	COMPLETE	FLAKE	FLAKE	15.18	19.04	4.12	0.90	CRUSHED	70-90%	ALIGNED	NA	NA	NA	NA	NA	NA-NA-NA-NA
LIA-326	FLINT	COMPLETE	FLAKE	FLAKE	16.00	9.57	3.59	0.50	PLAIN-100%	70-90%	ALIGNED_LATERAL	NA	NA	NA	NA	NA	NA-NA-NA-NA
LIA-329	FLINT	COMPLETE	FLAKE	FLAKE	15.31	17.51	5.30	1.45	PLAIN-NA	NA	NA	NA	NA	NA	NA	NA	NA-NA-NA-NA
LIA-330	FLINT	COMPLETE	FLAKE	FLAKE	16.40	14.86	3.54	0.50	PLAIN-100%	100%	ALIGNED	NA	NA	NA	NA	NA	NA-NA-NA-NA
LIA-331	FLINT	COMPLETE	FLAKE	FLAKE	16.43	22.27	6.25	2.75	PRIMARY_SURFACE-0%	100%	ALIGNED_LATERAL	NA	NA	NA	NA	NA	NA-NA-NA-NA
LIA-332	FLINT	DISTAL	FLAKE	FLAKE	4.92	21.70	4.89	0.60	NA	NA	NA	NA	NA	NA	NA	NA	NA-NA-NA-NA
LIA-335	FLINT	COMPLETE	NATURAL_PIECE	CORE	56.80	114.70	34.80	196.90	NA	NA	NA	NA	70-90%	3	5	PRIMARY_SURFACE	UNIDIRECTIONAL-UNIDIRECTIONAL-UNIDIRECTIONAL-NA
LIA-336	FLINT	COMPLETE	FLAKE	FLAKE	21.76	32.73	13.41	5.50	PRIMARY_SURFACE-0%	NA	NA	NA	NA	NA	NA	NA	NA-NA-NA-NA
LIA-342	FLINT	COMPLETE	FLAKE	FLAKETOOL	41.55	34.59	12.96	16.10	REMOVED	100%	ALIGNED_LATERAL	BACKED_KNIFE	NA	NA	NA	NA	NA-NA-NA-NA
LIA-348	FLINT	DISTAL	FLAKE	FLAKE	36.37	43.31	9.59	14.80	NA	NA	NA	NA	NA	NA	NA	NA	NA-NA-NA-NA
LIA-349	FLINT	COMPLETE	NATURAL_PIECE	CORE	30.85	34.35	33.33	21.90	NA	NA	NA	NA	70-90%	3	3	PRIMARY_SURFACE	UNIDIRECTIONAL-UNIDIRECTIONAL-UNIDIRECTIONAL-NA
LIA-350	FLINT	DISTAL	FLAKE	FLAKETOOL	9.48	20.57	5.75	0.85	NA	NA	NA	ENDSCRAPER	NA	NA	NA	NA	NA-NA-NA-NA
LIA-356	FLINT	COMPLETE	FLAKE	FLAKE	23.20	15.10	6.90	2.25	CRUSHED	70-90%	ALIGNED	NA	NA	NA	NA	NA	NA-NA-NA-NA
LIA-359	FLINT	COMPLETE	FLAKE	FLAKETOOL	33.00	27.00	10.20	8.00	REMOVED	70-90%	ALIGNED	SCRAPER	NA	NA	NA	NA	NA-NA-NA-NA
LIA-360	FLINT	COMPLETE	FLAKE	FLAKE	21.90	12.50	7.60	1.80	PLAIN-NA	0%	NA	NA	NA	NA	NA	NA	NA-NA-NA-NA
LIA-361	FLINT	DISTAL	FLAKE	FLAKE	38.30	19.40	12.00	7.25	NA	NA	NA	NA	NA	NA	NA	NA	NA-NA-NA-NA
LIA-362	FLINT	SHATTERED	FLAKE	SHATTER	16.40	13.90	8.00	1.45	NA	NA	NA	NA	NA	NA	NA	NA	NA-NA-NA-NA
LIA-364	FLINT	SHATTERED	FLAKE	SHATTER	25.30	12.10	7.00	2.85	NA	NA	NA	NA	NA	NA	NA	NA	NA-NA-NA-NA
LIA-367	FLINT	COMPLETE	NATURAL_PIECE	CORE	12.30	16.30	19.90	3.15	NA	NA	NA	NA	10-30%	1	1	PRIMARY_SURFACE	UNIDIRECTIONAL-NA-NA-NA
LIA-368	FLINT	DISTAL	FLAKE	FLAKE	40.70	26.50	29.10	20.70	NA	NA	NA	NA	NA	NA	NA	NA	NA-NA-NA-NA
LIA-370	FLINT	SHATTERED	FLAKE	SHATTER	26.30	13.20	9.50	1.80	NA	NA	NA	NA	NA	NA	NA	NA	NA-NA-NA-NA

Supplementary Table S9. Selected attributes for Lichtenberg II *(continued)*

INVENTARNUMMER	RAWMAT	PRESERVATION	BLANK	CLASSIF	LENGTH	WIDTH	THICK	WEIGHT	PLATFORM	DORSALSCARS	DORSALDIRECT	TOOL_TYPE	AMOUNT_RETCORE	FLAKE_SUR	FLAKE_SCARS	CONDITION_STRIKE	FLAKING_DIR_A_B_C_D
LIA-372	FLINT	COMPLETE	NATURAL_PIECE	CORE	17.50	27.90	16.00	9.90	NA	NA	NA	NA	10-30%	2	3	PLAIN	UNIDIRECTIONAL-BIDIRECTIONAL-NA-NA
LIA-373	FLINT	COMPLETE	NATURAL_PIECE	CORE	25.90	13.60	8.50	2.75	NA	NA	NA	NA	70-90%	2	4	PLAIN	UNIDIRECTIONAL-UNIDIRECTIONAL-NA-NA
LIA-375	FLINT	COMPLETE	FLAKE	CORE	16.40	24.00	13.50	4.75	NA	NA	NA	NA	40-60%	1	2	PLAIN	UNIDIRECTIONAL-NA-NA-NA
LIA-376	FLINT	DISTAL	FLAKE	FLAKE	18.10	6.50	3.60	0.50	NA	NA	NA	NA	NA	NA	NA	NA	NA-NA-NA-NA
LIA-377	FLINT	COMPLETE	FLAKE	FLAKETOOL	31.20	22.50	8.40	6.50	PLAIN-100%	NA	NA	DENTICULATE	NA	NA	NA	NA	NA-NA-NA-NA
LIA-378	FLINT	COMPLETE	NATURAL_PIECE	CORE	23.30	40.10	18.60	15.20	NA	NA	NA	NA	40-60%	2	3	PRIMARY_SURFACE	UNIDIRECTIONAL-UNIDIRECTIONAL-NA-NA
LIA-379	FLINT	COMPLETE	CORE	CORETOOL	40.90	24.40	18.30	12.55	NA	NA	NA	HAMMERSTONE	40-60%	2	4	PRIMARY_SURFACE	UNIDIRECTIONAL-UNIDIRECTIONAL-NA-NA
LIA-380	FLINT	COMPLETE	FLAKE	FLAKE	19.50	15.80	6.60	1.40	PLAIN-100%	70-90%	ALIGNED	NA	NA	NA	NA	NA	NA-NA-NA-NA
LIA-381	FLINT	COMPLETE	FLAKE	FLAKE	20.00	18.60	8.40	1.90	REMOVED	70-90%	LATERAL	NA	NA	NA	NA	NA	NA-NA-NA-NA
LIA-383	FLINT	COMPLETE	FLAKE	FLAKETOOL	17.40	14.30	8.80	1.85	REMOVED	NA	NA	POSS_USE	NA	NA	NA	NA	NA-NA-NA-NA
LIA-384	FLINT	COMPLETE	FLAKE	FLAKE	16.40	16.41	5.00	1.30	CRUSHED	100%	OPPOSED	NA	NA	NA	NA	NA	NA-NA-NA-NA
LIA-387	FLINT	COMPLETE	CORE	CORETOOL	23.10	23.50	14.50	7.50	NA	NA	NA	ENDSCRAPER	40-60%	2	4	PLAIN	BIDIRECTIONAL-UNI_LAT-NA-NA
LIA-388	FLINT	SHATTERED	FLAKE	SHATTER	17.10	8.50	4.80	0.65	NA	NA	NA	NA	NA	NA	NA	NA	NA-NA-NA-NA
LIA-390	FLINT	COMPLETE	NATURAL_PIECE	CORE	21.20	14.90	12.40	4.20	NA	NA	NA	NA	100%	4	5	PLAIN	UNIDIRECTIONAL-UNIDIRECTIONAL-UNIDIRECTIONAL-UNIDIRECTIONAL
LIA-392	FLINT	COMPLETE	FLAKE	FLAKE	8.30	15.80	4.70	0.55	PLAIN-100%	70-90%	ALIGNED	NA	NA	NA	NA	NA	NA-NA-NA-NA
LIA-396	FLINT	DISTAL	FLAKE	FLAKE	15.70	14.40	4.20	0.85	NA	NA	NA	NA	NA	NA	NA	NA	NA-NA-NA-NA
LIA-397	FLINT	COMPLETE	CORE	CORETOOL	23.30	18.70	13.40	5.60	NA	NA	NA	ENDSCRAPER_HAMMER	40-60%	2	2	PLAIN	UNIDIRECTIONAL-UNIDIRECTIONAL-NA-NA
LIA-398	FLINT	COMPLETE	FLAKE	FLAKETOOL	14.30	27.90	16.40	7.45	REMOVED	100%	NA	ENDSCRAPER_SCRAPER	NA	NA	NA	NA	NA-NA-NA-NA
LIA-399	FLINT	COMPLETE	NATURAL_PIECE	CORE	22.40	29.10	18.10	5.55	NA	NA	NA	NA	70-90%	3	7	PLAIN	CONCENTRIC-UNIDIRECTIONAL-BIDIRECTIONAL-NA
LIA-400	FLINT	PROXIMAL	FLAKE	FLAKE	15.60	16.40	3.40	0.70	NA	NA	NA	NA	NA	NA	NA	NA	NA-NA-NA-NA
LIA-401	FLINT	COMPLETE	FLAKE	FLAKE	21.70	8.30	4.70	0.70	PLAIN-100%	0%	NA	NA	NA	NA	NA	NA	NA-NA-NA-NA
LIA-405	FLINT	COMPLETE	FLAKE	FLAKETOOL	21.00	12.40	8.40	2.30	REMOVED	70-90%	NA	ENDSCRAPER	NA	NA	NA	NA	NA-NA-NA-NA
LIA-406	FLINT	COMPLETE	FLAKE	FLAKETOOL	8.10	17.60	3.60	0.55	CRUSHED	NA	NA	EDGE_RETOUCH	NA	NA	NA	NA	NA-NA-NA-NA
LIA-413	FLINT	DISTAL	FLAKE	FLAKETOOL	16.70	20.30	4.80	1.80	NA	NA	NA	SCRAPER	NA	NA	NA	NA	NA-NA-NA-NA
LIA-416	FLINT	COMPLETE	CORE	CORETOOL	26.00	20.70	13.20	5.25	NA	NA	NA	EDGE_RETOUCH	10-30%	1	1	PLAIN	UNIDIRECTIONAL-NA-NA-NA
LIA-419	FLINT	COMPLETE	NATURAL_PIECE	CORE	23.00	13.70	10.60	3.95	NA	NA	NA	NA	10-30%	2	3	PRIMARY_SURFACE	UNIDIRECTIONAL-UNI_LAT-NA-NA
LIA-421	FLINT	COMPLETE	FLAKE	FLAKE	16.60	14.30	4.20	1.00	CRUSHED	0%	NA	NA	NA	NA	NA	NA	NA-NA-NA-NA
LIA-422	FLINT	COMPLETE	NATURAL_PIECE	CORE	15.10	13.40	7.80	1.25	NA	NA	NA	NA	10-30%	1	1	PRIMARY_SURFACE	UNIDIRECTIONAL-NA-NA-NA
LIA-427	FLINT	COMPLETE	FLAKE	FLAKE	17.90	17.30	5.00	1.65	PLAIN-100%	100%	ALIGNED	NA	NA	NA	NA	NA	NA-NA-NA-NA
LIA-428	FLINT	COMPLETE	FLAKE	FLAKETOOL	21.70	11.10	5.50	0.95	CRUSHED	100%	OPPOSED	DENTICULATE	NA	NA	NA	NA	NA-NA-NA-NA
LIA-429	FLINT	COMPLETE	FLAKE	FLAKE	16.50	15.00	4.30	1.05	CRUSHED	10-30%	ALIGNED	NA	NA	NA	NA	NA	NA-NA-NA-NA
LIA-432	FLINT	COMPLETE	FLAKE	FLAKE	11.70	22.90	4.60	1.10	CRUSHED	0%	NA	NA	NA	NA	NA	NA	NA-NA-NA-NA
LIA-433	FLINT	COMPLETE	NATURAL_PIECE	CORE	44.00	33.40	14.90	19.10	NA	NA	NA	NA	40-60%	1	5	PRIMARY_SURFACE	BIDIRECTIONAL-NA-NA-NA
LIA-434	FLINT	PROXIMAL	FLAKE	FLAKE	16.30	17.70	6.30	2.45	NA	NA	NA	NA	NA	NA	NA	NA	NA-NA-NA-NA
LIA-436	FLINT	COMPLETE	FLAKE	FLAKE	31.00	27.90	17.20	12.40	PLAIN-100%	70-90%	ALIGNED	NA	NA	NA	NA	NA	NA-NA-NA-NA
LIA-437	FLINT	SHATTERED	FLAKE	SHATTER	20.60	14.40	8.50	2.50	NA	NA	NA	NA	NA	NA	NA	NA	NA-NA-NA-NA
LIA-439	FLINT	SHATTERED	CORE	SHATTER	15.60	8.70	5.70	0.90	NA	NA	NA	NA	NA	NA	NA	NA	NA-NA-NA-NA
LIA-440	FLINT	COMPLETE	FLAKE	FLAKETOOL	20.70	11.20	7.50	1.30	REMOVED	40-60%	ALIGNED	NOTCH	NA	NA	NA	NA	NA-NA-NA-NA
LIA-441	FLINT	SHATTERED	FLAKE	SHATTER	18.10	14.00	3.00	0.70	NA	NA	NA	NA	NA	NA	NA	NA	NA-NA-NA-NA
LIA-442	FLINT	COMPLETE	FLAKE	FLAKE	15.00	6.60	3.10	0.40	PLAIN-100%	100%	ALIGNED	NA	NA	NA	NA	NA	NA-NA-NA-NA
LIA-446	FLINT	COMPLETE	NATURAL_PIECE	CORE	12.20	18.00	8.80	1.80	NA	NA	NA	NA	10-30%	1	1	PRIMARY_SURFACE	UNIDIRECTIONAL-NA-NA-NA
LIA-447	FLINT	COMPLETE	FLAKE	FLAKE	14.50	19.30	14.00	3.90	PRIMARY_SURFACE-0%	40-60%	BILATERAL	NA	NA	NA	NA	NA	NA-NA-NA-NA
LIA-448	FLINT	SHATTERED	SHATTER	SHATTER	25.00	19.60	12.70	4.80	NA	NA	NA	NA	NA	NA	NA	NA	NA-NA-NA-NA
LIA-449	FLINT	COMPLETE	FLAKE	FLAKE	15.00	7.60	4.50	0.50	PLAIN-100%	100%	ALIGNED_LATERAL	NA	NA	NA	NA	NA	NA-NA-NA-NA
LIA-450	FLINT	MEDIAL	FLAKE	FLAKE	18.30	16.50	3.20	1.55	NA	NA	NA	NA	NA	NA	NA	NA	NA-NA-NA-NA
LIA-451	FLINT	COMPLETE	NATURAL_PIECE	CORE	25.40	21.00	30.00	105.00	NA	NA	NA	NA	10-30%	1	1	PRIMARY_SURFACE	UNIDIRECTIONAL-NA-NA-NA
LIA-453	FLINT	MEDIAL	FLAKE	FLAKE	15.20	15.70	2.80	0.75	NA	NA	NA	NA	NA	NA	NA	NA	NA-NA-NA-NA
LIA-454	FLINT	COMPLETE	FLAKE	FLAKE	17.10	6.30	4.10	0.45	PLAIN-NA	40-60%	LATERAL	NA	NA	NA	NA	NA	NA-NA-NA-NA
LIA-455	FLINT	COMPLETE	FLAKE	FLAKE	15.40	17.80	4.10	1.35	CRUSHED	70-90%	ALIGNED	NA	NA	NA	NA	NA	NA-NA-NA-NA
LIA-456	FLINT	DISTAL	FLAKE	FLAKE	15.00	10.90	4.40	0.90	NA	NA	NA	NA	NA	NA	NA	NA	NA-NA-NA-NA
LIA-457	FLINT	COMPLETE	SHATTER	CORETOOL	18.30	12.20	8.50	2.15	NA	NA	NA	NOTCH	NA	NA	NA	NA	NA-NA-NA-NA
LIA-458	FLINT	COMPLETE	FLAKE	FLAKETOOL	17.30	19.90	7.20	2.20	REMOVED	10-30%	LATERAL	POSS_USE	NA	NA	NA	NA	NA-NA-NA-NA
LIA-461	FLINT	COMPLETE	FLAKE	FLAKETOOL	22.20	24.30	13.20	6.90	REMOVED	70-90%	CONCENTRIC	POSS_USE	NA	NA	NA	NA	NA-NA-NA-NA
LIA-462	FLINT	COMPLETE	NATURAL_PIECE	CORE	16.80	37.20	17.20	11.50	NA	NA	NA	NA	10-30%	1	1	PRIMARY_SURFACE	UNIDIRECTIONAL-NA-NA-NA
LIA-463	FLINT	COMPLETE	NATURAL_PIECE	CORETOOL	28.80	24.10	6.30	6.00	NA	NA	NA	NOTCH	NA	NA	NA	NA	NA-NA-NA-NA
LIA-464	FLINT	COMPLETE	FLAKE	FLAKETOOL	15.90	23.90	11.40	4.40	REMOVED	100%	ALIGNED_LATERAL	POSS_USE	NA	NA	NA	NA	NA-NA-NA-NA
LIA-465	FLINT	FROSTCRACK	FLAKE	FLAKE	22.40	17.40	9.50	3.20	NA	NA	NA	NA	NA	NA	NA	NA	NA-NA-NA-NA
LIA-467	FLINT	COMPLETE	FLAKE	FLAKETOOL	18.70	16.10	8.50	2.80	PRIMARY_SURFACE-0%	10-30%	LATERAL	NOTCH	NA	NA	NA	NA	NA-NA-NA-NA
LIA-468	Quartzite(?)	COMPLETE	COBBLE	OTHER	34.00	25.10	26.50	26.60	NA	NA	NA	HAMMERSTONE	NA	NA	NA	NA	NA-NA-NA-NA
LIA-469	FLINT	COMPLETE	FLAKE	FLAKETOOL	20.70	11.60	6.80	1.15	NA	70-90%	BILATERAL	POSS_USE	NA	NA	NA	NA	NA-NA-NA-NA
LIA-470	FLINT	COMPLETE	CORE	CORETOOL	27.20	31.50	20.90	12.25	NA	NA	NA	NOTCH	10-30%	1	1	PRIMARY_SURFACE	UNIDIRECTIONAL-NA-NA-NA
LIA-471	FLINT	COMPLETE	NATURAL_PIECE	CORE	15.20	13.70	7.70	1.35	NA	NA	NA	NA	40-60%	1	1	PRIMARY_SURFACE	UNIDIRECTIONAL-NA-NA-NA
LIA-472	FLINT	DISTAL	FLAKE	FLAKE	15.80	9.90	3.20	0.55	NA	NA	NA	NA	NA	NA	NA	NA	NA-NA-NA-NA
LIA-473	FLINT	COMPLETE	CORE	CORETOOL	24.80	19.00	14.50	5.40	NA	NA	NA	NOTCH	70-90%	3	4	PLAIN	UNIDIRECTIONAL-UNIDIRECTIONAL-UNIDIRECTIONAL-NA
LIA-474	FLINT	COMPLETE	FLAKE	FLAKE	20.00	17.20	6.80	2.70	PRIMARY_SURFACE-0%	70-90%	ALIGNED	NA	NA	NA	NA	NA	NA-NA-NA-NA
LIA-475	FLINT	COMPLETE	FLAKE	FLAKETOOL	15.70	21.70	5.90	1.80	NA	100%	LATERAL	EDGE_RETOUCH	NA	NA	NA	NA	NA-NA-NA-NA
LIA-476	FLINT	MEDIAL	FLAKE	FLAKE	15.30	14.50	3.10	1.00	NA	NA	NA	NA	NA	NA	NA	NA	NA-NA-NA-NA
LIA-478	FLINT	COMPLETE	SHATTER	CORETOOL	22.40	13.70	12.00	3.15	NA	NA	NA	NOTCH	NA	NA	NA	NA	NA-NA-NA-NA
LIA-479	FLINT	COMPLETE	FLAKE	FLAKETOOL	17.80	13.80	5.00	1.40	REMOVED	100%	LATERAL	EDGE_RETOUCH	NA	NA	NA	NA	NA-NA-NA-NA
LIA-481	FLINT	COMPLETE	FLAKE	FLAKE	20.30	8.70	5.40	1.40	CRUSHED	40-60%	ALIGNED	NA	NA	NA	NA	NA	NA-NA-NA-NA
LIA-482	FLINT	COMPLETE	CORE	CORETOOL	20.90	18.50	8.00	2.75	NA	NA	NA	POSS_USE	40-60%	1	4	PLAIN	CONCENTRIC-NA-NA-NA
LIA-483	FLINT	LIGHTLY_DAMAGED	FLAKE	FLAKETOOL	15.20	19.50	4.90	0.85	REMOVED	NA	NA	NOTCH	NA	NA	NA	NA	NA-NA-NA-NA
LIA-487	FLINT	SHATTERED	FLAKE	SHATTER	15.00	8.70	6.50	0.65	NA	NA	NA	NA	NA	NA	NA	NA	NA-NA-NA-NA
LIA-489	FLINT	COMPLETE	NATURAL_PIECE	CORE	30.20	32.80	28.50	20.40	NA	NA	NA	NA	40-60%	3	4	PLAIN	UNIDIRECTIONAL-UNIDIRECTIONAL-UNIDIRECTIONAL-NA
LIA-491	FLINT	SHATTERED	CORE	SHATTER	31.10	29.40	12.40	9.90	NA	NA	NA	NA	NA	NA	NA	NA	NA-NA-NA-NA
LIA-495	FLINT	COMPLETE	COBBLE	MANUPORT	77.90	68.30	35.00	212.75	NA	NA	NA	NA	NA	NA	NA	NA	NA-NA-NA-NA
LIA-498	FLINT	COMPLETE	FLAKE	FLAKE	11.30	15.40	7.40	1.35	PLAIN-100%	70-90%	ALIGNED	NA	NA	NA	NA	NA	NA-NA-NA-NA
LIA-499	FLINT	SHATTERED	FLAKE	SHATTER	23.80	9.80	5.80	1.10	NA	NA	NA	NA	NA	NA	NA	NA	NA-NA-NA-NA
LIA-500	FLINT	COMPLETE	NATURAL_PIECE	CORE	10.80	17.10	15.00	2.45	NA	NA	NA	NA	10-30%	1	1	PRIMARY_SURFACE	UNIDIRECTIONAL-NA-NA-NA

Supplementary Table S9. Selected attributes for Lichtenberg II *(continued)*

INVENTARNUMMER	RAWMAT	PRESERVATION	BLANK	CLASSIF	LENGTH	WIDTH	THICK	WEIGHT	PLATFORM	DORSALSCARS	DORSALDIRECT	TOOL_TYPE	AMOUNT_RETCORE	FLAKE_SUR	FLAKE_SCARS	CONDITION_STRIKE	FLAKING_DIR_A_B_C_D
LIA-503	FLINT	SHATTERED	CORE	SHATTER	16.40	9.60	8.40	0.70	NA	NA	NA	NA	NA	NA	NA	NA	NA-NA-NA-NA
LIA-504	Quartzite	COMPLETE	FLAKE	FLAKETOOL	75.00	41.50	11.60	41.00	PRIMARY_SURFACE-0%	0%	NA	NOTCH	NA	NA	NA	NA	NA-NA-NA-NA
LIA-505	FLINT	DISTAL	FLAKE	FLAKE	31.90	23.70	8.30	5.90	NA	NA	NA	NA	NA	NA	NA	NA	NA-NA-NA-NA
LIA-506	FLINT	DISTAL	FLAKE	FLAKE	20.70	32.20	6.10	3.70	NA	NA	NA	NA	NA	NA	NA	NA	NA-NA-NA-NA
LIA-510	FLINT	COMPLETE	CORE	CORETOOL	42.80	33.10	33.20	52.60	NA	NA	NA	HAMMERSTONE	10-30%	2	4	NA	BIDIRECTIONAL-UNIDIRECTIONAL-NA-NA
LIA-511	FLINT	SHATTERED	FLAKE	SHATTER	22.60	10.60	5.20	1.10	NA	NA	NA	NA	NA	NA	NA	NA	NA-NA-NA-NA
LIA-513	Quartzite	COMPLETE	FLAKE	FLAKE	53.70	106.30	25.00	94.60	PRIMARY_SURFACE-0%	40-60%	LATERAL	NA	NA	NA	NA	NA	NA-NA-NA-NA
LIA-514	IronConc	COMPLETE	COBBLE	MANUPORT	80.20	54.80	41.00	255.40	NA	NA	NA	NA	NA	NA	NA	NA	NA-NA-NA-NA
LIA-515	FLINT	COMPLETE	SHATTER	CORETOOL	13.50	15.30	6.90	1.25	NA	NA	NA	ENDSCRAPER	NA	NA	NA	NA	NA-NA-NA-NA
LIA-516	FLINT	PROXIMAL	FLAKE	FLAKE	17.70	22.10	7.10	3.45	NA	NA	NA	NA	NA	NA	NA	NA	NA-NA-NA-NA
LIA-517	FLINT	COMPLETE	FLAKE	FLAKE	29.20	13.60	8.80	2.55	PLAIN-100%	100%	LATERAL	NA	NA	NA	NA	NA	NA-NA-NA-NA
LIA-518	FLINT	COMPLETE	NATURAL_PIECE	CORE	47.60	63.40	60.10	171.30	NA	NA	NA	NA	10-30%	1	1	PRIMARY_SURFACE	UNIDIRECTIONAL-NA-NA-NA
LIA-521	FLINT	COMPLETE	FLAKE	FLAKE	18.00	12.70	22.10	4.80	PRIMARY_SURFACE-0%	0%	NA	NA	NA	NA	NA	NA	NA-NA-NA-NA
LIA-522	FLINT	COMPLETE	NATURAL_PIECE	CORE	24.90	12.00	12.40	4.45	NA	NA	NA	NA	100%	2	5	PLAIN	UNIDIRECTIONAL-UNIDIRECTIONAL-NA-NA
LIA-524	FLINT	COMPLETE	FLAKE	FLAKE	34.00	33.10	9.50	6.45	PLAIN-NA	100%	ALIGNED_LATERAL	NA	NA	NA	NA	NA	NA-NA-NA-NA
LIA-526	FLINT	COMPLETE	NATURAL_PIECE	CORE	13.60	27.40	34.40	19.15	NA	NA	NA	NA	10-30%	1	1	PRIMARY_SURFACE	UNIDIRECTIONAL-NA-NA-NA
LIA-527	FLINT	PROXIMAL	FLAKE	FLAKE	10.40	18.00	4.50	1.20	NA	NA	NA	NA	NA	NA	NA	NA	NA-NA-NA-NA
LIA-528	FLINT	COMPLETE	FLAKE	FLAKE	16.10	12.70	2.60	0.30	PLAIN-NA	100%	ALIGNED	NA	NA	NA	NA	NA	NA-NA-NA-NA
LIA-529	FLINT	SHATTERED	CORE	SHATTER	16.00	12.00	7.40	1.15	NA	NA	NA	NA	NA	NA	NA	NA	NA-NA-NA-NA
LIA-532	FLINT	COMPLETE	SHATTER	CORETOOL	63.00	31.00	22.80	34.40	NA	NA	NA	NOTCH	NA	NA	NA	NA	NA-NA-NA-NA
LIA-536	FLINT	COMPLETE	FLAKE	FLAKETOOL	14.90	26.00	11.80	3.55	PRIMARY_SURFACE-0%	NA	NA	EDGE_RETOUCH	NA	NA	NA	NA	NA-NA-NA-NA
LIA-537	FLINT	COMPLETE	FLAKE	FLAKE	16.60	19.20	5.70	1.95	PRIMARY_SURFACE-0%	40-60%	ALIGNED_LATERAL	NA	NA	NA	NA	NA	NA-NA-NA-NA
LIA-538	FLINT	COMPLETE	CORE	CORETOOL	21.90	14.80	13.00	3.20	NA	NA	NA	NATBACK	40-60%	2	3	PLAIN	UNIDIRECTIONAL-BIDIRECTIONAL-NA-NA
LIA-541	FLINT	COMPLETE	FLAKE	FLAKE	11.50	21.50	7.00	1.65	PRIMARY_SURFACE-0%	10-30%	LATERAL	NA	NA	NA	NA	NA	NA-NA-NA-NA
LIA-543	Quartzite	SHATTERED	SHATTER	SHATTER	20.30	12.00	7.70	1.55	NA	NA	NA	NA	NA	NA	NA	NA	NA-NA-NA-NA
LIA-545	FLINT	SHATTERED	FLAKE	SHATTER	29.60	26.00	6.60	4.00	NA	NA	NA	NA	NA	NA	NA	NA	NA-NA-NA-NA
LIA-548	FLINT	COMPLETE	FLAKE	FLAKE	12.80	15.80	3.50	0.80	CRUSHED	10-30%	LATERAL	NA	NA	NA	NA	NA	NA-NA-NA-NA
LIA-549	FLINT	SHATTERED	SHATTER	SHATTER	16.80	8.00	7.20	0.55	NA	NA	NA	NA	NA	NA	NA	NA	NA-NA-NA-NA
LIA-550	FLINT	COMPLETE	FLAKE	FLAKETOOL	50.60	27.70	9.70	11.65	CRUSHED	10-30%	ALIGNED	POSS_USE	NA	NA	NA	NA	NA-NA-NA-NA
LIA-554	FLINT	SHATTERED	CORE	SHATTER	17.80	10.90	7.80	1.10	NA	NA	NA	NA	NA	NA	NA	NA	NA-NA-NA-NA
LIA-556	Porphyry	COMPLETE	COBBLE	MANUPORT	55.00	51.60	42.50	167.85	NA	NA	NA	NA	NA	NA	NA	NA	NA-NA-NA-NA
LIA-557	FLINT	COMPLETE	FLAKE	FLAKETOOL	12.70	24.40	7.00	2.15	REMOVED	0%	NA	EDGE_RETOUCH	NA	NA	NA	NA	NA-NA-NA-NA
LIA-558	FLINT	DISTAL	FLAKE	FLAKE	16.50	8.30	2.60	0.50	NA	NA	NA	NA	NA	NA	NA	NA	NA-NA-NA-NA
LIA-559	FLINT	COMPLETE	NATURAL_PIECE	CORETOOL	36.40	26.80	19.20	16.70	NA	NA	NA	HAMMERSTONE	NA	NA	NA	NA	NA-NA-NA-NA

References

Bratlund, B., 1999. Taubach revisited. Jahrbuch des Römisch-Germanischen Zentralmuseums 46, 61–114.

Gaudzinski-Windheuser, S., Roebroeks, W., 2014. Multidisciplinary studies or the Middle Paleolithic record from Neumark-Nord (Germany). Volume I, Veröffentlichungen des landesamtes für archäologie sachsen-anhalt 69. Beier & Beran, Halle(Saale).

Hein, M., Weiss, M., Otcherednoy, A., Lauer, T., 2020. Luminescence chronology of the key-Middle Paleolithic site Khotylevo I (Western Russia) - Implications for the timing of occupation, site formation and landscape evolution. Quaternary Science Advances 2, 100008. https://doi.org/10.1016/j.qsa.2020.100008

Mania, D., Toepfer, V., 1973. Königsaue: Gliederung, Ökologie und mittelpaläolithische Funde der letzten Eiszeit. Veröffentlichungen des Landesmuseums für Vorgeschichte in Halle 26, Deutscher Verlag der Wissenschaften, Berlin.

Pastoors, A., 2001. Die Mittelpaläolithische Freilandstation von Salzgitter-Lebenstedt: Genese der Fundstelle und Systematik der Steinbearbeitung. Archiv der Stadt Salzgitter, Salzgitter.

Tode, A., 1982. Der altsteinzeitliche Fundplatz Salzgitter-Lebenstedt. Teil I, archäologischer Teil. Böhlau, Köln, Wien.

Toepfer, V., 1958. Steingeräte und Palökologie der mittel- paläolithischen Fundstelle Rabutz bei Halle. Jahresschrift für mitteldeutsche Vorgeschichte 41/42, 140–179.

Veil, S., Breest, K., Höfle, H.-C., Meyer, H.-H., Plisson, H., Urban-Küttel, B., Wagner, G.A., Zöller, L., 1994. Ein mittelpaläolithischer Fundplatz aus der Weichsel-Kaltzeit bei Lichtenberg, Lkr. Lüchow-Dannenberg. Germania 72, 1–66.

Weiss, M., 2020. The Lichtenberg Keilmesser - it's all about the angle. PLOS ONE 15, e0239718. https://doi.org/10.1371/journal.pone.0239718

Weiss, M., 2015. Stone tool analysis and context of a new late Middle Paleolithic site in western central Europe - Pouch-Terrassenpfeiler, Ldkr. Anhalt-Bitterfeld, Germany. Quartaer 62, 23–62. https://doi.org/10.7485/QU62_2

Weiss, M., Otcherednoy, A., Wiśniewski, A., 2017. Using multivariate techniques to assess the effects of raw material, flaking behavior and tool manufacture on assemblage variability: An example from the late Middle Paleolithic of the European Plain. Journal of Archaeological Science 87, 73–94. https://doi.org/10.1016/j.jas.2017.09.014

Weiss, M., Weber, T., 2019. Das Mittelpaläolithikum in Mitteldeutschland – Auswertung und Interpretation von Abschlaginventaren anhand multivariater Analysemethoden, in: Baales, M., Pasda, C. (Eds.), All Der Holden Hügel Ist Keiner Mir Fremd - Festschrift Zum 65. Geburtstag von Claus-Joachim Kind, Universitätsforschungen Zur Prähistorischen Archäologie [Upa]. Habelt, Bonn.

Wiśniewski, A., Adamiec, G., Badura, J., Bluszcz, A., Kowalska, A., Kufel-Diakowska, B., Mikolajczyk, A., Murczkiewicz, M., Musil, R., Przybylski, B., Skrzypek, G., Stefaniak, K., Zych, J., 2013. Occupation dynamics north of the Carpathians and Sudetes during the Weichselian (MIS5d-3): The Lower Silesia (SW Poland) case study. Quaternary International 294, 20–40. https://doi.org/10.1016/j.quaint.2011.09.016

Section 4: Lichtenberg I and II Traceology

In order to provide additional data on the nature of the human occupation at the Middle Paleolithic site of Lichtenberg I and II, traceological analysis were conducted on a sample of 27 artefacts. The traceological method (Semenov, 1964) aims at identifying specific taphonomical, technological and functional traces or modifications, which allows us to reconstruct specific technical behaviours, the post-depositional history of anthropic inclusions within sedimentary units as well as how and to what end stone tools where made and used at a specific site. This is achieved by systematically scanning the edges and surfaces of stone tools under different magnifications ranging between 0.63 X to 500x and plotting their location and distribution. The location and morphology of specific micro negatives, edge rounding, microscopic polish, micro scars and striations are compared to an experimental reference collection in order to establish the kinetics of stone tool use as well as the material transformed (Chan et al., 2020; González-Urquijo and Ibañez-Estéves, 1994; Keeley, 1980; Vaughan, 1985). For this study a Carl Zeiss Stemi 508 stereo microscope and an Olympus reflected light microscope have been used.

The majority of the analyzed artefacts have been made on flint and show a light developed soil polish, which presents itself as an ephemeral bright sheen that covers the entire surface of the artefacts and impends the secure identification of the materials transformed. Out of the 27 lithics eight have suffered less from taphonomic processes making the identification of both motion and material transformed possible, while on six only the motion and location of working edges could be detected (Table S10). Artefacts from Lichtenberg I and II have been analyzed. The Lichtenberg I sample was composed of one Keilmesser, two flakes and one fragmented tool with bifacial shaping. Due to taphonomical constraints, the tool fragment and the flakes presented no discernible traces of use. The Keilmesser, on the other hand, presented traces resulting from longitudinal (cutting) motions. The Lichtenberg II tools were used with different modalities of force, including pressure and percussion. Tools used with the application of pressure have been wielded in longitudinal, transverse and drilling motions (Figure S42).

Table S10. Summary of the traceological analysis. Li-6, Li-7, LIA-36, and LIA-50 are from Lichtenberg I, the other artefacts come belong to Lichtenberg II.

#	Blank	Use	Force	Motion	Striations	Working Edges	Material Worked
Li-6	Fractured bifacial tool	No	-	-	-	1	-
Li-7	Keilmesser	Yes	Pressure	Longitudinal	Y	1	Soft Organic
LIA-36	BTF	No	-	-	-	-	-
LIA-50	Flake	No	-	-	-	-	-
LIA-99	Flake,	No	-	-	-	-	-
LIA-103	Flake/Spal	Probably,	Pressure/ Percussive	Drilling	-	2	Hard Organic
LIA-120	Flake	No	-	-	-	-	-
LIA-121	Flake	Yes	Pressure/ Percussive	Transverse/ Longitudinal	Y	2	Hard Organic
LIA-128	Flake	Probably,	Pressure/ Percussive	Transverse	No	1	-
LIA-133	Ckunk	Yes	Pressure	Drilling	No	1	Hard Organic
LIA-147	Flake	No	-	-	-	1	-
LIA-152	Flake/Spal	?	Pressure	-	-	1	-
LIA-154	Core/Chunk	Yes	Pressure	Transverse	Y	1	Hard Organic
LIA-216	Flake/Spall	Yes	Pressure	Longitudinal / Transverse	Y	2	Soft Organic/ Hard Organic
LIA-285	Chunk	Probably	Percussive	-	-	1	-
LIA-307	Flake	Yes	Pressure	Transverse	Y	1	Hard Organic/W ood
LIA-327	Flake	No	-	-	-	1	-
LIA-330	Flake	No	-	-	-	-	-
LIA-342	Flake	Probably	Pressure/ Percussive	Longitudinal / Transverse	-	2	-
LIA-359	Flake	Yes	Pressure	Transverse	Y	1	Soft Vegetal/ Hard Organic

LIA-377	Core/Chunk	No	Percussive	-	-	-	-
LIA-379	Chunk	?	Percussive	-	-	-	-
LIA-398	Flake/Spal	Probably,	Pressure	Transverse	-	1	Hard Organic
LIA-478	Chunk	No	-	-	-	-	-
LIA-504	Flake/Spall	No	-	-	-	1	-
LIA-538	Flake/Spal	Probably	Pressure	Transverse	-	1	-
LIA-550	Flake	Yes	Pressure	Transverse	Y	2	Soft Vegetal / Hard Organic

Artefact LIA-550 (Figure S43), a flake made on dark translucent flint, shows two working edges, one on the distal termination, which ends on a hinge fracture, and one on the lateral edge of the tool; both have been used in transverse motions. The traces located on the distal working edge show a well-developed bright undulating polish with a high incidence of directional markers indicating a crossed transverse motion. This bright well-developed polish likely formed from the contact with a highly abrasive and soft vegetal material while the striations may be related to the admixture of mineral particles, possibly sand or grit during the scraping activity. The working edge was re-sharpened leaving only a small part of the original traces preserved.

Artefact LIA-307 shows a small concave truncation placed on the distal portion of a dark translucent thick flake, which was intentionally thinned along the proximal ventral surface (Figure S44). The working edge shows intense rounding from use indicative for the processing of a hard organic material. Well-developed bright polish on both extremities of the working edge, associated with the rounding may indicate the working of wood. The edges of the negatives on the dorsal surface of the tool shows signs of crushing while “G” type polish (Moss, 1987; Rots, 2010) spots on the ventral surface may indicate that the artefacts was hafted.

The processing of soft animal material has been attested at artefact LIA-216, which is an elongated flake with parallel sides that shows two working edges, one on the acute lateral edge and one on the steeper distal portion (Figure S45). Along the edge a patterned distribution of micro negatives on both dorsal and ventral faces, coupled with micro stria indicate a longitudinal and transverse motions. Light developed undulating mate micro polish and circular micro pits indicate a soft, but abrasive organic material; in combination with punctuated bright flat polish areas, which hint at the repeated contact with a harder material may indicate a possible use of this tool as a meat knife or butchering tool.

Artefact LIA-359 shows a concave working edge with a steep cortical back. The high incidence of micro negatives with step fracture and hinge fracture terminations in combination with the punctuated crushed appearance of the working edge may be a result of combination of both the application of pressure and percussive motions during use activities. Different traces including bright undulating micro polish observed on the distal portion of the dorsal working edge, flat bright spots and scars as well as an extensive bright flat micro polish surface with striations on the ventral surface have been observed (Figure S46). The processing of both hard, possibly wood, and soft abrasive vegetable material is suggested for this tool.

The analyzed Keilmesser (LI-7) presents a symmetrical outline and well-defined techno functional elements including a working edge, a transformative part and a prehensile/hafting zone. The continuous and symmetric convex working surface shows signs of repeated re-sharpening on the dorsal face, evident by the continuous retouch, which is absent on the ventral surface save for a series of larger negatives on the distal end of the working edge. A considerable amount of effort was placed in thinning the prehensile/hafting zone or back of the tool. The tool is made on dark Baltic flint and shows little signs of severe post-depositional modification, i.e. mechanical damage or chemical weathering furthering the preservation of wear traces. Traces indicating the natures of the transformed material, however, are subtle being constricted to lightly developed micro polishes zones located on the distal portion of the working edge (Figure S47 F1). Negative edge rounding and additional polished surfaces are found further inwards on the dorsal side of the working edge. Directional markers, including striations running parallel to the working edge of the tool and generally associated with lightly developed polished spots are also located on the dorsal surfaces of the working edge. In combination with the micro negatives located on the ventral side of the tool a longitudinal cutting motion under the excretion of pressure is suggested for the tool comparable with the interpretation offered by previous traceological analysis from Lichtenberg (Veil et al., 1994).The light developed polish and the presence of striations on the analyzed specimen indicates the processing of a soft organic material and occasional contact with harder organic substance; a use as butchering knife is therefore suggested.

The back of the analyzed Keilmesser shows a series of marked modifications and traces associated with intense mechanical stress. The distal portion of the back shows marked rounding and crouching evident by short continuous micro-negatives with step and hinge terminations (Figure S48 F1 and F2). Bright and semi undulating cohesive polished areas have been identified on the edges of the negatives located on the medial portion of the back indicating the repeated contact with a hard organic substance. Together these signs may indicate the continued mechanical friction of the tool with a hard organic haft, thus possibly indicating the use of composite tools by Neanderthals at the site. Which is not to say that Keilmesser tools in general were hafted, a sample of one hardly establishes a pattern making it paramount to conduct further investigations into the subject.

In summary the preliminary traceological analysis of the Lichtenberg II lithic material indicates a heterogeneous pattern of activities including the processing of soft animal materials, soft and abrasive vegetable materials and hard vegetable materials (wood). The combination of percussive and pressure force has been noted as well as the possible use of hafting technology. The later has been observed on artefact LIA-307 based on the presence of G type polish and the scaring on the dorsal surface along the edges of the central negatives. The diminutive characteristics of the assemblage in general, the high incidence of crushing coupled with the high amount of force used during the different productive activities undertaken at the site may suggested that artefacts LIA-307 was not the only hafted tool. The absence of further hafting wear, however, constrains the further exploration of this possibility. In respect to the traceological analysis of the sample from the Keilmesser horizon from Lichtenberg I, a use of the analyzed specimen as a hafted butchering knife is suggested due to the wear traces identified. It cannot be stressed enough, however, that additional specimens need to be analyzed in order to fully understand the function of the Neanderthal occupation in order to add information to the already existing traceological investigation (Veil et al., 1994). While the analyzed lithic assemblage from Lichtenberg II is yet too small to properly address site function the preliminary analysis supports the interpretation of the site as being more than a raw material extraction and tool production station and likely the accumulation of the lithics reflects a diversified spectrum of tasks and productive activities undertaken by of Neanderthals at a lakeshore environment.

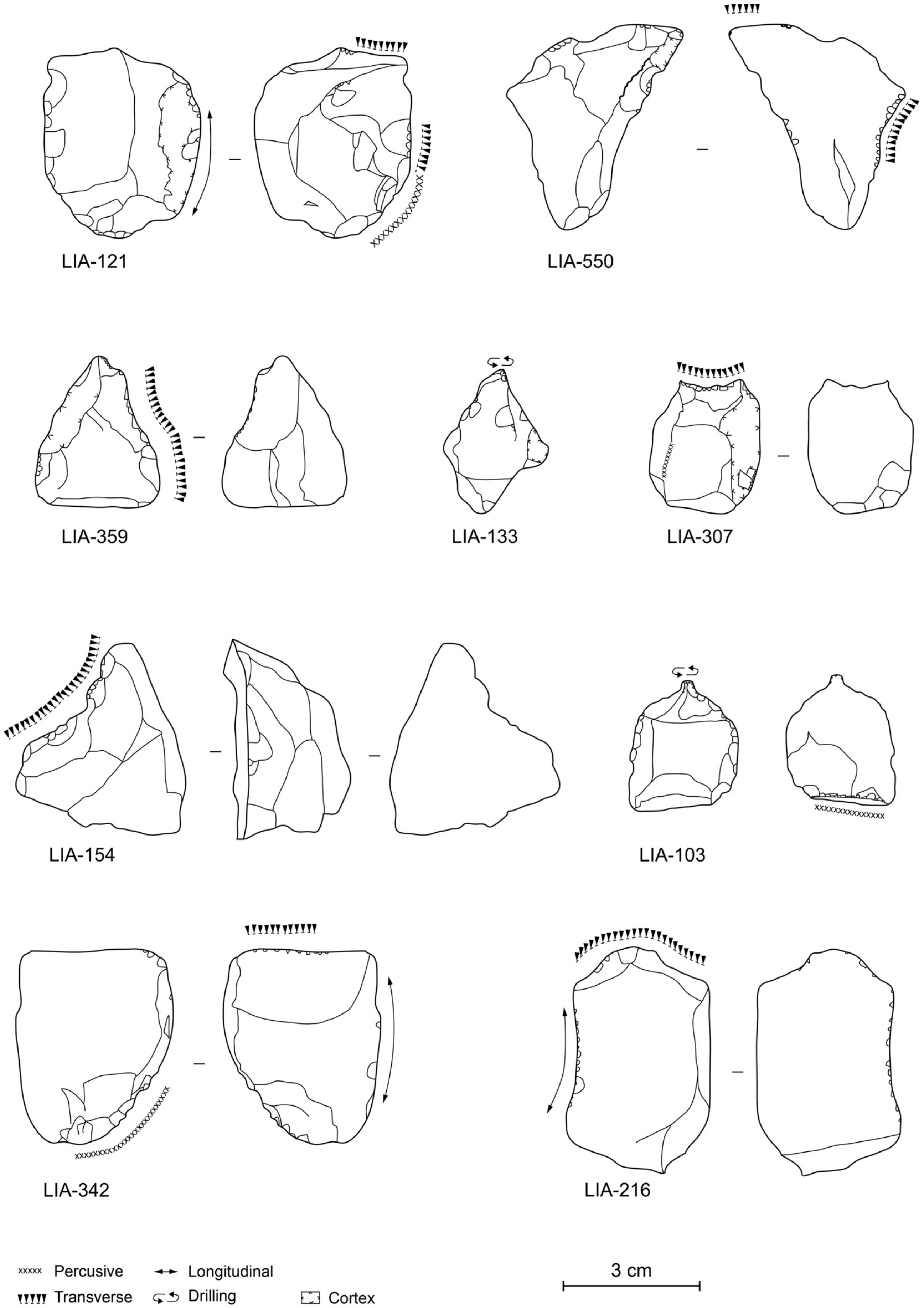

Figure S42. Schematic drawings of the tools with definite and probable use traces showing the location of working edges, the type of force used and use motions.

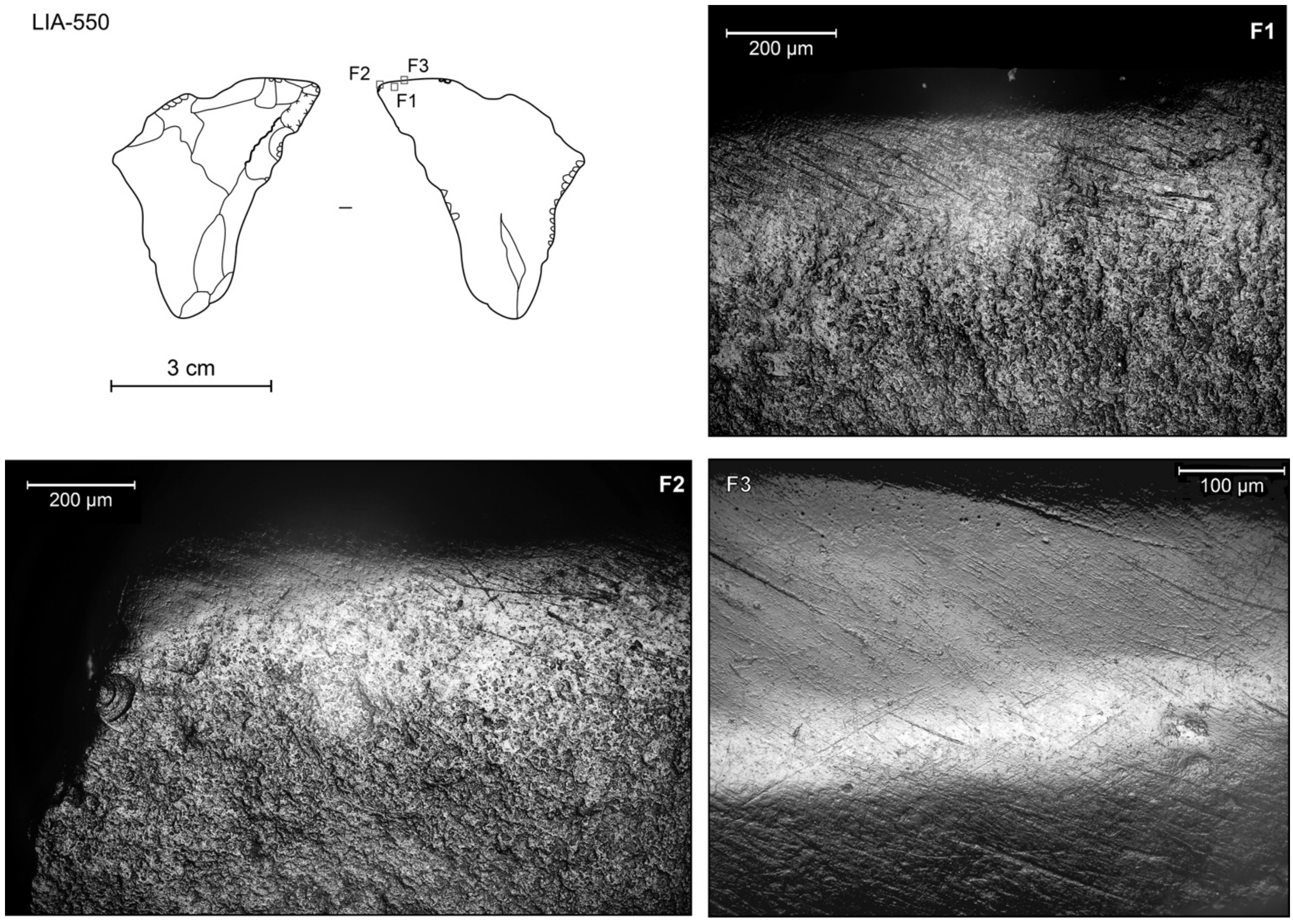

Figure S43. Schema of artefact LIA-550 and the location of the micrographs showing the use related polish. F1 – taken at magnification 100 x bright undulating extensive polish located on the distal portion of the working edge; F2 – taken at magnification 100x on the edge of the working surface showing the spread of the bright undulating extensive polish, note the high incidence of striations and scratches; F3 – taken at magnification 200x at the center of the maximum extension of the micro polished surface on the working edge of the tool. The spread and connectedness of the polish is very high and the surface is extremely smoothened, again the criss-cross patterned motion of tool use is particularly evident by the striations and scratches. The resemblance to cereal polish (Clemente and Gibaja, 1998) is remarkable.

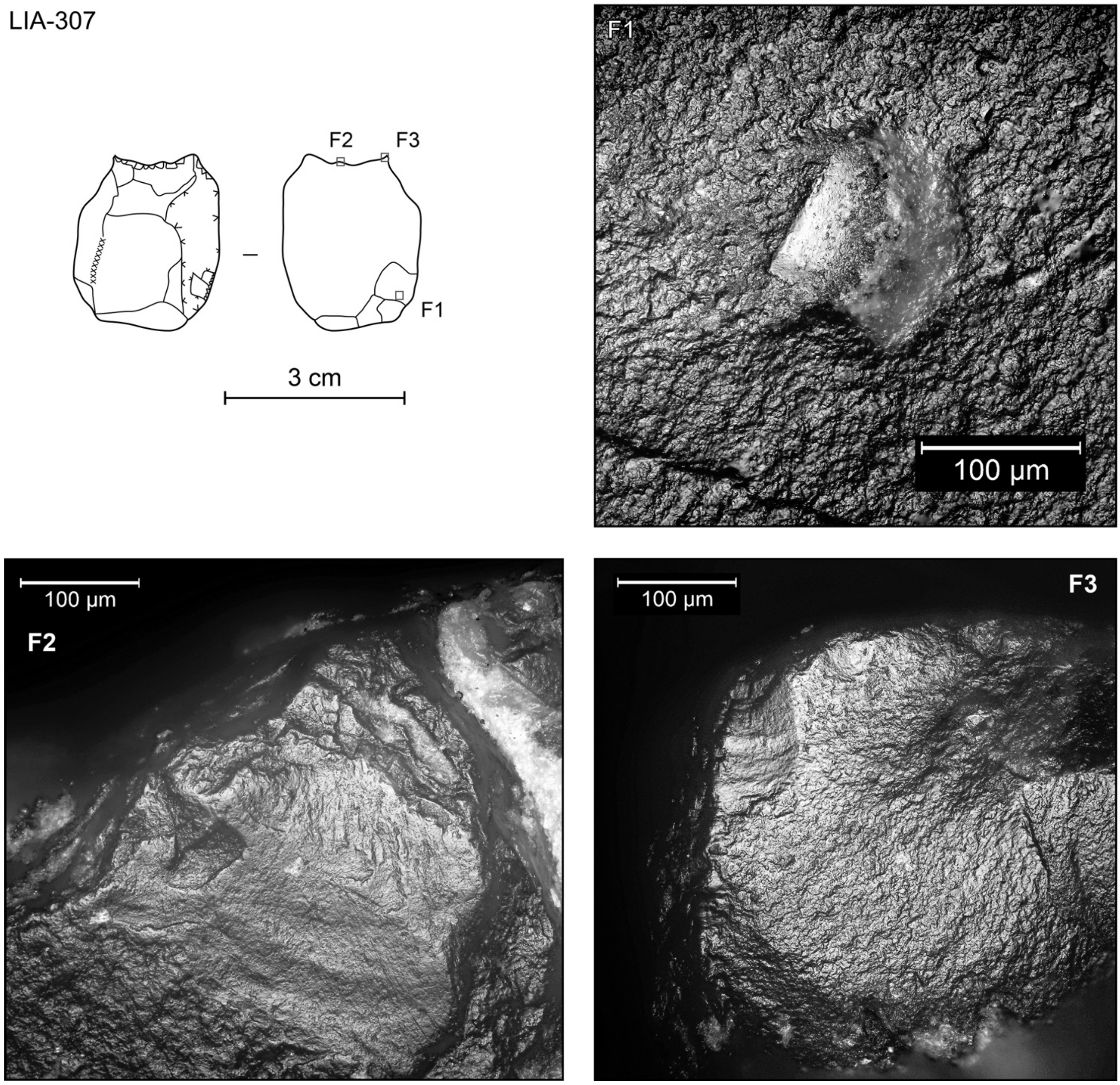

Figure S44. Schema of artefact LIA-307 and the location of the micrographs showing use and hafting related polish. F1 – flat bright polish located on the eminence of the micro topography on the ventral surface of the tool; F2 and F3 – negative edge rounding and bright undulating extensive polish on concave working surface. All micrographs taken at magnification 200x.

LIA-216

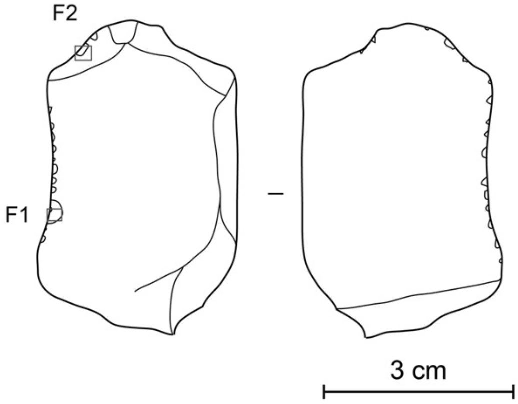

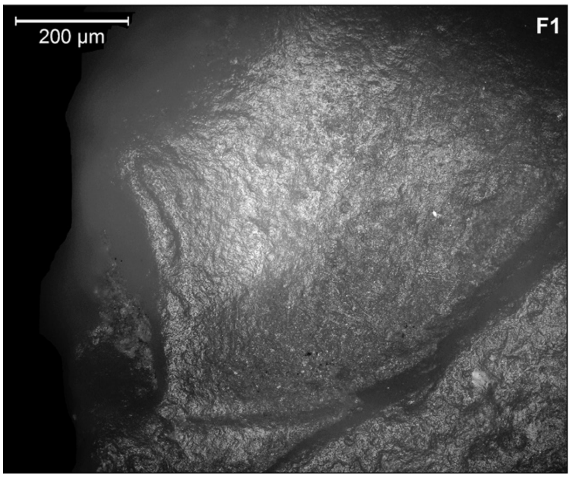

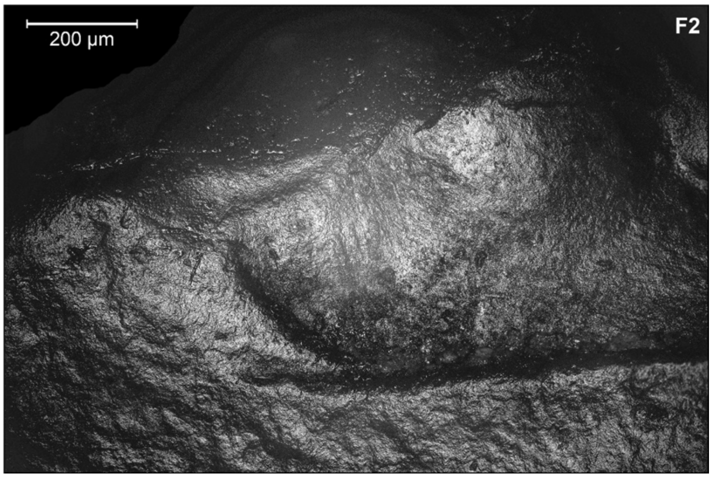

Figure S45 Schema of artefact LIA-216. F1 – micrograph of the polish showing the orientation and motion of tools use, note the micro pits and the undulating character of the micro polish; F2 – micrograph showing the rounded edges of the micro negatives and the lightly developed micro polish with parallel striations oriented perpendicularly to the working edge. All micrographs taken at 200x.

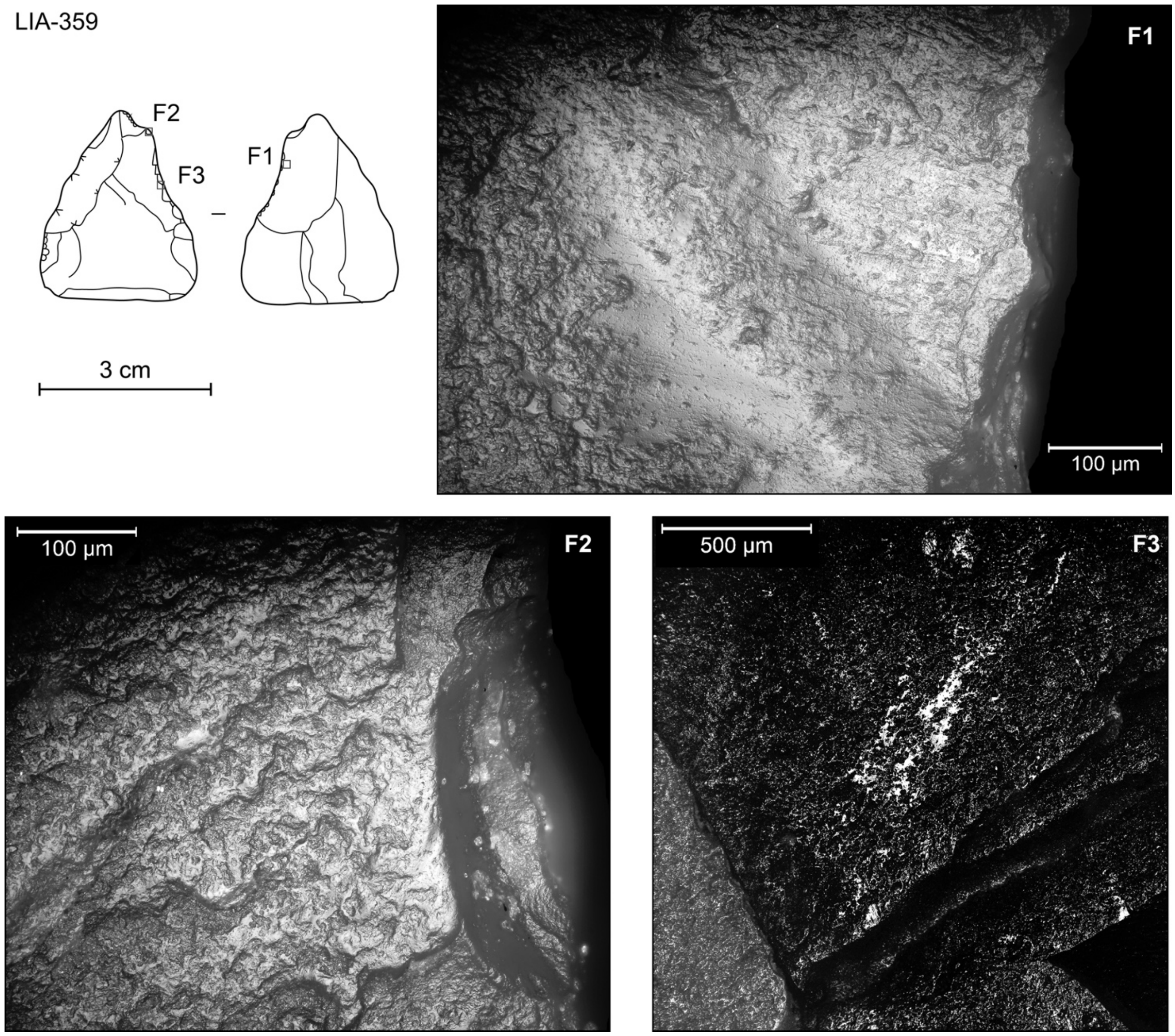

Figure S46. Schema of artefact LIA-359. F1 – micrograph showing the well-developed and interconnected bright undulating micro polish, micrograph at 200x; F2 – Micrograph showing the rounded edges of the negatives and the well interconnected undulating polish on the eminences of the micro topography of the stone tool edge, micrograph at 200x; F3 – bright and flat polish at magnification 50x.

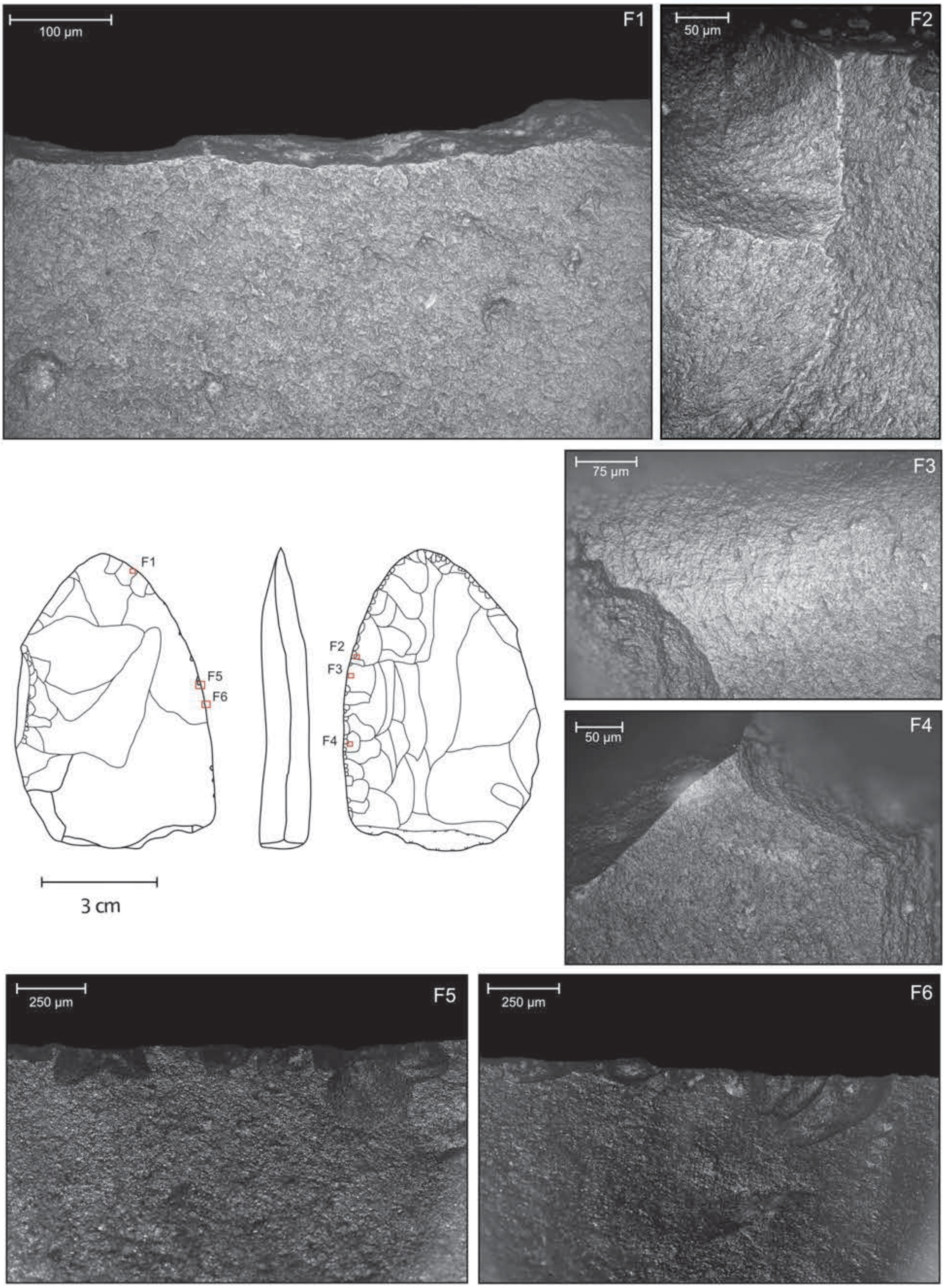

Figure S47. Keilmesser Li-7 from Lichtenberg. F1 – micrograph of the light developed bright polish on the edge of the active zone of the tool; F2 – micrograph showing the rounded and polished edges of the negatives on the dorsal surface of the working edge; F3 and F4 – micrographs of the striations on the interior of the dorsal side of the tools' working edge; F5 and F6 – micrographs of the micro-negatives on the ventral surface of the working edge.

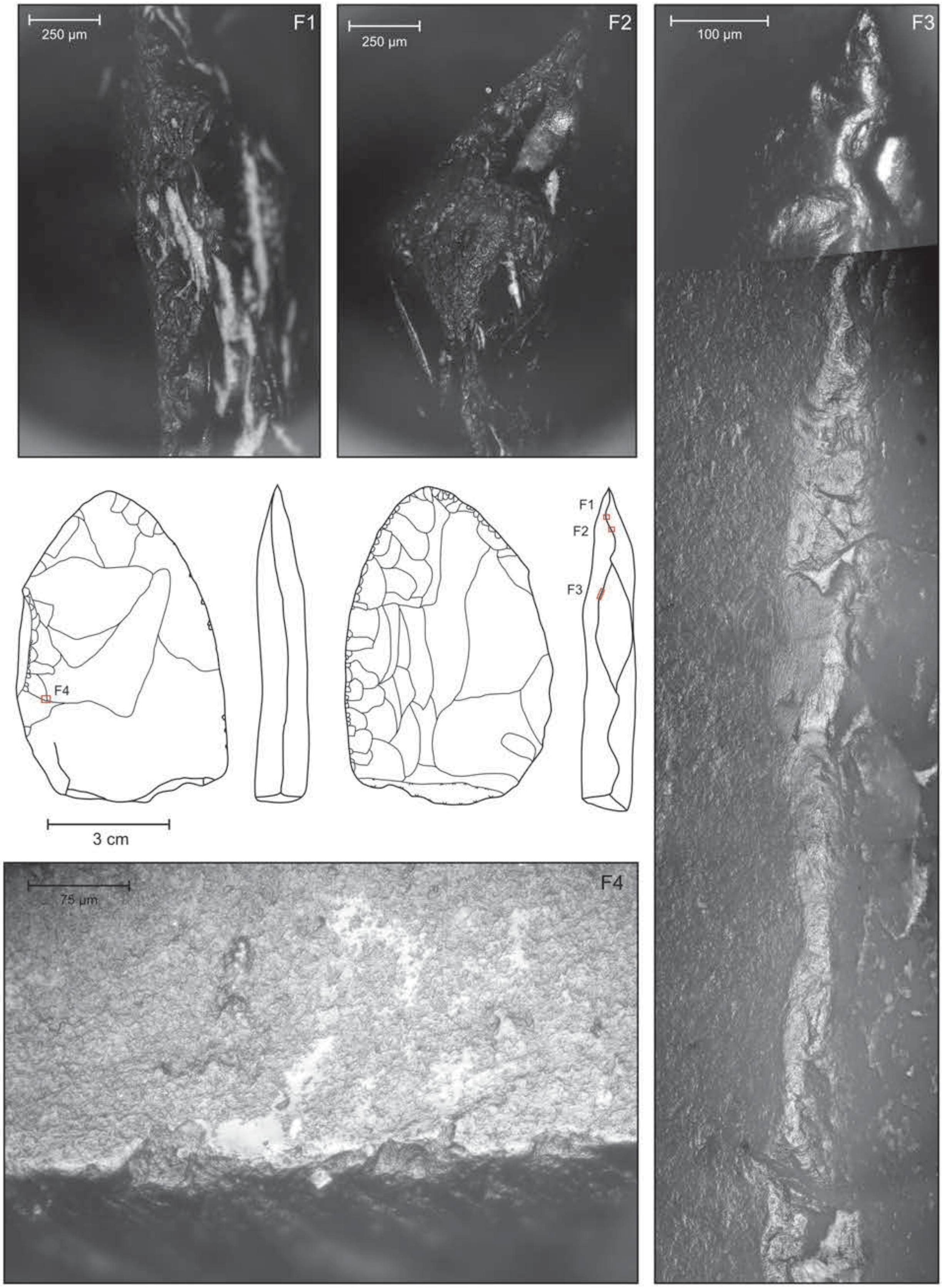

Figure S48. Traces on the prehensile/hafting zone of the Keilmesser Li-7. F1 and F2 – crushed and abraded edges on the back of the tool; F3 – composed micrograph images showing the undulating bright and well interconnected polish on the edge of the negative forming the back of the Keilmesser; F4 – bright undulating “G” type polish on the ventral surface of the tool.

References

Chan, B., Francisco Gibaja, J., García-Díaz, V., Hoggard, C.S., Mazzucco, N., Rowland, J.T., Van Gijn, A., 2020. Towards an understanding of retouch flakes: A use-wear blind test on knapped stone microdebitage. PLoS One 15, e0243101. https://doi.org/10.1371/journal.pone.0243101

Clemente, I., Gibaja, J.F., 1998. Working Processes on Cereals: An Approach Through Microwear Analysis. J. Archaeol. Sci. 25, 457–464. https://doi.org/10.1006/jasc.1997.0214

González-Urquijo, J.E., Ibañez-Estéves, J.J., 1994. Metodología de análise funcional de instruentos tallados en sílex. Universidad de Duesto.

Keeley, L.H., 1980. Experimental Determination of Stone Tool Uses: a Microwear Analysis. University of Chicago Press.

Moss, E., 1987. Polish G and the question of hafting, in: La Main et l'outil: Manches et Emmanchements Préhistoriques. G.S. Maison de l'Orient, pp. 97–102.

Rots, V., 2010. Prehension and hafting traces on flint tools: a methodology. Universitaire Press Leuven.

Semenov, S.A., 1964. Prehistoric Technology: an Experimental Study of the Oldest Tools and Artifacts from Traces of Manufacture and Wear. Barnes and Noble.

Vaughan, P.C., 1985. Use-wear analysis of flaked stone tools. University of Arizona Press Tucson.

Veil, S., Breest, K., Höfle, H.-C., Meyer, H.-H., Plisson, H., Urban-Küttel, B., Wagner, G.A., Zöller, L., 1994. Ein mittelpaläolithischer Fundplatz aus der Weichsel-Kaltzeit bei Lichtenberg, Lkr. Lüchow-Dannenberg. Germania 72, 1–66.

Supplementary Information S2 – Sections 5 to 8
Geo-Biosciences

Neanderthals in changing environments from MIS 5 to early MIS 4 in northern Central Europe – Integrating archaeological, (chrono)stratigraphic and paleoenvironmental evidence at the site of Lichtenberg

Marcel Weiss*[1,2], Michael Hein*[1], Brigitte Urban[3], Mareike C. Stahlschmidt[1], Susann Heinrich[1], Yamandu H. Hilbert[2] , Robert C. Power[4,1], Hans v. Suchodoletz[5], Thomas Terberger[6], Utz Böhner[6], Florian Klimscha[7], Stephan Veil[7], Klaus Breest[8], Johannes Schmidt[5], Debra Colarossi[9,1], Mario Tucci[3], Manfred Frechen[10], David Colin Tanner[10] & Tobias Lauer[1]

[1]Max Planck Institute for Evolutionary Anthropology, Leipzig, Germany

[2]Institut für Ur- und Frühgeschichte, Friedrich-Alexander-Universität Erlangen-Nürnberg, Erlangen, Germany

[3]Leuphana University Lüneburg, Institute of Ecology, Lüneburg, Germany

[4]Institute for Pre- and Protohistoric Archaeology and Archaeology of the Roman Provinces, Ludwig Maximilian University Munich, Germany

[5]Institute of Geography, Leipzig University, Leipzig, Germany

[6]State Service for Cultural Heritage Lower Saxony, Hannover, Germany

[7]Lower Saxony State Museum, Department for Research and Collections, Archaeology Division, Hannover, Germany

[8]Volunteer archaeologist, Berlin, Germany

[9]Department of Geography and Earth Sciences, Aberystwyth University, Aberystwyth, Wales, UK

[10]Leibniz Institute for Applied Geophysics, Stilleweg 2, Hannover, Germany

Section 5: Stratigraphic framework

5.1 Field descriptions and interpretation

Layer 1 is a ploughing horizon, developed in layer 2 and the humic topsoil that formed in layer 2 during the Holocene.

Layer 2 consists of gravelly, slightly silty and loamy sand, which is very poorly sorted and unbedded, i.e. massive. Its vertical extent coincides with a distinctly brunified Bw-horizon of a Cambisol. In some places, there is an accumulation of coarser gravel (stoneline) at its lower boundary. However, more often, a gravel concentration is found in the central parts of the layer. These characteristics are typical for a phenomenon called 'Geschiebedecksand' (GDS, periglacial cover sand), which is ubiquitously observed in the northern German lowlands. Its genesis is still a matter of debate, but there is general agreement, that different periglacial processes contributed, most importantly solifluction with a varying aeolian influx. The GDS is thought to have formed as a cold stage deposit during the late or latest Weichselian in MIS 2 (Altermann et al., 2008; Grimmel, 1973; cf. Semmel and Terhorst, 2010).

Layer 3 is characterized by slightly gravelly and silty, poorly sorted, yellow medium sand. The structure varies between a well-bedded planar to trough-like lamination and entirely structureless segments. The layer is interveined by thin gravel beds/stonelines, the most pronounced situated at the lower boundary, where occasional wind-facetted pebbles occur. These stonelines are very common in periglacial deposits of northern Central Europe and are usually interpreted as erosional residues or deflation beds (Van Huissteden et al., 2000; Zagwijn and Paepe, 1968). Accordingly, an alternation of solifluction, slopewash and likely aeolian influence needs to be assumed for the formation of layer 3 (cf. Fränzle, 1988; Richter et al., 1970). In that regard, it is related to layer 2 above, which is confirmed by grain size analysis (Fig. 3, main text, Supplementary Section 5.2). Contrary to layer 2, evidence for pedogenesis is missing. Frost features (involutions and cracks) can be observed in layer 3, but it is unclear, whether they developed in conjunction with MIS 4 or MIS 2 permafrost processes.

Layer 4 contains finely laminated, wavy plane-bedded, pale yellow, moderately to poorly sorted, fine to medium sands, which are interbedded with thicker lenses of better sorted medium sands, similar to those of layer 5. Occasionally, the mm to cm thick laminae of layer 4 are interspersed with organic matter (plant fibers), that might be redeposited residues from an upslope interglacial or interstadial. Genetically, this sediment is interpreted as a niveofluvial to niveoaeolian deposit, triggered by annual snowmelt and associated slopewash in loosely vegetated conditions. The lenses of better sorted sands (cm to dm scale) are either produced by erosional redeposition of aeolian sands (e.g. from layer 5) on the slope or by contemporaneous aeolian saltation processes, alternating with the slopewash (Christiansen, 1998a; Christiansen, 1998c; Van Huissteden et al., 2000). Niveofluvial and niveoaeolian deposition is known to have been one of the most important geomorphic processes in the former periglacial areas of northern Central Europe (see references for layer 8/9). Post-depositionally, layer 4 has experienced a cryogenic overprint in the form of involutions, updoming and frost-cracking. In such clear ex-situ positions, the layer is referred to as 4'.

Layer 5 comprises very loose, yellow medium sands that are better sorted than in the surrounding layers. In Trench 2, they are sheet-like (ca. 10 cm thickness) and sometimes display an inclined, fine bedding (dip angle of ca. 15°), possibly indicating foreset-lamination. However, in Trench 1, they are predominantly structureless, macroscopically massive and frequently subjected to former cryoturbation, in that case referred to as layer 5'. The interpretation of layer 5 as an aeolian sand, transported and deposited by saltation rather than in suspension is supported by micromorphology and grain size analysis (cf. reference given there). Thin aeolian sand sheets with limited lateral extent and well-sorted medium sands are commonly found in periglacial Weichselian sequences of Central and Western Europe (Schwan, 1988; cf. Vandenberghe, 1992).

Layer 6 is characterized by unbedded, poorly to moderately sorted, fine to medium sands with an orange oxidation color. The latter is likely due to lepidocrocite dominance, inferred from the high chroma values in the Munsell colors (between 6 and 8). Lepidocrocite is formed in redoximorphic environments by episodic water logging and might be related to permafrost processes but also fluctuating groundwater levels (Cornell and Schwertmann, 2003). Layer 6 cannot be assigned to any depositional process with confidence, so far. This is mainly because of its low extent in the sequences, rendering it impossible to distinguish between original properties and posterior alterations by cryogenesis or hydromorphic conditions. Furthermore, because of the patchy occurrence and undiagnostic features in the field, only one grain size sample has been taken and analyzed from layer 6 (sample 22, Fig. 3, main text). A ferruginated zone on top of layer 7 (see there) might actually be a pedogenic feature of layer 6. This hypothesis is strengthened by a three-part banded occurrence of this ferrugination in the northern section of Trench 1 (Supplementary Figure S 50), where the individual members are separated by medium sands seemingly belonging to layer 6. Additional exposures within the excavation area in Lichtenberg might help to resolve this ambiguity in the future.

Layer 7 is a thin bed (< 15 cm) of whitish, very poorly sorted fine sandy silt to silty very fine sand that appears to be massive in macroscopic examination (but weakly bedded in thin sections; Supplementary Figure S 53, Supplementary Section 5.3). Notably, it has a very brittle and dense structure, therefore it is not easily deformable but all the more easy to recognize even in cryoturbated segments that occur as injections and diapiric structures (layer 7'). At the study site, this deposit covers extensive areas as a thin veneer with distinct upper and lower boundaries. Given that the site is situated alongside an Eemian to Weichselian palaeolake (Hein et al., 2021), we interpret this layer as a lacustrine, muddy shoreface deposit, which is typical for small lakes with very narrow coastal belts. According to Cohen (2003, cf. Bridge and Demicco, 2008) this facies frequently shows very thin laminar beds but is often massive due to bioturbation or rapid deposition. In Trench 2 (Fig. 2c, main text), layer 7 is intertonguing and alternating with the underlying slope deposits of layer 9. A bit further upslope the individual filamentary members of layer 7 first unify in a single layer and then wedge out shortly afterwards. Throughout the sequence, at the upper boundary of layer 7, a brown-orange ferrugination can be observed, seemingly formed in overlying medium sands (layer 6?) that became cemented by the process. The Munsell color implies that ferrihydrite might be the dominant iron oxide here (Cornell and Schwertmann, 2003). This ferruginated zone encroaches into the whitish silty deposit of layer 7 along a drop-shaped boundary, resembling a micro-drop soil on a mm to cm-scale. While a pedogenic influence cannot be ruled out (Supplementary Section 5.3), the origin of this overlying iron-cemented medium sand is not clear therefore the stratigraphic and chronological relationship of a possible soil formation with layer 7 is uncertain. This question will be the topic of a follow-up publication. Both the in situ layer 7 and the cryoturbated expression 7' accommodate Middle Palaeolithic artefacts and comprise the main part of the archaeological find horizon Li-I.

Layer 8 consists of fine to medium gravelly, medium sands that are poorly sorted, crudely to non-bedded and possess a greyish to light brown color with redoximorphic features. This deposit is only present in Trench 1 and its upper 5 to 10 cm contain lithic artefacts as part of the archaeological find horizon Li-I. Interpretation will be undertaken together with layer 9.

Layer 9 is a thick deposit (40 cm to >1 m) of finely laminated, wavy plane-bedded and moderately to poorly sorted fine to mediums sands with greyish to light brown color. In some places, it is streaked with horizontal or mottled iron oxide accumulation. In Trench 2 (western section) the layer is interbedded with the lacustrine sediments from layer 7 (see there), in the eastern section it is heavily distorted by cryogenic processes (cryoturbation/solifluction). In Trench 1 (southern section) it is contained within a cryoturbation pocket. We refer to these reworked segments as layer 9' (Fig. 2, main text). The thin, wavy lamination and the granulometric properties (Supplementary Section 5.2) clearly lead to an interpretation as niveofluvial slopewash sediment, whose deposition was induced by annual snowmelt (Christiansen, 1998b). Layer 8 was likely formed by the same process, only that higher-energy slopewash also transported pebble-sized grains. This points to comparatively more intense melting, which often results in a massive, unbedded structure (cf. Christiansen, 1998c). Niveofluvial processes played a major role in the erosion and re-shaping of periglacial landscapes during the Weichselian in Central and Western Europe (Lade and Hagedorn, 1982; Menke, 1976; Zagwijn and Paepe, 1968).

Layer 10 is a very thin veneer (<10 cm) of fine-sandy to loamy silt with gleyic properties and a very slight organic carbon (C_{org}) content. Appearing massive in the field, the layer shows clear bedding structures in thin sections (Supplementary Section 5.3, Supplementary Figure S 52). It possesses particularly distinct upper and lower boundaries. Only present in Trench 2, layer 10 emerges from layer 11b and covers extensive parts of layer 11a, but wedges out towards higher ground in the northern half of Trench 2 (cf. Fig. 2 main text). The layer discontinuously contains very thin humic veins of a few mm thickness. Contrary to the overlying sediments, layer 10 has not been affected by cryoturbation in the observed exposure. In terms of thickness, structure and texture, it shows a strong resemblance to layer 7. Therefore, just like the latter, layer 10 is interpreted as a muddy, lacustrine shoreline or shoreface sediment, deposited within the narrow coastal zone of a small lake (Bridge and Demicco, 2008; Cohen, 2003). The humic vein is taken to represent a drift line (cf. Supplementary Figure S 52), formed by wave activity that reworked organic compounds (possibly from layer 11b) in the intertidal zone of the lake.

Layer 11 only occurs in Trench 2, does not display apparent cryogenic deformations and has a bipartite nature (11a and 11b). Both members incorporate lithic artefacts of the archaeological find horizon Li-II, with the highest find densities existing in the uppermost 11 cm of 11a. *Layer 11a* consists of a slightly humic, very silty, very poorly sorted fine sand, that appears massive in the upper ~40 cm, but gradually changes to a crude, weakly inclined (consequent) bedding and a notable redoxidmorphic mottling underneath. The archaeologically relevant upper part also contains high abundancies of charred organic matter. Additionally, in the uppermost 10 cm on the slope near the contact with layer 11b, various, stacked humic veins occur (Supplementary Figure S 59). In the northern part of Trench 2, where layer 10 is wedging out (see there), a ca. 10 cm thick half-bog horizon developed within and on top of layer 11a. The presence of this half-bog and layer 10 seems to be mutually exclusive, which might point towards an erosive contact between both layers. This palaeosol will be the subject of a follow-up publication. *Layer*

11b is a peaty, detrital and sandy mud, that becomes more silty and fine-detrital towards the north in Trench 2 (layer $11b_2$) (Supplementary Figure S 59). Generally, layer 11b is directly overlain by layer 9. However, in some places very shallow kettles on the surface of layer 11b (due to slight subsidence) accommodate a thin (<1 cm) grey silt, that might correlate with layer 10. While in the eastern section of Trench 2 the stratigraphic relationship between layers 11a and 11b remains rather ambiguous (possibly due to erosion or settlement/slippage of neighboring deposits – see below), it can be clarified in the western section (Fig. 3b/c, main text, Supplementary Figure S 59a/b). A branch of $11b_2$ is horizontally extending to the north and turns into a highly humic sand, which clearly interfingers with layer 11a. Consequently, the two sub-layers can be regarded as stratigraphically contemporaneous, even though layer 11a started forming shortly before 11b, because it not only interfingers with, but also underlies the latter. In small closed-basin lakes, sediments of the actual lake and the coastal plain are hardly distinguishable, because of usually significant water table fluctuations that alternatingly expose or inundate certain deposits. We understand layer 11 in its entirety to comprise different coastal-lacustrine environments (cf. Bridge and Demicco, 2008; Cohen, 2003; Mania and Toepfer, 1973). Layer 11a as a beach face deposit, situated next to the shoreline represented by layer 11b. Beach deposits are often lakeward-dipping, but can be massive around small lakes due to low wave energy or bioturbation. The vertical and lateral extent of the beach deposit is shown in Supplementary Figure S 49a. It possesses a constant thickness of just under 1 m and can be traced along a section of ca. 30 m in the accompanying coring transect (Hein et al., 2021). These dimensions and the silty, fine sandy texture are typical for small-lake beach faces (see references above). In Trench 2, the stacked humic veins in the uppermost part of the downslope segment in layer 11a represent drift lines (compare layer 10), formed by wind driven waves that ran on the beach, depositing organic compounds and redistributing beach sands. From the stacked, multi-generation nature of these drift lines, a prograding lake with a rising water table can be inferred. This also caused the deposition of the peaty layer 11b (which partially overlies layer 11a) in shallow waters near/at the shore. Beyond that, the lateral contact zone between the more aquatic 11b and the beach deposit of 11a seems to be complex and variable, with very small-scale differences. Whereas in the western section of Trench 2, this contact shows an interfingering of both deposits, the situation in the eastern section resembles that of a minor wave-cut niche (Supplementary Figure S 59).

The lithostratigraphy of core PD.028 (for position see Fig.1, main text) is presented in Supplementary Table S 11.

5.2 Grain sizes analysis

Scatter plot (Fig. 3a, main text)

The aeolian sands, found in layer 5, were initially thus described for their remarkably loose sedimentary structure and the microscopic impact scars on the individual grains (see Supplementary Section 5.1). This group shows the best sorting (median of 1.7) and the highest mean grain size (median of 354.0 µm), which is in line with typical values for saltated sand both in wind tunnel experiments and field-based investigations (Cheng et al., 2015; Farrell et al., 2012; cf. Schwan, 1988). The niveofluvial (layer 9) and niveofluvial to niveoaeolian (layer 4) sands were treated as a coherent group statistically, because the processes are genetically related and difficult to distinguish in the palaeorecord (see Supplementary Section 5.1 above). Niveofluvial and niveoaeolian sands are common phenomena in Weichselian slope deposits of northern Central Europe (e.g. Zagwijn and Paepe, 1968) and usually consist of thin-bedded fine to medium sands. In our data, the typical grain size is reproduced (median of 227.6 µm). The depositional process results in a slightly poorer sorting, compared with the aeolian sands (median of 2.2). The niveofluvial to niveoaeolian layer 4 contains lenses (up to 10 cm thick, up to 15 cm long) of coarser sand that seem to derive from the aeolian layer 5 below. Samples 2 and 20 were taken from these lenses and confirm that relatedness by their position at the intersection of both grain size clusters (compare Fig. 3b, main text). The solifluctive layers 2 and 3 feature the highest gravel contents by far and thus the statistical data are somewhat distorted by excluding this fraction from the analysis, which is also the reason for the relatively low mean grain sizes (median of 227.0 µm). Nevertheless, the poorer sorting (median of 3.4) still separates this group from the aforementioned. The overlap of sample 18 with the niveofluvial/-aeolian deposits is likely caused by solifluction alternating with slopewash deposition for layer 3 (see Supplementary Section 5.1, compare Fig. 3b, main text). The lacustrine deposits are set apart by their very poor sorting and lowest mean grain sizes and can be subdivided according to their position within the coastal zone (Supplementary Section 5.1). Samples 24, 25 and 28 (layer 11b, find horizon Li-II) belong to the beach face deposit, with a mean grain size of 80.7 µm (median of the three samples) and a sorting of 7.3 (median of the three samples). The remaining two lacustrine clusters represent thin, muddy shoreface deposits from layers 7 (find horizon Li-I) and 10 with median values for the mean grain sizes of 58.8 µm and 16.5 µm, respectively. Both show similarly poor sorting of 5.6 and 5.2.

Principal Component Analysis (PCA) (Fig. 3b, main text)

Whereas for the scatter plot only two descriptive parameters were taken into account, the PCA is based on all 116 dimensions of the grain size fractions. Between them, PC1 and PC2 explain 95.8 % of total variance of the data set. The associated biplots display the relative influences of the categorical grain size fractions clay, silt, fine/medium/coarse sand on the analysis of the data. The results strongly resemble those of the scatter plot and the same clusters, based on field descriptions can plausibly be formed. The biplots reveal, that the aeolian, niveofluvial-/aeolian and soliflucitve deposits are distinguished by their contents of the different sand fractions, while the position of the lacustrine members within the data matrix is mainly determined by their relative silt and also fine sand contents.

5.3. Micromorphology

We here report on the micromorphological analyses of five block samples from the 2019 excavation Trenches 1 and 2 at Lichtenberg (for sample locations see Fig. 2, main text and Supplementary Figure S 50). Sampling concentrated on the two archaeological find layers, Li-I and Li-II, and associated, under- and overlying lithofacies. From the bottom up, the analyzed sequence contains (field interpretations in brackets): layer 11b (peaty mud), layer 11a (humic sand) and archaeological layer Li-II at its top, layer 10 (clayey silt), layer 9 (niveo-fluvial sands) as well as layer 7 (silty fine sand) containing archaeological layer Li-I and the overlying layer 6 (orange fine to medium sand). In the following we describe and interpret each layer and note where differences exist between thin sections of the same layer.

The lower sequence contains layers 11a, 11b, 10, 9 as well as archaeological find horizon Li-II and is present in two thin sections from Trench 2 (Fig. 2, main text and Supplementary Figures S 51, 52). The two thin sections reflect lateral variability in the sequence here, layer 9 is only present in LIB 19 5 (SI fig. 2), while layer 11b and 10 are only preserved in LIB 19 4 (Supplementary Figure S 52). Starting from the bottom, layer 11a is mainly composed of (sub)rounded, generally unsorted silt to coarse sand sized quartz grains (Supplementary Figure S 51f, g), but some lenses with coarser grains were observed as well and a slight coarsening upwards. The next common component are plant residues in the form of amorphous organic staining to plant tissues and organs (Supplementary Figure S 51d, e). Elongated plant tissue have a tendency for horizontal alignment (Supplementary Figure S 51c) indicating a waterlain nature (Taylor et al., 1998). This is in accordance with the macroscopic interpretation of this phenomenon as a drift line at the shoreface of a small lake (section 4.1, main text and Supplementary Section 5.1). Few mica, flint, charcoal (Supplementary Figure S 52f) and unidentified heavy minerals are also present. Void space is mainly limited to simple packing voids, but a few channels are present as well, which are often filled with clay (Supplementary Figure S 52e, g), supporting periods of surface stabilization with vegetation growth and incipient soil formation (Bouma et al., 1990). Fine material is sparse and composed of brown to grey (only in LIB 19 4) clay, which is arranged in porphyric or a weakly developed chitonic and gefuric related distribution. In thin section LIB 19 5, layer 11a is overlain by layer 11b, a peaty deposit, with a clear, but gradual conformable contact. The two layers show only limited compositional or structural differences. In layer 11b, the occurrence of a possible krotovina feature indicates more intense bioturbation here. The main difference between these two layers, however, is an increase in the number and size of organic residues in layer 11b compared to layer 11a, which may reflect a greater proximity to the shore or lower energy setting for layer 11b compared to layer 11a (Dobrowolski et al., 2001). At the same time layer 11b shows internal stratification (Supplementary Figure S 51c), in the upper part, organic residues are dominantly composed of cells and tissue residues (Supplementary Figure S 51b), while in the lower part larger tissues to organs (Supplementary Figure S 51d, e) were deposited, reflecting an upward increase in energy or greater transport distance of the organic material with increasing distance to the shore (Cohen, 2003; Taylor et al., 1998). Overall layer 11 shows characteristics of a shore environment with repeated flooding events and periods of surface stabilization, potentially the eulittoral zone of a lake (Bouma et al., 1990).

In thin section, the contact between layer 11 and the overlying layer 9 and 10 respectively is clear with the two overlaying layers showing slight compositional and structural differences. In thin section LIB 19 4, layer 10 is characterized by bedded sands and silt (Supplementary Figure S 52a-c). At the top of this thin section a red orange layer is present (Supplementary Figure S 52a, c), where the same depositional bedding structure is present but overprinted by post-depositional iron oxidation. The contact with the red orange layer is sharp and potentially presents an former groundwater line (Fedoroff et al., 2010). The main components in layer 10 are medium to coarse or fine to medium sand sized quartz grains, while mica, plant residues and heavy minerals are rare. Void space dominantly consists of simple packing voids with few chambers and fissures, which are filled with dusty and limpid clay coatings. Clay is arranged in a porphyric to chitonic and gefuric related distribution. Thin sections LIB 19 5 preserved the contact between layer 11b and 9 (Supplementary Figure S 51a) but only a limited exposure of layer 9 (Supplementary Figure S 51c), which shows a slightly different expression from layer 10. Layer 9 is moderately sorted for medium sand sized quartz grains. Rare components – mica, plant residues, heavy minerals – are the same, but organic-rich soil aggregates and charcoal present additional, rare components here. A further difference, but of minor magnitude only, is the more common and thicker occurrence of clay coatings here (SI fig. 2a).

The upper sequence contains layers 5, 6, 7, archaeological find horizon Li-I and is present in three thin sections, two from Trench 1 (LIB 19 1 and 2, Fig. 2 in the main text and Supplementary Figure S 54, 55) and one from Trench 2 (LIB 19 3, Fig. 2 in the main text and Supplementary Figure S 53). Starting from the bottom, layer 7 containing the find horizon Li-I shows the same expression in all three thin sections. This layer is composed of weakly bedded (sub)rounded quartz grains, which are silt to sand sized, but the layer is poorly sorted for silt and fine sand (Supplementary Figures S 53f, g; 54e, f; 55f, g). Other components include mica and clay, which are both rare. The microstructure is very compact, grain supported and only simple packing voids were observed. A great degree of compaction is a unique characteristic of this layer and it resembles a fragipan but for the lack of pedofeatures. The contact with the overlaying layer 6 is clear and characterized by an increase in sand sized quartz and clay here (Supplementary Figures S 53c-e; 54c, d; 55c, f, g). Grains in layer 6 are dominantly composed of (sub)rounded silty to coarse sand sized quartz grains (Supplementary Figures S 53d, e; 54a, b; 55d, e), but silt sized grains are rare. However, in thin section LIB 19 3 this increase in grain size and the contact zone extends over almost 1 cm and is also characterized by amorphous organic staining (SI fig. 4c, e), reflecting local variability. Further variation is visible in the interstitial clay component. Clay is arranged in a gefuric related distribution and as clay illuviation, most expressed in LIB 19 2 (Supplementary Figure S 54a, b), while in LIB 19 1 the upper part of this layer shows only thinly expressed clay coatings (Supplementary Figure S 55a-c). There are also color changes in the clay. In LIB 19 3, the clay is generally brown reddish, resulting from iron staining (Supplementary Figure S 53b, d). In LIB 19 1 and 2 the color changes from grey over dark or black to reddish brown (Supplementary Figures S 54b; 55d, e). This pattern may indicate spatial variation in water saturation (Fedoroff et al., 2010). Otherwise, layer 6 shows a dense, massive microstructure with simple packing voids and is grain supported. The contact with the overlaying layer 5 is clear and conformable in LIB 19 2 (SI fig. 6), but gradual in LIB 19 3 (SI fig. 4c). The structure and composition of layer 5 is similar to layer 6, and the main difference is the thinner and more scarce nature of clay coatings here, but again LIB 19 3 shows a slightly different expression with thicker clay coatings (Supplementary Figure S 53a, b) compared to LIB 19 2. Furthermore, LIB 19 3 shows weak bedding.

Section 6: Robustness of luminescence ages

6.1 Testing and choice of measurement protocol

On three samples (L-EVA 2013, 2016 and 2021) from the two trenches, we performed a dose recovery and an anomalous fading test using three aliquots each. After bleaching in the solar simulator for 3 h, the dose recovery test was conducted with three different protocols for potassium feldspar: $pIRIR_{225}$, $pIRIR_{290}$ and $pIRIR_{290}$ with a hotbleach. For further measurements and age calculations, we opted for the $pIRIR_{290}$ hotbleach protocol (summarized in Supplementary Table S 12), as it produced the most reliable residual-subtracted measured-to-given dose ratios (0.98, Supplementary Figure S 56). This approach has been shown to produce robust luminescence ages and to be less prone to anomalous fading (Thiel et al., 2011; Thomsen et al., 2008). We measured the signal stability following Huntley and Lamothe (2001) and obtained a mean g-value of 2.2%/decade (Supplementary Figure S 56). Hence, the ages were not fading corrected so as to avoid age overestimations (cf. Arnold et al., 2015; Buylaert et al., 2012). Even though L-EVA 2013 and 2021 were later excluded from the scope of this publication, their measured to given dose rates and g-values are fully representative for the measured samples described in the main text. The ages of L-EVA 2013 and 2021 will be reported in a forthcoming publication.

6.2. Dose rate determination

The results of the high-resolution germanium gamma spectrometry are presented in Supplementary Table S 13. To calculate the total dose rates, the contribution of cosmic radiation was accounted for based on Prescott and Hutton (1994). For the internal beta dose rate contribution we assumed an effective potassium content of 12.5 ± 0.5 % (Huntley and Baril, 1997), furthermore, we applied radioactivity conversion factors suggested by Guérin et al. (2011). An a-value of 0.11 ± 0.02 was used to approximate alpha particle efficiency (Kreutzer et al., 2014).

6.3 D_e-estimation

After measuring the independent equivalent dose (D_e) estimates for each sample, we used Abanico plots for exploration and visualization of the data (Supplementary Figures S 57, 58). Abanico plots combine the benefits of radial plots, suitable for depicting the precision of individual D_e-values, with kernel density estimates (KDE), which more comprehensively show

D_e frequency distributions (Dietze et al., 2016). This amalgamation allows for an enhanced identification of patters within the individual D_e-estimates (Galbraith and Roberts, 2012). An adequate inspection of the distributions, however, requires a sufficiently small bandwidth (bw) for the univariate KDE part of the plot, preventing over-smoothing of the curve and associated loss of data variability (ibid.). Therefore we chose the bw to achieve an accordance between the radial plot and KDE representation of the data and based on the bw-selectors “bw.ucv” and “bw.nrd0” as implemented in the r.luminescence package (Kreutzer et al., 2020). The choice of dose model for the final D_e-estimation ensued according to the most meaningful cluster and peak in the Abanico plot with respect to the depositional process and characteristics of the sediment (Tab. 1, main text). As a tendency, samples from the niveofluvial layers 8 and 9 and the beach sand (layer 11) were mostly subjected to the central age model (CAM), whereas the aquatic deposits of layer 7 were treated with the minimum age model (MAM), using a σ_b-value of 0.11 (e.g. Cunningham and Wallinga, 2012). In one instance, for sample L-EVA 2024, with a complicated depositional history of short-distance reworking on the slope and suspected posterior bioturbation by trampling, we opted for the weighted mean, because no other age model was in better compliance with the distribution.

Sample L-EVA 2010 was taken from a stratigraphic position where the archaeological find horizon Li-I is injected upwards through cryoturbation. The obtained age of 53.5 ± 4.9 ka (applying MAM) does not refer to the deposition of the sediment, but to the cryoturbation incident, whereas the main mode of this sample’s KDE curve (159.1 Gy) results in an age of 64.6 ± 5.8 ka and thus better corresponds with the in situ samples from the same layer (L-EVA 2014, 2015 and 2018; 70.8 ± 8.0 to 71.6 ± 7.0 ka). However, the cryoturbation age of L-EVA 2010 (53.5 ± 4.9 ka) is in line with the date of 57 ± 6 ka that was previously presented for the same find horizon in Lichtenberg (Veil et al., 1994). Hence, there is evidence to suggest, that unmixing distinct age populations (original deposition and cryoturbation event) in very small (0.5 mm) multiple grain aliquots is to some extent possible, if the genuine age of the initial deposition is known from independent samples. For the previous chronology, an in situ representation of the find horizon was not available, because the depth of the non-cryoturbated layers had not been reached during the preceding excavation (cf. Fig. 2a, main text). So while the actual former age appears to be comparably accurate, its stratigraphic and archaeological interpretation needs to be updated in view of our data.

Section 7: Palynology

7.1 Detailed sample preparation

All samples were treated by standard methods (Faegri et al., 1989; Moore et al., 1991). About 5 g of sediment were prepared per sample, including dispersion with 10% KOH, flotation using sodium polytungstate hydrate ($3\ Na_2WO_4 \cdot 9\ WO_3 \cdot H_2O$) and acetolysis to dissolve cellulose. Residues were embedded in glycerine and up to three slides (24 x 32 mm) per sample were analysed under a transmitted light microscope for pollen and non-pollen palynomorphs at 40x magnification. Pollen and spores were identified using the atlases of Faegri and Iversen (1989), Moore et al. (1991) and Beug (2004). Micro-charcoal particles smaller than 100 µm were counted in samples of Trench 2 of the excavations (2019 and 2020) and are presented by a curve for each 24×32 mm slide in the pollen diagrams.

7.2 Results and Interpretation

7.2.1 Bulk samples 1, 2, 3 and 8 (excavation 2019, Trench 2)

Results

The pollen and spore content of the four analysed samples is low but sufficient for statistical evaluation, although pollen preservation is partially poor. For sampling positions, see Fig. 2 main text, Supplementary Figure S 59. The three lowermost samples of layers 11a, 11 b and 11 b_2 (samples 1 to 3) are rather similar concerning their AP and NAP assemblages. They are characterized by high values of *Pinus* (60%) and *Betula* (20%) and some *Salix*, whereas Poaceae amount to 10% and total NAP to 15% (Supplementary Figure S 60). Very few *Picea* pollen occur (samples 2, 3) and single grains of the thermophile trees (*Quercus* and *Carpinus*), most probably reworked from subjacent Eemian layers. Additionally, *Alnus, Larix, Myrica* and *Juniperus* occur in layer 11 b_2 (sample 3). The pollen spectra of all four samples are furthermore characterized by the occurrence of cryptogam spores (*Ophioglossum, Botrychium* and *Selaginella selaginoides*) and by low amounts of Cyperaceae and Ericaceae (mean about 5%) in layer 11b_2 (sample 3). Very few pollen of aquatic taxa such as *Potamogeton*, *Sparganium* type, *Typha latifolia* type and of wetland plants like *Montia* and taxa representing the *Ranunculus acris* pollen type (including for example *R. acris, R. aquatilis, R. sceleratus*) have been found. Remains of a coenobium of the green algae *Pediastrum* spec. occur. *Sphagnum* peaks in sample 2, layer 11b (30%), but is present in all four samples.

Particular differences between the pollen assemblage of the topmost sample 8 (drift line within layer 10) and those of the underlying layers are a strong decrease of *Pinus* (15%) and increase of Poaceae up to 40% and of total NAP to about 50%, whereas the *Betula* curve has slightly increased (>20%). The micro-charcoal particle counts increase from bottom (sample 1, layer 11a) to top (sample 8, layer 10 [drift line]) from 6 to 260) (Supplementary Figure S 60).

Discussion

From the palynological record, a shallow water body and a swampy environment can be concluded for the lowermost three layers (11a, 11b and 11b$_2$). This is indicated by the occurrence of the aquatic, wetland and boggy, peat-forming taxa *Pediastrum, Ranunculus cf. sceleratus, Typha spec., Sparganium spec., Montia*, Polypodiaceae, *Sphagnum*, Ericaceae, *Myrica* and *Junipe*rus. Behre et al. (2005) describe macro remains of *Ranunculus sceleratus* for the Brörup and Glinde interstadials. The presence of the Ophioglossaceae ferns *Ophioglossum* spec. and *Botrychium cf. lunaria* points to sandy, humic open stands, as for example meadows or heathland. The arctic-alpine, as well light-demanding *Selaginella selaginoides* found in layer 11 b$_2$, known from Late Glacial plant communities, has probably occupied peat bogs or other open moist stands, like meadows. *Selaginella selaginoides* macro-remains are recorded from the Early-Weichselian Rederstall Stadial and Pleni-Weichselian Glinde Interstadial (Behre et al., 2005), pointing to opening-up of the landscape and most probably to a temperature drop.
The azonal vegetation observed in samples 1, 2, 3 and 8 records a gradual change in vegetation and climate from the (late) Brörup Interstadial to the Rederstall Stadial. From an open boreal pine-birch forest (layer 11a and 11b) with a relatively rich undergrowth of mosses and grasses in association with wetter and dryer heliophyte (*Larix*) and grass rich stands, it likely shifted to slightly lighter and cooler conditions towards the end of the interstadial (layer 11b$_2$). Finally, the uppermost layer 10 indicates the development of a grass rich open, *Betula* dominated Steppe-Tundra, caused by a strong climatic decline in the following Rederstall Stadial.

7.2.2 Trench 2, excavation 2020 (samples 4 to 7)

Results

High resolution analyses of 4 samples (4 to 7) from the ca. 8 cm thick, peaty and sandy detrital mud (layer 11b), shows a medium to poor pollen preservation. The directly overlying thin silt (part of layer 10?) (Fig. 2c, main text) has been sterile on the other hand (Supplementary Figure S 59).
The bottom sample 4 (0-2 cm) of layer 11b has a similar pollen assemblage as layers 11a, 11b and 11 b$_2$ in the bulk samples 1 to 3 (Supplementary Figures S 59a,b; 61.). *Pinus* is the predominant woody taxon (60%), followed by *Betula* (20%). *Salix*, *Juniperus, Larix, Alnus, Picea* and *Myrica* occur with values between <1-2%. NAP are mainly composed of Poaceae

(10%), Rosaceae, Caryophyllaceae, *Artemisia* and Asteraceae and reach 15% in total. The sum of Ericaceae amounts to 6%; Sphagnum is present with 11% and Polypodiaceae with 4%. Only single grains of *Typha latifolia* type and *Sparganium* type were found. Micro-charcoal counts amount to 280 particles. The subsequent sample 5 (2-4 cm) shows a slight increase of *Betula* (31%) and *Myrica* (2%) and of NAP (19%), mainly composed of *Artemisia*, Asteraceae and Rosaceae. Few pollen of Chenopodiaceae occur in this depth and in the overlying sample 6 (4-6 cm). Amounts of Poaceae and of *Pinus* have decreased down to 7.5% and to 45.5% respectively. Pollen of *Polygonum bistorta* type (syn. *Bistorta officinalis*) appear for the first time. Among the aquatic taxa, *Myriophyllum spicatum* is recorded by a single grain, whereas the amount of *Typha latifolia* type has increased. Micro-charcoal particles amount to 828 counts.

In sample 6 (4-6 cm) *Pinus* has dropped further down to 37%, whereas *Betula* stays around 30% and *Salix* increases up to 5%. *Juniperus* slightly increases (2%) while Myrica values stay constant at around 2%; NAP amount to 23%. A slight increase of total Ericaceae is observed. Among the terrestrial herbs, *Artemisia*, Cichoriaceae and *Polygonum cf. bistorta* (synonym *Bistorta officinalis*) are prominent. The Poaceae curve increases again up to 12%. One coenobium of *Pediastrum boryanum* and one pollen of *Myriophyllum spicatum* were identified among the aquatic taxa. Micro-charcoal counts further increase up to 900 particles.

The uppermost sample 7 (at 6-8 cm) is characterized by the intersection of the *Betula* and *Pinus* curves particularly. *Betula* increases up to 42%, whereas *Pinus* drops down to 28%. A further increase of heliophytes as for example of Caryophyllaceae, Rosaceae and Asteraceae as well as of *Sphagnum* is observed. Among the aquatic taxa *Typha latifolia* type is present, albeit with very low amounts. Several spores of *Ophioglossum* occur in this layer. The micro-charcoal counts slightly decrease down to 720 particles.

Discussion

As stated earlier, the pollen assemblage of the lowermost sample 4 (0-2 cm) of layer 11b (Supplementary Figure S 61).), shows great similarities regarding vegetation and environmental conditions with those of the three bulk samples 1,2 and 3 from layers 11a, 11b, and 11b$_2$ (Tab. 3, main text; Supplementary Figure S 60). They are therefore considered to be of the same depositional age. Samples 5 (2-4 cm) and 6 (4-6 cm) on the other hand reflect the slow transition from boreal woodlands into the open, grass- and heliophyte-rich steppe-tundra-like vegetation. This shift seems to be fully completed in sample 7 (6-8 cm) and also in sample 8, which already belongs to layer 10. That means that the top of layer 11b and layer 10 have to be regarded as coeval formations. Micro-charcoal counts are highest in the uppermost samples 7 and 8 pointing to burning. It remains unclear, however, whether these were natural fire events or related to human activity.

In comparison with the former Eemian/Early Weichselian pollen profile of Lichtenberg (Veil et al., 1994) (Supplementary Table S 14) and other northern German Early Weichselian key profiles (Behre et al., 2005; Behre and Lade, 1986; Caspers, 1997; Caspers and Freund, 2001; Hahne et al., 1994; Menke and Tynni, 1984), the obtained pollen spectra might be either correlated with the transition of the Brörup Interstadial into the Rederstall Stadial or the Odderade Interstadial into the Schalkholz Stadial, respectively. The main distinction between these two transitional phases is the differing amounts of the Poaceae and total NAP. Because of the relatively low amounts of Poacaeae and total NAP in our record, and taking into account the known occurrence of the heliophytic *Selaginella selaginoides* already in the Rederstall Stadial (Behre et al., 2005), we assign the samples 1 to 8 from Trench 2 to late Brörup (WE II b) transitioning into the Rederstall Stadial (WE III) (Tab. 3, main text; Supplementary Table S 14). This is in good accordance with the established lithostratigraphy and the geochronological time scale for Trench 2 (see section 5.2, main text; Supplementary Section 5.1).

7.2.3 Bulk samples of core PD.028 (9 to 12)

Results

The two lowermost bulk samples (10 and 9) of core PD.028 (530-555 cm and 465-530 cm) (Supplementary Figure S 59c and Supplementary Table S 11 for sediment description) show relatively similar pollen spectra, characterized by high *Pinus* values between 60 and 70%, wh*ereas Betula* amounts to 16% in both samples. Values of *Salix* are between 0.8% and about 3%. *Picea, Juniperus* and *Larix* occur with amounts below 1%. Pollen of heliophytic genus such as *Valeriana vulgaris*-type, *Matricari*a-type, *Artemisia*, Asteraceae and Chenopodiaceae occur. A decrease of the Poaceae from bottom (11%) to top (3%) can be observed. NAP are between 6% and 17%. A spore of cf. *Botrychium lunaria* and a few *Sphagnum* spores were found in the upper sample (9; 530-465 cm) (Supplementary Figure S 62).

The two overlying samples 11 and 12 (355-375 cm and 230-250 cm) of core PD.028 are also very similar in their qualitative and quantitative pollen composition. They are showing very high amounts of NAP (between 50 and 60%), mainly composed of Poaceae (ca. 35%). The very rich heliophytic flora includes *Artemisia*, *Valeriana montana*-type, *Matricaria*-type, *Polygonum bistorta*-type, *Helianthemum oelandicum*-type, Rosaceae, Apiaceae, Brassicaceae, Asteraceae, Chenopodiaceae and *Epilobium*. Among the arboreal pollen, *Betula* is predominant (ca. 30%), whereas *Pinus* values are between 11 and 15%. Ericaceae indeterminate, *Calluna,* *Empetrum* and *Vaccinium*-type have unambiguously increased. Characteristic for both samples are highly abundant cell colonies of the green algae *Pediastrum* (Supplementary Figure S 62). Due to preservation only two species could be determined, namely *P. boryanum* and cf. *P. kawraiskyi*, the majority of colonies is listed as *Pediastrum* indeterminate.

Discussion

Both lowermost samples (9 and 10) reflect a boreal *Pinus-Betula* forest with some *Picea, Juniperus, Larix* and a relatively diverse but not predominant heliophytic herbal flora, indicating open stands. The occurrence of *Botrychium cf. lunaria* in sample 10 points to sandy and humic open areas in the closer vicinity.

The samples 11 and 12 on the other hand reflect an open landscape with grasses and heliophytic herbs predominating. Among the wooden taxa only *Betula*, most probably *Betula nana* and very few *Salix* and *Juniperus* are part of the zonal vegetation of this severe cold phase. We assume *Pinus* pollen to be the result of long-distance transport. The occurrence of extremely large numbers of *Pediastrum* colonies points to wet local conditions. Among the *Pediastrum* species recorded, *P. kawraiskyi* is the most cold tolerant (Turner et al., 2014) with Holocene occurrences in Arctic and Antarctic environments (Komárek and Jankovská, 2001). The increase of moisture and a rise of water tables is typical for transitional phases between forested and nonforested phases due to the loss of woodland (Behre et al., 2005).

The core Veil 1 (Veil et al., 1994) taken a few meters apart from core PD.028 with a quite similar lithology (Fig. 1, main text; Supplementary Table S 11) provides a sound basis for correlation. Based on this continuous record and further data obtained by the authors, the two lowermost bulk samples of core PD.028 (samples 9 and 10) are correlated to late phases of the Odderade Interstadial (WE IVb). Regarding the two uppermost samples (11 and 12), on the premise that organic-rich deposits mostly refer to relatively temperate conditions (Hahne et al., 1994; cf. Vandenberghe and van der Plicht, 2016), we interpret these two layers to have formed during individual minor interstadials, not yet described for Northern Germany. Their position on top of the Odderade, but below the clearly cryogenic deposits, induces their ascription to early phases of the Schalkholz Stadial (WP I) (Tab. 3, main text) (cf. Antoine et al., 2016; Müller and Sánchez Goñi, 2007). This correlation is furthermore mainly based on the occurrence of high NAP, particularly Poaceae values in pollen records of the Schalkholz Stadial (Caspers and Freund, 2001; Hahne et al., 1994; Veil et al., 1994), which are not documented from the previous stadials Herning (WF I) and Rederstall (WF III). Due to sampling manner and low number of samples, the correlation and denomination remains preliminary. A future publication will provide more detail and resolution.

Section 8: Phytolith analysis

Datailed Sample preparation

Phytolith extraction according to the Rapid Phytolith Extraction method (Katz et al., 2010) required sieving the dry samples to remove particles larger than 0.5 mm. We then weighed between 30- 50 mg of sieved sediment from each sample and recorded the weight. Due to the low organic content in the samples hydrogen peroxide or dry ashing was not required. We added this to a 0.5 ml centrifuge tube and removed carbonates minerals and bones in the sediment with the addition of 50 µl of 6 N HCl with a mechanical pipette (Eppendorf Research Plus). Each tube was gently agitated to ensure the HCI fully saturated the sample. After bubbling ceased and no carbonates remained, after approximately about 30 minutes, we added 450 µl 2.4 g/ml sodium polytungstate solution (SPT, Na_6 ($H_2W_{12}O_{40}$) H_2O). The samples were then agitated for 1 minute, and then sonicated (Elma E-One) for ten minutes and then centrifuged for 10 min at 5000 rpm (Eppendorf Centrifuge 5424). The phytolith-rich supernatant was transferred to a new 0.5 ml centrifuge tube and agitated for 1 minute. An aliquot of 50 µl was then pipetted onto a slide and covered with a 24 mm x 24 mm coverslip. Phytoliths were counted at 200 -400x magnification (0.95) using a field count method with a transmitted light microscope (Axio scope A1, Zeiss).

For calculating phytolith concentrations, 100 mg of dry sediment was weighed and then heated in crucibles at 500 °C for 5 min in a muffle oven to remove organic material. After cooling, we transferred the sample to 2 ml Eppendorf tubes, and then added 100 µl of 1 N HCl. The samples were then centrifuged at 6000 rpm for 5 minutes. The supernatant was discarded, and the samples were washed twice. The samples were then dried over a few days and then weighed in the Eppendorf tubes.

Additional discussion

Quantifications of the phytolith assemblage established that the concentrations of phytoliths per gram of sediment and per gram of acid-insoluble sediment are mainly similar between different samples. Similarity indicates that intra samples comparison is not distorted by large amounts of carbonates or organic material in particular samples that would misleadingly inflate phytoliths per gram of sediment (Karkanas et al., 2000). The phytolith assemblages exhibit low densities (< 70,000 phytoliths/gram, see Supplementary Tables S15, S16, S17) and have large amounts of weathered and indeterminate phytoliths. The assemblages are nearly entirely composed of single-cell morphologies. The most common morphotypes were derived from monocot plants, including parallelepiped elongate thin psilates, parallelepiped elongate thin sinuates, rondels and indeterminate short-cells. These types are either diagnostic of grasses or occur in grasses. Phytoliths diagnostic of non-grass type monocots such as sedges or reedmaces were not evident. Although highly rare, a small number of multi-cell forms occurred including parallelepiped elongate thin psilates. Phytoliths associated with eudicots were found in all samples. These included leaf types such as eudicot-type hairs, hair bases, jigsaws, tracheids (cylindric sulcates), and multi-cell polyhedral. Unfortunately diagnostic types of specific genera were absent. Wood/bark types include spheroid, discoid and ellipsoid types were much rare, but this reflects the small numbers produced by these plants. Phytolith associated with burning with color or melting damage was not evident. Monoaxon sponge spicules were found in MH3 and MH5. Diatoms were present in one sample but were too damaged to identify beyond showing a pennate form (MH4). Occasional starches were observed in some samples but they were attributed to contamination and not counted.

The nature of the assemblage suggests it is probable that some morphologies such as dendritics, sedge cones, and plates may be disproportionately damaged and lost from the assemblage due to taphonomic processes. These patterns and the limited sample size prevent detailed vegetation reconstruction on-site For example, the assemblages are too limited to apply bulliform cell, anatomical-based aridity or forest cover indexes. However, they do provide a broad environmental picture and this overall picture is consistent with sedimentation processes at open-air sites (Wroth et al., 2019). Although several samples are relatively similar, phytolith variation does show diachronic patterning in plant assemblages. For example, the earliest sample from layer 7 had low numbers (~8,000 phytoliths/g), both in terms of phytoliths of 1 g of sediment and phytoliths in 1 g of AIF, there are much higher numbers associated with the browner-colored layer 11a (<60,000 phytoliths/g). Later layers (layer 8 and 9) were more similar to layer 7. This indicates that layer 11a was formed during distinct, warmer and more plant rich conditions.

References

Altermann, M., Jäger, K.-D., Kopp, D., Kowalkowski, A., Kühn, D., Schwanecke, W., 2008. Zur Kennzeichnung und Gliederung von periglaziär bedingten Differenzierungen in der Pedosphäre - On characteristics and subdivision of pedospheric differentiations due to previous periglacial conditions. Waldökologie, Landschaftsforsch. und Naturschutz 6, 5-42 (German with english abstract and captions).

Antoine, P., Coutard, S., Guerin, G., Deschodt, L., Goval, E., Locht, J.-L., Paris, C., 2016. Upper Pleistocene loess-palaeosol records from Northern France in the European context: Environmental background and dating of the Middle Palaeolithic. Quat. Int. 411, 4–24. https://doi.org/10.1016/j.quaint.2015.11.036

Arnold, L.J., Demuro, M., Parés, J.M., Pérez-González, A., Arsuaga, J.L., Bermúdez de Castro, J.M., Carbonell, E., 2015. Evaluating the suitability of extended-range luminescence dating techniques over early and Middle Pleistocene timescales: Published datasets and case studies from Atapuerca, Spain. Quat. Int. 389, 167–190. https://doi.org/10.1016/j.quaint.2014.08.010

Behre, K.-E., Hölzer, A., Lemdahl, G., 2005. Botanical macro-remains and insects from the Eemian and Weichselian site of Oerel (northwest Germany) and their evidence for the history of climate. Veg. Hist. Archaeobot. 14, 31–53. https://doi.org/10.1007/s00334-005-0059-x

Behre, K.-E., Lade, U., 1986. Eine Folge von Eem und 4 Weichsel-Interstadialen in Oerel/Niedersachsen und ihr Vegetationsablauf. E&G Quat. Sci. J. 36, 11–36. https://doi.org/10.3285/eg.36.1.02

Beug, H.-J., 2004. Leitfaden der Pollenbestimmung für Mitteleuropa und angrenzende Gebiete. Germania 87, 542.

Bouma, J., Foc, C.A., Miedma, R., 1990. Micromorphology of Hydromorphic Soils: Applications for Soil Genesis and Land Evaluation, in: Douglas, L.A. (Ed.), Soil Micro-Morphology: A Basic and Applied Science. pp. 257–278.

Bridge, J., Demicco, R., 2008. Earth Surface Processes, Landforms and Sediment Deposits. Cambridge University Press, New York.

Buylaert, J.P., Jain, M., Murray, A.S., Thomsen, K.J., Thiel, C., Sohbati, R., 2012. A robust feldspar luminescence dating method for Middle and Late Pleistocene sediments. Boreas

41, 435–451. https://doi.org/10.1111/j.1502-3885.2012.00248.x

Caspers, G., 1997. Die eem- und weichselzeitliche Hohlform von Groß Todtshorn (Kr. Harburg; Niedersachsen) - Geologische und palynologische Untersuchungen zu Vegetation und Klimaverlauf der letzten Kaltzeit. Schriftenr. der Dtsch. Geol. Gesellschaft 4, 7–59.

Caspers, G., Freund, H., 2001. Vegetation and climate in the Early- and Pleni-Weichselian in northern Central Europe. J. Quat. Sci. 16, 31–48. https://doi.org/10.1002/1099-1417(200101)16:1<31::AID-JQS577>3.0.CO;2-3

Cheng, H., He, J., Zou, X., Li, J., Liu, C., Liu, B., Zhang, C., Wu, Y., Kang, L., 2015. Characteristics of particle size for creeping and saltating sand grains in aeolian transport. Sedimentology 62, 1497–1511. https://doi.org/10.1111/sed.12191

Christiansen, Hanne Hvidtfeldt, 1998a. Periglacial sediments in an Eemian-Weichselian succession at Emmerlev Klev, southwestern Jutland, Denmark. Palaeogeogr. Palaeoclimatol. Palaeoecol. 138, 245–258. https://doi.org/10.1016/S0031-0182(97)00117-X

Christiansen, Hanne H., 1998. ‘Little Ice Age’ nivation activity in northeast Greenland. The Holocene 8, 719–728. https://doi.org/10.1191/095968398666994797

Christiansen, Hanne Hvidtfeldt, 1998b. Nivation forms and processes in unconsolidated sediments, NE Greenland. Earth Surf. Process. Landforms 23, 751–760. https://doi.org/10.1002/(SICI)1096-9837(199808)23:8<751::AID-ESP886>3.0.CO;2-A

Cohen, A.S., 2003. Paleolimnology: the history and evolution of lake systems. Oxford University Press.

Cornell, R.M., Schwertmann, U., 2003. The Iron Oxides, 2nd ed. WILEY-VCH, Weinheim. https://doi.org/10.1002/3527602097

Cunningham, A.C., Wallinga, J., 2012. Realizing the potential of fluvial archives using robust OSL chronologies. Quat. Geochronol. 12, 98–106. https://doi.org/10.1016/j.quageo.2012.05.007

Dietze, M., Kreutzer, S., Burow, C., Fuchs, M.C., Fischer, M., Schmidt, C., 2016. The abanico plot: Visualising chronometric data with individual standard errors. Quat. Geochronol. 31, 12–18. https://doi.org/10.1016/j.quageo.2015.09.003

Dobrowolski, R., Bałaga, K., Bogucki, A., Fedorowicz, S., Melke, J., Pazdur, A., Zubovič, S., 2001. Chronostratigraphy of the okunin and Czerepacha Lake-mire geosystems (Volhynia polesiye, NW Ukraine) during the Late Glacial and Holocene. Geochronometria 20, 107–115.

Faegri, K., Iversen, J., Kaland, P.E., Krzywinski, K., 1989. Textbook of pollen analysis, 4th ed. John Wiley & Sons Ltd., Chichester.

Farrell, E.J., Sherman, D.J., Ellis, J.T., Li, B., 2012. Vertical distribution of grain size for wind blown sand. Aeolian Res. 7, 51–61. https://doi.org/10.1016/j.aeolia.2012.03.003

Fedoroff, N., Courty, M.-A., Guo, Z., 2010. Palaeosoils and Relict Soils, in: Stoops, G., Marcelino, V., Mees, F. (Eds.), Interpretation of Micromorphological Features of Soils and Regoliths. Elsevier, pp. 623–662. https://doi.org/10.1016/B978-0-444-53156-8.00027-1

Fränzle, O., 1988. Glaziäre, periglaziäre und marine Reliefentwicklung im nördlichen Schleswig-Holstein. Schr. Naturwiss. Ver. Schlesw.-Holst. 58, 1–30.

Galbraith, R.F., Roberts, R.G., 2012. Statistical aspects of equivalent dose and error calculation and display in OSL dating: An overview and some recommendations. Quat. Geochronol. 11, 1–27. https://doi.org/10.1016/j.quageo.2012.04.020

Grimmel, E., 1973. Bemerkungen zum Geschiebedecksand. E&G – Quat. Sci. JournalG Quat. Sci. J. 23/24, 16–25. https://doi.org/10.3285/eg.23-24.1.02

Guérin, G., Mercier, N., Adamiec, G., 2011. Dose-rate conversion factors: update. Anc. TL 29, 5–8.

Hahne, J., Kemle, S., Merkt, J., Meyer, K.D., 1994. Eem-, weichsel- und saalezeitliche Ablagerungen der Bohrung “Quakenbrück GE 2.” Geol. Jahrb. A134, 9–69.

Hein, M., Urban, B., Tanner, D.C., Buness, A.H., Tucci, M., Hoelzmann, P., Dietel, S., Kaniecki, M., Schultz, J., Kasper, T., Suchodoletz, H., Schwalb, A., Weiss, M., Lauer, T., 2021. Eemian landscape response to climatic shifts and evidence for northerly Neanderthal occupation at a palaeolake margin in Northern Germany. Earth Surf. Process. Landforms esp.5219. https://doi.org/10.1002/esp.5219

Huntley, D.J.; Baril, M.R., 1997. The K content of the K-feldspars being measured in optical dating or thermoluminescence dating. Anc. TL 15, 11–13.

Huntley, D.J., Lamothe, M., 2001. Ubiquity of anomalous fading in K-feldspars and the measurement and correction for it in optical dating. Can. J. Earth Sci. 38, 1093–1106. https://doi.org/10.1139/cjes-38-7-1093

Karkanas, P., Bar-Yosef, O., Goldberg, P., Weiner, S., 2000. Diagenesis in Prehistoric Caves: the Use of Minerals that Form In Situ to Assess the Completeness of the Archaeological Record. J. Archaeol. Sci. 27, 915–929. https://doi.org/10.1006/jasc.1999.0506

Komárek, J., Jankovská, V., 2001. Review of the Green Algal Genus Pediastrum; Implication for Pollenanalytical Research. Bibl. Phycol. 108, 1–127.

Kreutzer, S., Burow, S., Dietze, M., Fuchs, M.C., Schmidt, C., Fischer, M., Friedrich, J., 2020. Luminescence: Comprehensive Luminescence Dating Data Analysis.

Kreutzer, S., Schmidt, C., Dewitt, R., Fuchs, M., 2014. The a-value of polymineral fine grain samples measured with the post-IR IRSL protocol. Radiat. Meas. 69, 18–29. https://doi.org/10.1016/j.radmeas.2014.04.027

Lade, U., Hagedorn, H., 1982. Sedimente und Relief einer eiszeitlichen Hohlform bei Krempel (Elbe-Weser-Dreieck). E&G Quat. Sci. J. 32, 93–108. https://doi.org/10.3285/eg.32.1.08

Mania, D., Toepfer, V., 1973. Königsaue: Gliederung, Oekologie und Mittelpaläolithische Funde der letzten Eiszeit. Veröffentlichungen des Landesmuseums für Vorgeschichte in Halle 26, Deutscher Verlag der Wissenschaften, Berlin.

Menke, B., 1976. Neue Ergebnisse zur Stratigraphie und Landschaftsentwicklung im Jungpleistozän Westholsteins. E&G Quat. Sci. J. 27, 53–68. https://doi.org/10.3285/eg.27.1.05

Menke, B., Tynni, R., 1984. Das Eeminterglazial und das Weichselfrühglazial von Rederstall/Dithmarschen und ihre Bedeutung für die mitteleuropäische Jungpleistozän-Gliederung . Geol. Jahrb. A 76, 1–120.

Moore, P.D., Webb, J.A., Collison, M.E., 1991. Pollen analysis. Blackwell Scientific Publications, Oxford.

Müller, U.C., Sánchez Goñi, M.F., 2007. Vegetation dynamics in southern Germany during marine isotope stage 5 (~ 130 to 70 kyr ago), in: Sirocko, F., Claussen, M., Sánchez Goñi, M.F., Litt, T. (Eds.), The Climate of Past Interglacials. (Developments in

Quaternary Sciences 7). pp. 277–287. https://doi.org/10.1016/S1571-0866(07)80044-3

Prescott, J.R., Hutton, J.T., 1994. Cosmic ray contributions to dose rates for luminescence and ESR dating: Large depths and long-term time variations. Radiat. Meas. 23, 497–500. https://doi.org/10.1016/1350-4487(94)90086-8

Richter, H., Haase, G., Lieberoth, I., 1970. Periglazial-Löß-Paläolithikum im Jungpleistozän der Deutschen Demokratischen Republik (Petermanns Geogr. Mitt. Ergänzungsheft Nr. 274). VEB Hermann Haack, Gotha.

Schwan, J., 1988. The structure and genesis of Weichselian to early hologene aeolian sand sheets in western Europe. Sediment. Geol. 55, 197–232. https://doi.org/10.1016/0037-0738(88)90132-7

Semmel, A., Terhorst, B., 2010. The concept of the Pleistocene periglacial cover beds in central Europe: A review. Quat. Int. 222, 120–128. https://doi.org/10.1016/j.quaint.2010.03.010

Taylor, G.H., Teichmüller, M., Davis, A., Diessel, C.F.K., Littke, R., Robert, P., 1998. Organic Petrology. Gebrüder Bornträger, Berlin Stuttgart.

Thiel, C., Buylaert, J.P., Murray, A., Terhorst, B., Hofer, I., Tsukamoto, S., Frechen, M., 2011. Luminescence dating of the Stratzing loess profile (Austria) - Testing the potential of an elevated temperature post-IR IRSL protocol. Quat. Int. 234, 23–31. https://doi.org/10.1016/j.quaint.2010.05.018

Thomsen, K.J., Murray, A.S., Jain, M., Bøtter-Jensen, L., 2008. Laboratory fading rates of various luminescence signals from feldspar-rich sediment extracts. Radiat. Meas. 43, 1474–1486. https://doi.org/10.1016/j.radmeas.2008.06.002

Turner, F., Pott, R., Schwarz, A., Schwalb, A., 2014. Response of Pediastrum in German floodplain lakes to Late Glacial climate changes. J. Paleolimnol. 52, 293–310. https://doi.org/10.1007/s10933-014-9794-2

Van Huissteden, J. (Ko., Vandenberghe, J., Van der Hammen, T., Laan, W., 2000. Fluvial and aeolian interaction under permafrost conditions: Weichselian Late Pleniglacial, Twente, eastern Netherlands. CATENA 40, 307–321. https://doi.org/10.1016/S0341-8162(00)00085-0

Vandenberghe, J., 1992. Periglacial phenomena and pleistocene environmental conditions in the Netherlands—An overview. Permafr. Periglac. Process. 3, 363–374. https://doi.org/10.1002/ppp.3430030410

Vandenberghe, J., van der Plicht, J., 2016. The age of the Hengelo interstadial revisited. Quat. Geochronol. 32, 21–28. https://doi.org/10.1016/j.quageo.2015.12.004

Veil, S., Breest, K., Höfle, H.-C., Meyer, H.-H., Plisson, H., Urban-Küttel, B., Wagner, G.A., Zöller, L., 1994. Ein mittelpaläolithischer Fundplatz aus der Weichsel-Kaltzeit bei Lichtenberg, Lkr. Lüchow-Dannenberg. Germania 72, 1–66.

Wroth, K., Cabanes, D., Marston, J.M., Aldeias, V., Sandgathe, D., Turq, A., Goldberg, P., Dibble, H.L., 2019. Neanderthal plant use and pyrotechnology: phytolith analysis from Roc de Marsal, France. Archaeol. Anthropol. Sci. 11, 4325–4346. https://doi.org/10.1007/s12520-019-00793-9

Zagwijn, W., Paepe, R., 1968. Die Stratigraphie der weichselzeitlichen Ablagerungen der Niederlande und Belgiens. E&G – Quat. Sci. J. 19, 10–31.

Figures and Tables

Supplementary Table S 11. Stratigraphic description of core PD.028 and correlation with the stratigraphic layers of Trench 1 and 2. For a picture of the core, see Supplementary Figure S 59.

Depth [cm]	Properties	Layer	CO_3	Munsell-Colour
0-30	Ploughing horizon, medium humic, silty medium to coarse sand, 10% gravel content	1	-	10YR 3/4
30-50	Bw-horizon, glacial cover sand (*Geschiebedecksand*), loamy medium sand, 10% gravel content, unbedded	2	-	10YR 5/7
50-120	crudely to unbedded silt and fine to coarse sand, varying gravel contents (10 to 50%), varying hydromorphic features	7', 3	-	10YR 8/2 - 10YR 5/7
120-175	Alternating well to crudely bedded medium sand, gravel content <1%	4, 5	-	10YR 7/5
175-200	Precipitation of ferrihydrite in unbedded yellowish medium sand and precipitation of lepidocrocite in thin (5cm) whitish (5Y 7/2) fine-sandy silt (multi-phased soil formation?), gravel content <1%	6, 7	-	10YR 4/4 - 2.5YR 6/4 - 10YR 5/8
200-215	Bore detritus	-	-	-
215-230	Wavy, thin-bedded, slightly silty fine to medium sand, <1% gravel	9	-	7/5GY
230-250	Peaty mud, 20% medium to coarse sand, no plant remains, lower boundary humic sand alternating with subjacent stratum	9	-	2.5Y 2.5/1- 2.5Y 3/2
250-325	Weak wavy thin bedded coarsening-up sequence of fine sands to gravelly (5%) medium sands	9	-	5Y 7/1 - 5Y 7/3
325-355	Same as above, alternating with thin, redeposited humic beds, lepidocrocite precipitation on top, bore detritus between 300 and 310 cm	9	-	2.5YR 3/2- 2.5YR 7/8
355-390	Strongly humiferous fine to medium sand, humic content gradually decreasing to the bottom	9		2.5 YR 3/2
390-465	Medium to fine sands, interbedded with thin humic layers, grading into very slightly humic, silty fine sands, bore detritus between 400 and 425 cm	9		2.5YR 6/2- 5/5BG
465-555	Peat, upper part (ca. 465-530 cm): weakly decomposed, plant remains; lower part (530-555 cm): strongly decomposed, no plant remains, gradual lower boundary; between 500 and 510 cm bore detritus or intercalation of overlying stratum	9(?)	-	2.5Y 3/2- 2.5Y 2.5/1
555-600	Well-bedded, very silty fine to medium sands, slightly to medium humic	10(?)	-	5Y 4/1

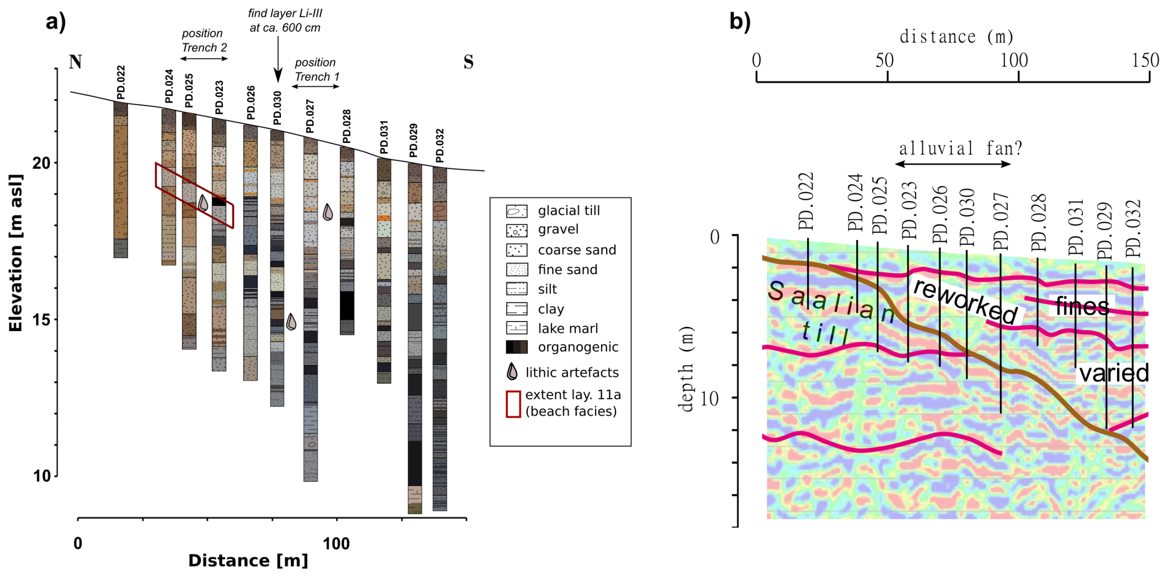

Supplementary Figure S 49. a) Section of the coring transect (Hein et al., 2021) with the position of the find layers Li-I to Li-III indicated by artefact symbols and arrows. The extent of the beach sand (layer 11a) is highlighted with a red box. b) Section of the seismic profile (Hein et al., 2021) with interpretation. The segment between core PD.025 (in the north) and PD.028 (in the south) is poorly stratified, classified as "reworked" and interpreted to represent a small alluvial fan, hosting the occupational sites.

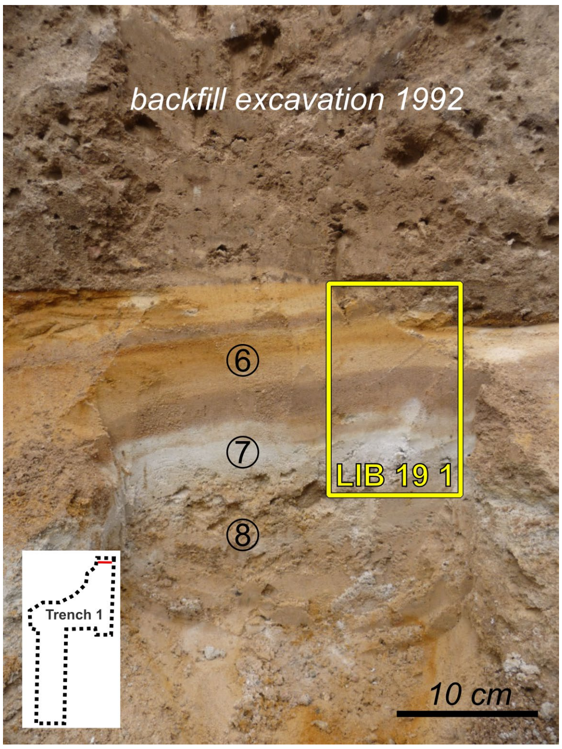

Supplementary Figure S 50. Location of the block sample, from which LIB 19 1 was produced at the northern profile of Trench 1 (indicated by red line in the insert). This block sample captures the contact of layer 6 and 7 as well as the overlying refill from the 1992 excavation of the site.

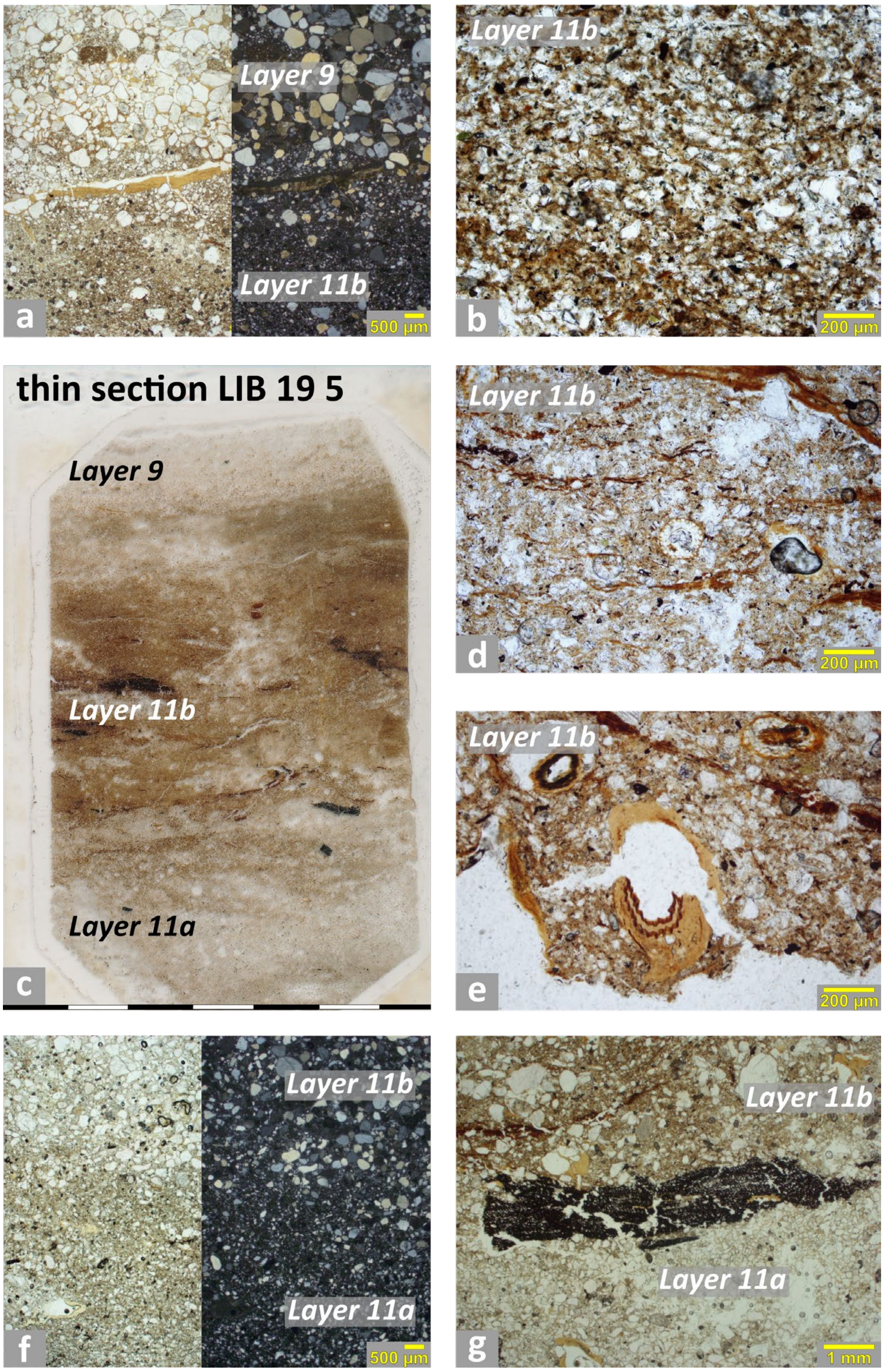

Supplementary Figure S 51. Thin section and microphotographs of sample LIB 19 5 containing layer 11a (humic sand), overlain by 11b (peat/mud) and layer 9 (Niveo-fluvial sand). (a) Contact of layer 11b with layer 9, showing a difference in grain size and organic content. Note also the clay infilling of a channel here. PPL (left) and XPL (right), scale 500 µm. (b) The upper part of layer 11b is dominated by fine, detrial organics. PPL, 200 µm. (c) Scan of thin section LIB 19 5 showing a clear contact between layers 10, 11a and 11b. Note also the upper, more greyish part in layer 11b. Scale in cm. (d) The central part of layer 11b is organic-rich and elongated plant tissues are aligned horizontally. PPL, 200 µm. (e) Plant residue, roots and clay illuviation in layer 11b. PPL, 200 µm. (f) Contact between layers 11a and 11b showing different grain size, the upper layer 11b is coarser grained than the lower layer 11a. PPL (left) and XPL (right), scale 500 µm. (g) A charcoal fragment at the contact of layer 11b with 11a. Note also the increase in organic content in layer 11b compared to layer 11a. PPL, scale 1 mm.

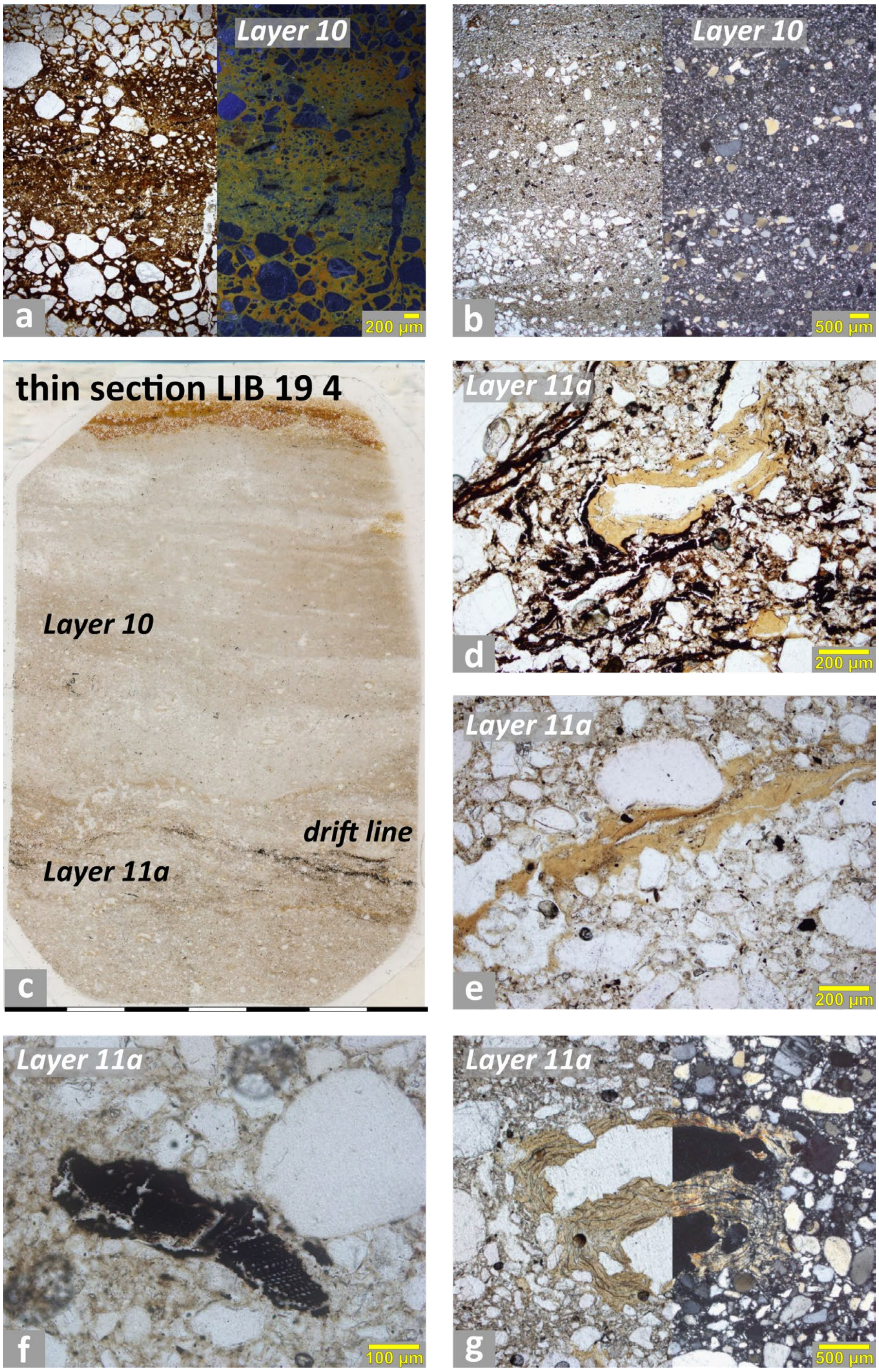

Supplementary Figure S 52. Thin section and microphotographs of sample LIB 19 4 containing layer 11a (humic sand) with find horizon Li-II on top and overlain by layer 10 (clayey silt). (a) The top of layer 10 is here overprinted with iron. PPL (left) and OIL (right), scale 200µm. (b) Layer 10 shows graded bedding. PPL (left) and XPL (right), scale 500 µm. (c) Thin section scan of LIB 19 4 showing humic bands in layer 11a and a gradual contact with layer 10. Scale in cm (d) Layer 11a is enriched in organic materials that are often humified. Note also the yellow clay coating in a void at the center of the photo. PPL scale, 200 µm. (e) A channel refilled with clay in layer 11a. PPL, 200 µm. (f) A charcoal fragment in layer 11a. PPL, 100 µm. (g) Clay illuviation in layer 11a often has a weathered/degraded appearance. PPL (left) and XPL (right), 200 µm.

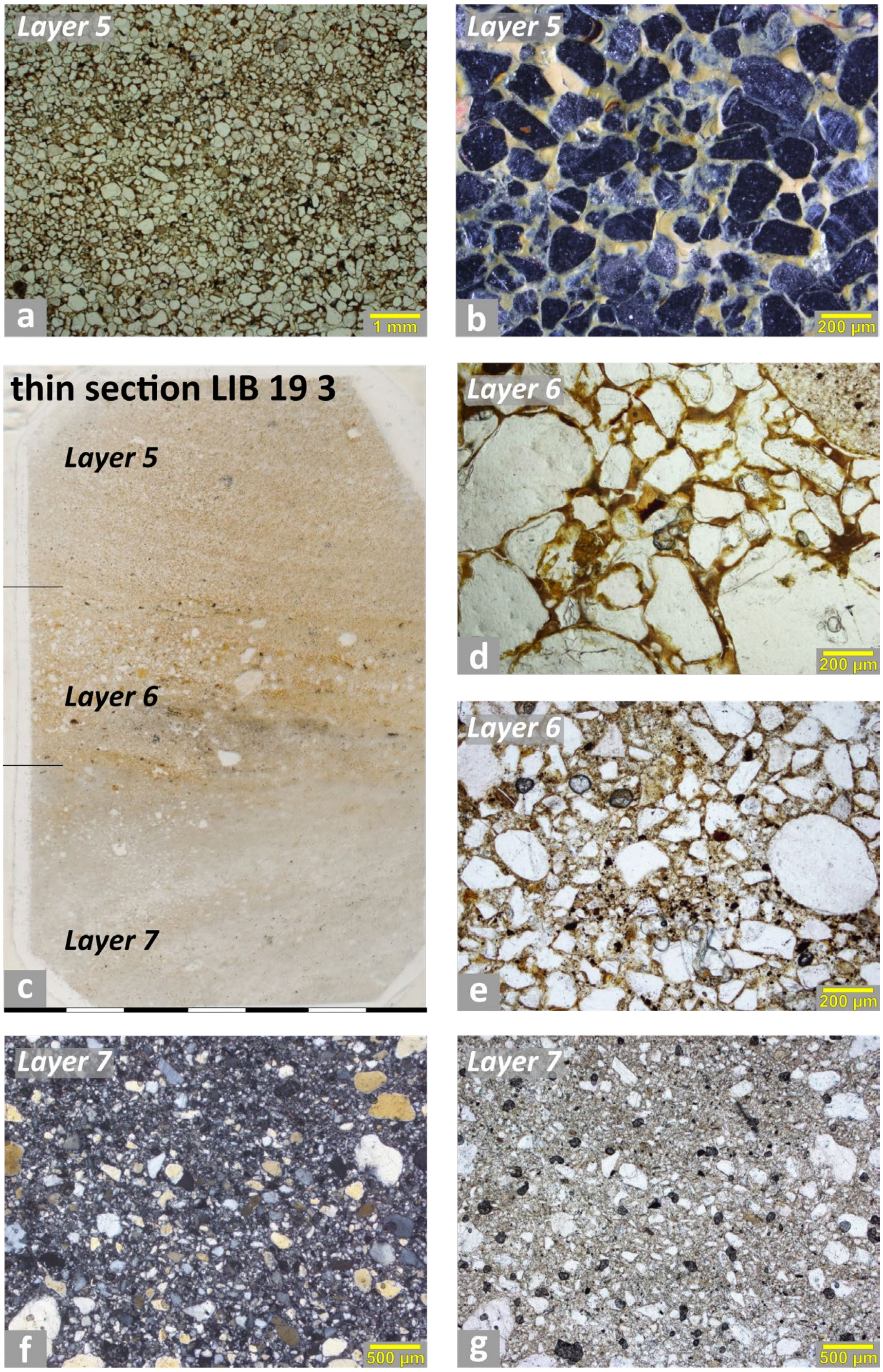

Supplementary Figure S 53. Thin section and microphotographs of sample LIB 19 3 containing the find horizon Li-I in layer 7 (silty fS) and the overlying layer 6 (orange fS) and layer 5 (eolian sand). (a) Layer 5 is mainly composed of silt to coarse sand sized, rounded quartz grains, but it is also poorly sorted for medium sized sand and also expresses weak bedding. PPL, Scale 1 mm. (b) The packing voids are filled with clay illuviation, which shows weak iron and organic staining. OIL, 200 µm. (c) Thin section showing the clear contact of layer 7 with layer 6, but a gradual contact of layer 6 with layer 5. Note also that layer 6 is here composed of two subunits showing different color expressions, more greyish in the lower opposed to orange in the upper part. Scale in cm. (d) Iron stained clay illuviation in layer 6, similar as in the other thin sections of this layer, but also similar to the overlying layer 5. PPL, scale 200 µm. (e) The lower subunit of layer 6 is enriched in amorphous organic fine material, explaining the color difference between the two subunits. (f & g). Layer 7 has a typical expression here with densely packed silt to coarse sand sized quartz and a poor sorting for fine sized material. XPL (f) and PPL (g), scale 500 µm.

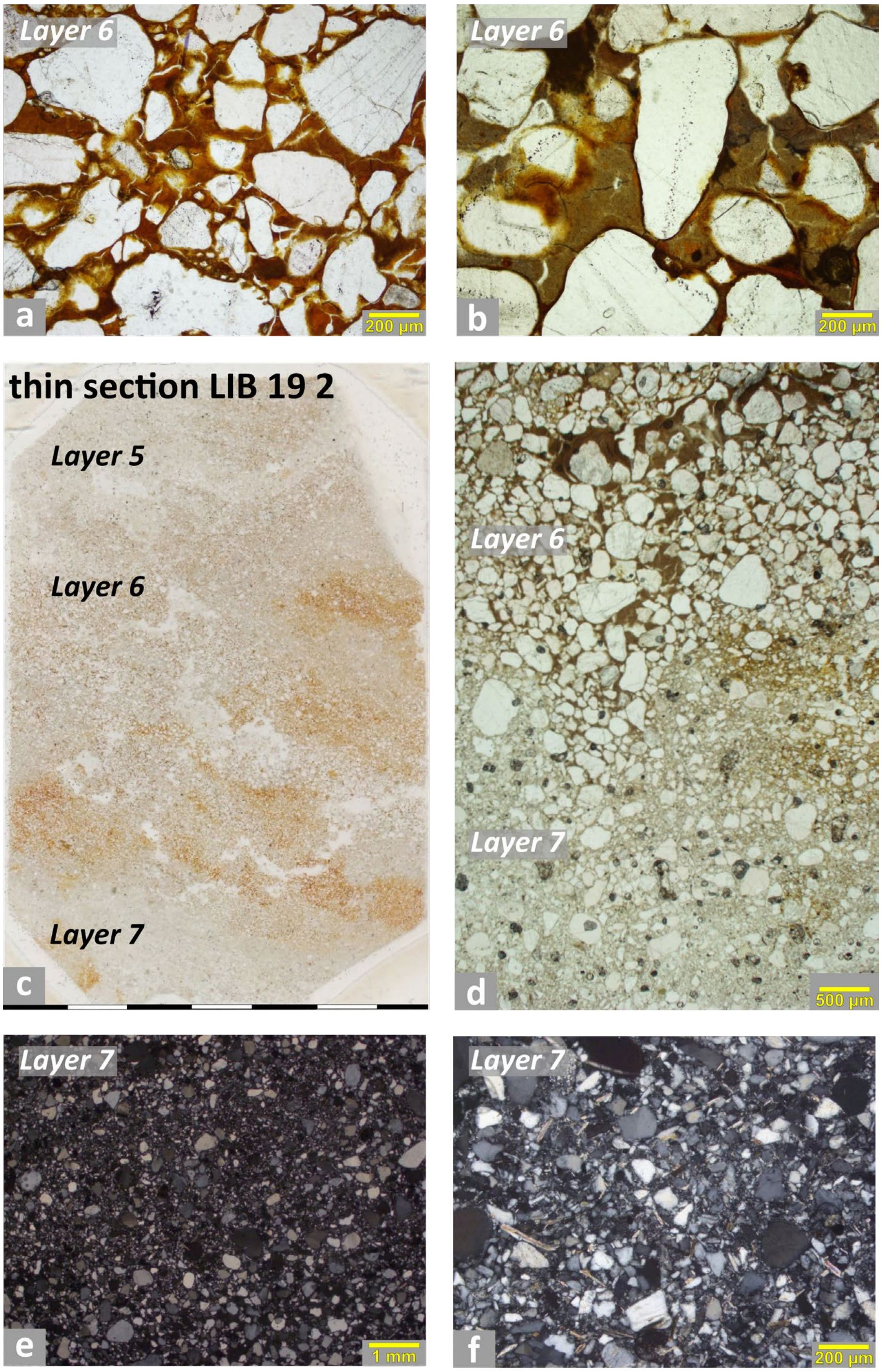

Supplementary Figure S 54. Thin section and microphotographs of sample LIB 19 2 containing the find horizon Li-I in layer 7 (silty fS) as well as overlying layer 6 (orange fS) and layer 5 (eolian sand). (a) Iron stained clay coatings and infillings in layer 6. PPL, 200 µm. (b) Here, the clay coatings are only locally iron stained (red) and are otherwise greyish-yellowish or show black amorphous staining. PPL, 200 µm. (c) This local variation in iron staining of the clay coatings is resulting in a mottled appearance of layer 6 in thin section. Note also the clear contact with the underlying layer 7. Scale in cm. (d) The contact between layer 6 and 7 is characterized by a change in grain size, layer 6 is coarser grained than layer 7. PPL, 500 µm. (e & f) Layer 6 at different magnifications (scale 1 mm in e and 200 µm in f) showing a very dense microstructure with a poor sorting for silt and fine sand. Note also the presence of mica. Both XPL.

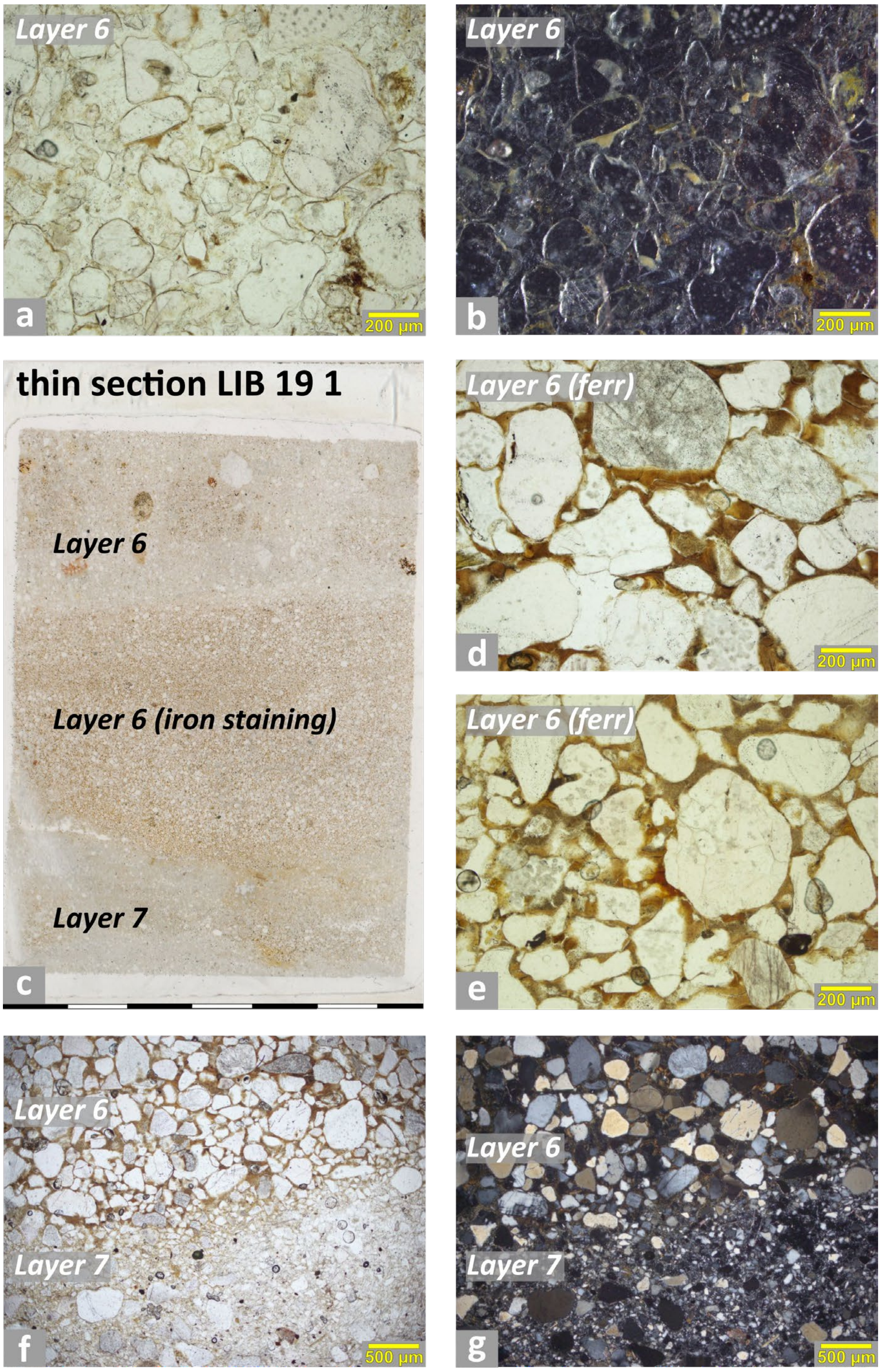

Supplementary Figure S 55. Thin section and microphotographs of sample LIB 19 1 containing the find horizon Li-I in layer 7 (silty fS) and the overlying layer 6 (orange fS). (a) Layer 5 is mainly composed of silty to coarse sand sized quartz grains with simple packing voids. PPL, scale 200 µm. (b) Fine material in the layer 5 consists of iron stained fine organics and clay OIL, 200 µm. (c) Thin section LIB 19 1 showing clear contact between the three layers and color differences. Scale in cm. (d) The darker color in the orange sand results from iron stained clay coatings. Note the similarity in grain size between layers 5 and 6. PPL 200 µm. (e) There is variability in the clay coatings with some exhibiting a lighter, more greyish color. PPL, 200 µm. (f & g) Clear contact between layers 6 and 7 (F in PPL, G in XPL). Note the clear difference in grain size, the underlying layer 7 is sorted for silt and fine sand, while coarse grains are rare. Layer 7 also lacks the clay coatings characteristic of layer 6. Layer 7 is very dense and shows limited void space in the form of simple packing voids.

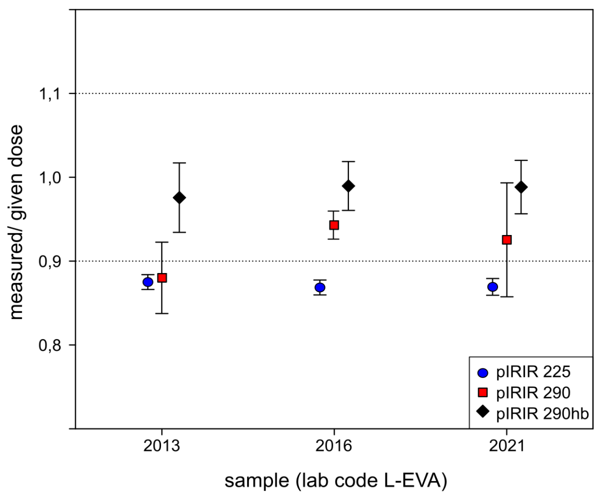

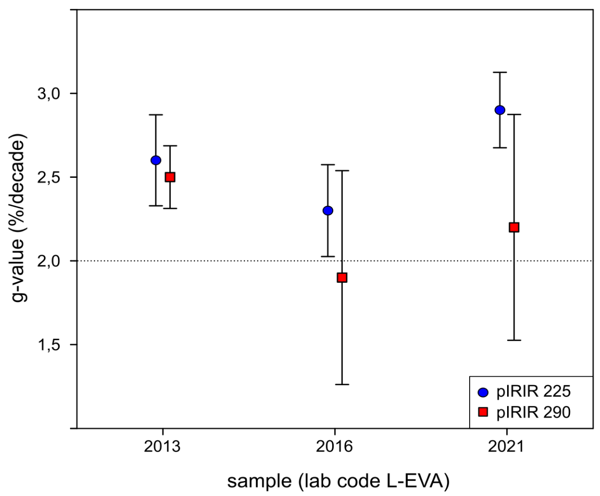

Supplementary Figure S 56. Results of the dose recovery (left) and anomalous fading (right) experiments using different elevated temperatures for the feldspar SAR protocol. For dose recovery testing, the residual signal was subtracted from the measured dose. For the chosen signal $pIRIR_{290}$ (with hotbleach, which is not relevant for the fading test), the mean measured-to-given dose ratio was 0.98 and the mean g-value was 2.2 %/decade.

Supplementary Table S 12. Measurement steps of the applied $pIRIR_{290}$ protocol

Step	Treatment
1	Dose
2	Preheat (320°C for 60s)
3	IRSL, 100s at 50°C
4	IRSL, 200s at 290°C → L_x
5	Test dose
6	Preheat (320°C for 60s)
7	IRSL, 100s at 50°C
8	IRSL, 200s at 290°C → T_x
9	IRSL, 100s at 325°C → hot bleach
10	Return to step 1

Supplementary Table S 13. Results of the high-resolution germanium gamma spectrometry, cosmic and total dose rates as well as water contents used for correction

Lab.-ID (L-EVA)	U (ppm)	Th (ppm)	K (%)	Cosmic Dose (Gy/ka)	DR_{total} (Gy/ka)	H_2O (%)
2010	1.49 ± 0.23	4.90 ± 0.40	1.24 ± 0.10	0.19 ± 0.02	2.46 ± 0.21	11.92 ± 10
2012	0.50 ± 0.10	1.80 ± 0.10	0.73 ± 0.08	0.18 ± 0.02	1.57 ± 0.20	12.90 ± 10
2014	1.50 ± 0.20	4.00 ± 0.30	1.06 ± 0.11	0.18 ± 0.02	2.25 ± 0.21	11.36 ± 10
2015	1.47 ± 0.20	4.10 ± 0.30	1.26 ± 0.10	0.18 ± 0.02	2.44 ± 0.21	10.19 ± 10
2016	1.28 ± 0.22	2.55 ± 0.18	0.98 ± 0.10	0.17 ± 0.02	2.00 ± 0.21	12.56 ± 10
2017	0.97 ± 0.17	3.57 ± 0.24	1.01 ± 0.07	0.18 ± 0.02	2.03 ± 0.20	13.25 ± 10
2018	1.06 ± 0.19	3.00 ± 0.20	0.85 ± 0.06	0.16 ± 0.02	1.88 ± 0.20	11.94 ± 10
2019	0.73 ± 0.18	1.68 ± 0.13	0.74 ± 0.08	0.18 ± 0.02	1.63 ± 0.20	11.77 ± 10
2022	3.90 ± 0.40	4.90 ± 0.30	1.11 ± 0.08	0.16 ± 0.02	2.78 ± 0.21	13.59 ± 10
2023	1.79 ± 0.24	4.60 ± 0.30	1.09 ± 0.11	0.16 ± 0.02	2.30 ± 0.20	14.77 ± 10
2024	3.50 ± 0.40	5.10 ± 0.30	1.17 ± 0.07	0.15 ± 0.02	2.69 ± 0.20	11.46 ± 10

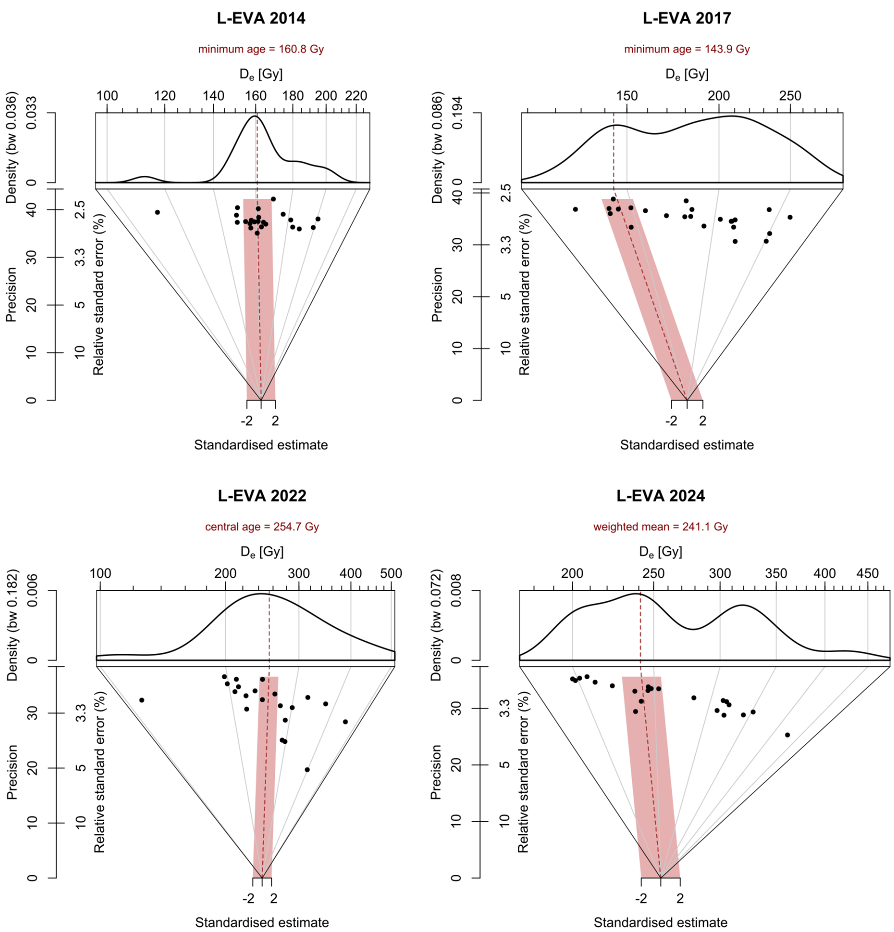

Supplementary Figure S 57. D_e-distributions of selected samples using Abanico plots. L-EVA 2014 and 2017 represent find horizon Li-I (stratigraphic layer 7); L-EVA 2022 and 2024 were taken from find-layer Li-II (stratigraphic layer 11a). Compare final ages in Tab. 2 main text.

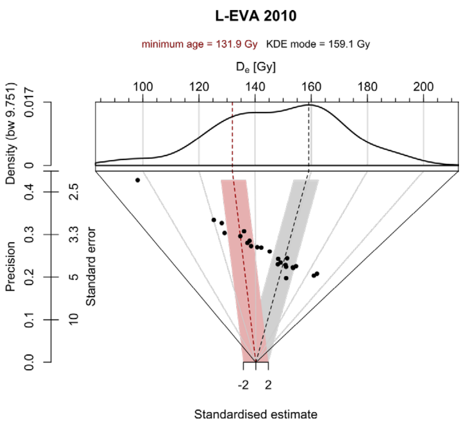

Supplementary Figure S 58. Abanico plot of the D_e-distribution of L-EVA 2010 (cryoturbated find horizon Li-I, stratigraphic layer 7'). The final D_e-estimation (applying the MAM) is indicated in red and equates a cryoturbational age of 53.5 ± 4.9 ka. For comparison, the main mode of the Kernel Density Estimation (KDE) is presented (grey bar and black dashed line). It relates to a distinct cluster in the radial plot and corresponds with a calculated age of 64.6 ± 5.8 ka, which is closer to the depositional age of this layer (see section 5.1, main text).

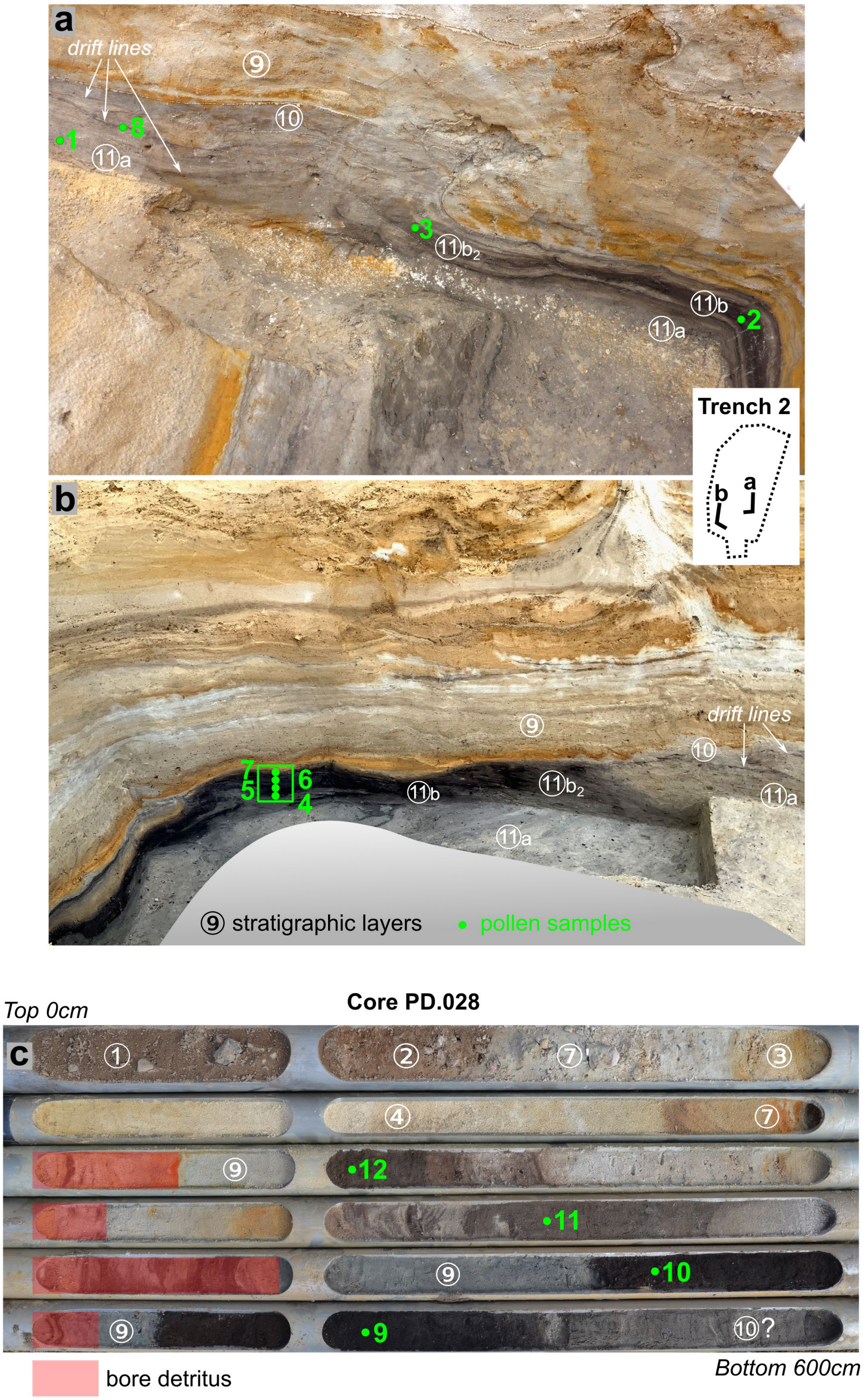

Supplementary Figure S 59. Detailed pollen sampling positions and sample codes in Trench 2 (a, b) and core PD.028 (c). Sample 8 taken from the drift line within layer 10. Lithological descriptions can be found in Supplementary Section 5.1 and Supplementary Table S 11.

Supplementary Table S 14. Summary of palynological results compared to core Veil 1 (Veil et al., 1994, Fig. 1 in the main text) and biostratigraphic subdivision. NAP = non-arboreal-pollen (terrestrial herbs and grasses); E = Eemian (pollen zone in brackets); WE = Early Weichselian, WP = Weichselian Pleniglacial.+

Lichtenberg core Veil 1 **(Veil et al., 1994)**		**Lichtenberg excavations trench2** **(2019 and 2020)**	**Lichtenberg core PD.028**	**Biostratigraphy** **(Menke and Tynni, 1984; Behre and Lade, 1986)**
Pollen/Vegetation	**LPAZ**	**Layer and Pollen/vegetation**	**Depth [m] Pollen/vegetation**	
NAP, strong increase of Poacaea	**Li 9**		**3.75m - 3.55m, 2.5m - 2.3m** NAP, very strong rise of Poaceae **Steppe-Tundra vegetation**	**Schalkholz (WP I)**
Pinus-Picea **(*Larix*), Sphagnum**	**Li 8**		**4.65m – 5,3m, 5.55m - 5.3m** *Pinus-Betula-Picea (Larix)* **boreal coniferous forest**	**Odderade** **(WE IV b)**
Betula-Salix-Pinus, **Cyperaceae**	**Li 7**			**(WE IV a)**
NAP dominance, *Sphagnum*, Ericaceae	**Li 6**	transition **11 to 10** NAP dominance, *Betula*, Poaceae, open **Tundra-like vegetation**		**Rederstall (WE III)**
Pinus-Betula-Picea (Larix, Alnus)	**Li 5** **Li 4**	**11a, 11b, 11b$_2$** *Pinus-Betula, very few Picea (Alnus, Larix)* **Boreal coniferous forest (opening up)**		**Brörup** **(WE II b)**
Betula-Pinus **(strong decrease of NAP)**				**(WE II a)**
NAP dominance (Poaceae, *Artemisia*)	**Li 3**			**Herning (WE I)**
Pinus-Picea-Alnus	**Li 2**			**Eemian** **(E VI (/VII))**
Carpinus-Alnus- **Quercetum mixtum-*Corylus*** **(*Picea*)**	**Li 1**			**(E V)**

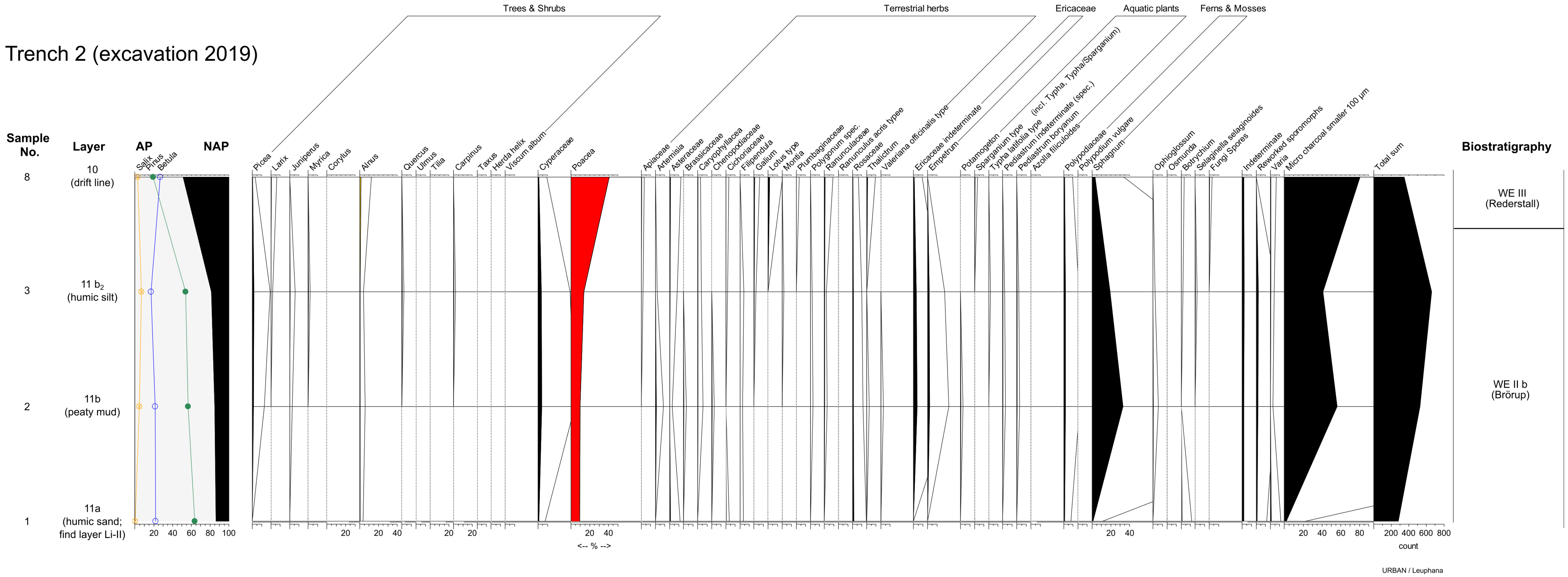

Supplementary Figure S 60. Pollen diagram of bulk samples 1, 2, 3 and 8 (Trench 2, excavation Lichtenberg 2019). Layers from bottom to top: 11a, 11b, 11b2, 10. Biostratigraphic assignment on the right

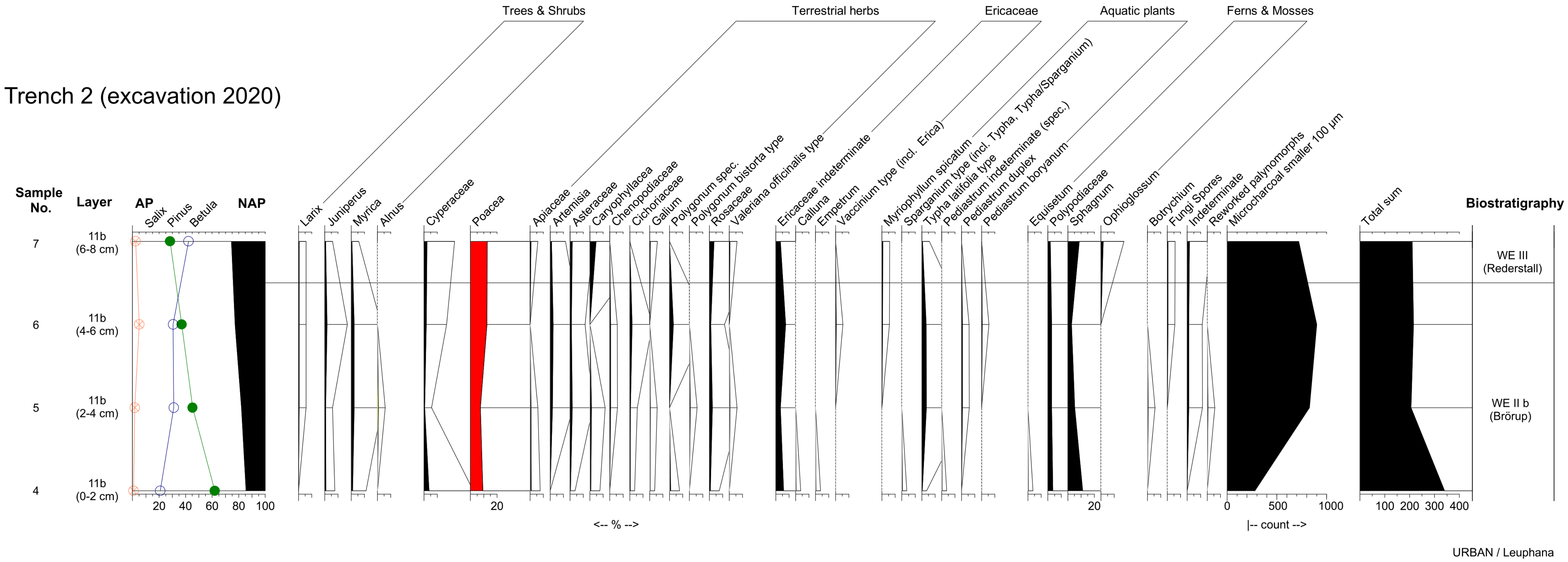

Supplementary Figure S 61. Pollen diagram of bulk samples 4 to 7 (0-8 cm) from layer 11b (Trench 2, excavation Lichtenberg 2020), documenting the gradual transition from Brörup Interstadial to Rederstall Stadial.

Core PD.028

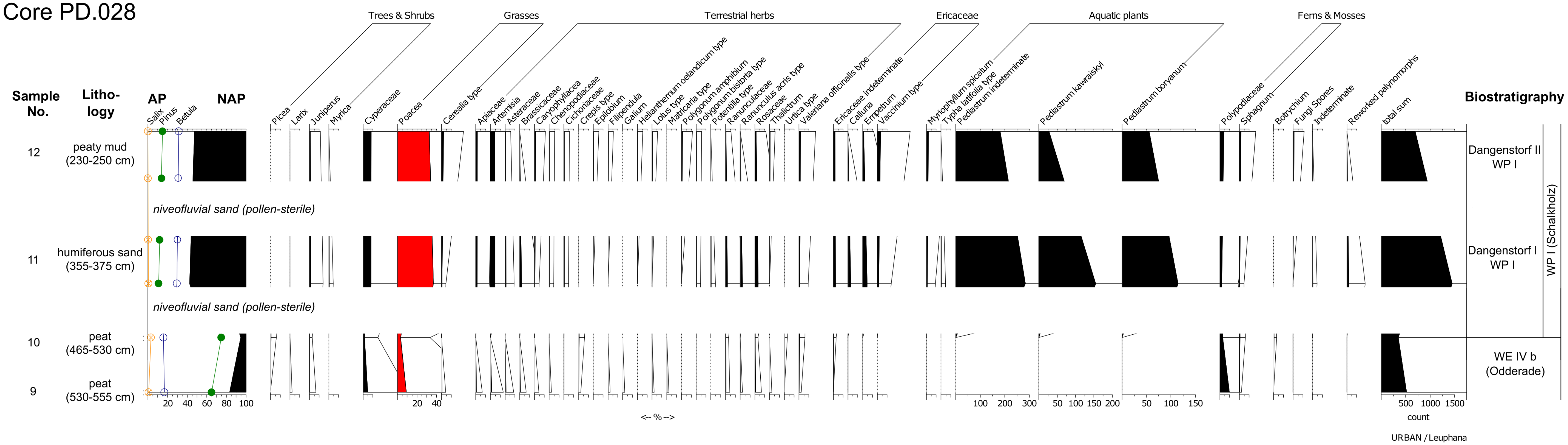

Supplementary Figure S 62. Pollen diagram of bulk samples 9 to 12 from core PD.028.

Supplementary Table S 15. Phytolith sample information by layer.

Sample	Phytoliths in 1 g of sediment	Phytoliths in 1 g of sediment count	Layer	Area designation	Collector	Year collected
MH1	7,636	213	layer 7	Trench 1 East	MH	2019
MH2	62,740	306	layer 11a	Trench 2	MH	2019
MH3	18,379	271	layer 7	Trench 1 South	MH	2019
MH4	6,980	156	layer 8	Trench	MH	2019
MH5	5,556	150	layer 9	Trench	MH	2019

Supplementary Table S 16. The number of multi-cell phytoliths and other biogenic silica particles per gram of dry sediment and summary information. For the summary, grey histogram bars show the row-wise (sample-wise) proportion of values related to the highest value in a row (invariably sample MH2).

Sample:	MH1	MH2	MH3	MH4	MH5
MULTI-CELL	n/g	n/g	n/g	n/g	n/g
Leaf/Stem:		205	272	97	
Polyhedral honeycomb:				45	0
Indeterminate:			68	0	38
Monoaxon spicule			68		31
Pennate diatom				45	
Grass stem	2,310	13,942	2,723	1,126	457
Grass floral	0	615	0	0	0
Grass	5,775	34,856	8,849	3,107	2,093
Monocots	5,775	35,061	8,849	3,107	2,055
Eudicots	1,091	3,896	1,429	270	266
Panicoid	0	820	0	0	0
Festucoid	1,348	8,201	1,702	676	457
Total long cell	36	72	40	26	12
Total short cell	41	77	71	30	35
Long cell/short cell index	36:41	72:77	40:71	13:15	12:35
Multi-cell/Single cell	0.00	0.00	0.00	0.00	0.00
Total Identifiable	7,636	44,902	11,640	4,008	2,770
Total no. phytoliths	13,604	62,740	18,379	6,980	5,670
Total fields on slide	9,062	2,261	7,776	15,052	17,221

Supplementary Table S 17. The number of single-cell phytoliths per gram of dry sediment.

Sample:	MH1	MH2	MH3	MH4	MH5
Parallelepiped elongate thin psilate:	1,733	9,432	2,451	901	419
Parallelepiped elongage thin sinuate:	193	2,460	136	45	0
Parallelepiped thin echinate:	0	410	0	0	0
Parallelepiped elongate thin indermin:	0	205	0	45	
Parallelepiped elongate thin wavy:		410	0	90	
Cylindroid psilate:	385	1,640	136	90	38
Parallelepiped elongate thin dendriform	0	205	0		
Trichome:	578	2,665	749	495	266
Unspecific hair:	0	205	0		
Prickle:	0	0	68		
Bulliform:	321	615	408	45	38
Bulliform fan:	0	205	0		
Oval:	0	410	68	45	
Short cell rondel:	898	5,536	817	360	152
Short cell square trapezoid:	193	410	340	45	114
Short cell smooth trapezoid:	193	0	0	0	38
Short cell sinuate trapezoid:		0	0	0	38
Short cell oblong trapezoid:	64	2,255	545	270	152
Short cell reniform:		205	68		
Short cell truncated tip bilobate:		820			
Indeterm shortcell:	1,219	6,561	3,063	676	837
Elongate trapezoid:		410	0		
Rugulose Spheroid:	64	0	0		
Spheroid smooth:		205	68		
Stellate-like spheroid:		0	0	45	
Platey:	257	1,640	68	90	0
Elongate:	128	2,050	545	405	228
Trapezoid:		205	0		
Oblong thick:		0	68		
Parallelepiped thin:		615	68		38
Block:		0	0		
Thick block:	385	1,435	749	45	38
Thin block:	128	410	204	45	266
Eudicot stoma:	0	205			
Parallelepiped thick elongate:	0	0		45	
Parallelepiped sinuathick elongate:			68		
Parallelepiped thick elongate scalloped:	64	0	136		
Sulcate:	64	0			
Sclereids:	0	0	204		
Polyhedron:	128	0	68	90	
Jigsaw type:	64	205			
Parallelepiped curved:	0	205			
Epidermal anticlinal pinus possible:	64				
Irregular:	513	2,665	476	90	76
Indeterminate:	5,968	17,838	6,807	3,017	2,930
Highly eroded count:	1,218	4,101	1,361		304